

# INDUCING AND PROBING CHARGE MIGRATION IN MOLECULAR SYSTEMS

arXiv:2502.16979v1 [physics.optics] 24 Feb 2025

*Sucharita Giri*



# INDUCING AND PROBING CHARGE MIGRATION IN MOLECULAR SYSTEMS

*Submitted in partial fulfillment of the requirements  
of the degree of*

**Doctor of Philosophy**

*by*

**Sucharita Giri**

Supervisor:

**Prof. Gopal Dixit**



**DEPARTMENT OF PHYSICS  
INDIAN INSTITUTE OF TECHNOLOGY BOMBAY**

**2023**

© 2023 Sucharita Giri All rights reserved.



Dedicated to my parents, and my sisters.



# Declaration

I declare that this written submission represents my ideas in my own words and where others' ideas or words have been included, I have adequately cited and referenced the original sources. I also declare that I have adhered to all principles of academic honesty and integrity and have not misrepresented or fabricated or falsified any idea/data/fact/source in my submission. I understand that any violation of the above will be cause for disciplinary action by the Institute and can also evoke penal action from the sources which have thus not been properly cited or from whom proper permission has not been taken when needed.

Sucharita Giri  
(Roll No. 174123002)





# Acknowledgements

I would like to acknowledge everyone who has helped me grow personally and academically throughout this Ph.D. journey. I can't possibly include everyone, but I'll try to mention the ones who have made a significant impact.

First and foremost, I would like to thank my supervisor, Prof. Gopal Dixit, for his guidance, patience, and support throughout the course of my research. His valuable advice and feedback helped me to complete this thesis.

I would like to express my sincerest gratitude to Prof. Jean Christophe Tremblay, for his guidance throughout the entire process and for inviting me to Freie University Berlin as a guest researcher with financial support. I could not have completed my Ph.D. without his help. Thank you for being such a great collaborator.

I would like to express my gratitude to the collaborators from IIT KGP, Prof. Partha Pratim Jana and Dr. Nilanjan Roy. I have really enjoyed learning the new concepts during the pandemic.

I would also like to thank the RPC members, Prof. Sumiran Pujari and Prof. Amber Jain, for their guidance and advice, and for taking the time to read my reports and be present in my annual progress seminar (APS) presentations.

I am thankful to all my charming and caring friends. A special thanks to Adhip, Monish, Manisha, Supriti and Suman for all the good moments shared throughout my campus journey. Thank you Sovan for being there through all the ups and downs. You are always a constant support in my life. I want to thank Avishek, who was a help to me throughout the writing of my thesis. Thank you Aneesha for the friendly discussions and all the encouragement.

Most importantly, I would like to thank my family for their unwavering love and support. They have understood throughout this entire process. Maa and Baba, thank you for being my heroes all my life. My little sisters, thank you for all your support and sacrifices. I could not have asked for better people to have in my corner.

---

I want to thank Irfana, Mrudul, Adhip, Navdeep, and Amar for being such friendly and supportive labmates. Furthermore, I would like to record my thanks to all the staff members of IITB for making life inside IITB much easier. Finally, I would like to thank my institution for providing the resources and infrastructure.

Sucharita Giri  
Department of Physics  
IITB

# Abstract

Technological advancements in generation of ultrafast and intense laser pulses have enabled the real-time observation and control of charge migration in molecules on their natural timescale, which ranges from few femtoseconds to several hundreds of attoseconds. Present thesis discusses the effect of symmetry on the adiabatic attosecond charge migration in different molecular systems. The spatial representation of the charge migration is documented by time-dependent electronic charge and flux densities. Furthermore, the induced charge migration is imaged via time resolved x-ray diffraction (TRXD) with atomic-scale spatiotemporal resolution in few cases.

We have studied how the charge migration will be modified if one reduces the symmetry of the molecule by transiting from six-membered benzene to heterocyclic five-membered ring molecules. For this purpose, the effects of symmetry reduction and electronegativity are investigated by a comparative study of the charge migration in pyrrole, furan, and oxazole with the help of the time-dependent electronic charge and flux densities are used. In the next case, we have studied the role of symmetry reduction on the charge migration in copper corrole – a non-planer molecule with saddled geometry. Correlation of the flux densities and TRXD signals indicates that the signature of the structural saddling during charge migration is imprinted in TRXD signals. After studying charge migration in molecules with certain symmetries, we have explored charge migration in molecules without any symmetry – chiral molecules. Control over charge migration in R- and S-epoxypropane is achieved by choosing the different orientations of the linearly polarized pulse. For oriented and floppy molecules, we find that the charge migration is different for enantiomers when the polarization of the pulse lies in the mirror plane defining the enantiomer pair. It is found that the total TRXD signals are significantly different for both enantiomers. Furthermore, a asymmetry parameter is introduced to discern the concentration of an enantiomer in the racemic mixture.

**Key words:** Charge migration, Molecular symmetry, Electronic flux density, TRXD, Chirality



# Contents

Title Page . . . . .	i
Declaration . . . . .	v
Acknowledgements . . . . .	vii
List of Symbols and Abbreviations . . . . .	ix
Abstract . . . . .	ix
List of Figures . . . . .	xiii
List of Symbols and Abbreviations . . . . .	xix
<b>Chapter 1 Introduction . . . . .</b>	<b>1</b>
1.1 Attosecond Physics . . . . .	2
1.1.1 Time-Resolved X-ray Diffraction . . . . .	4
1.2 Charge Migration . . . . .	5
1.3 Aim of This Thesis . . . . .	7
1.4 Outline . . . . .	11
<b>Chapter 2 Theoretical Framework for Laser-Induced Charge Mi- gration . . . . .</b>	<b>13</b>
2.1 Electronic Structure Theory . . . . .	14
2.1.1 Wave Function Based Methods . . . . .	14
2.1.2 Density Based Methods . . . . .	16
2.2 Laser-Induced Charge Migration . . . . .	20
2.2.1 Electronic Continuity Equation . . . . .	21
2.3 Time-Resolved X-ray Diffraction . . . . .	23
2.4 Technical Details . . . . .	26
<b>Chapter 3 Charge Migration in Heterocyclic Five-Membered Plan- ner Molecules . . . . .</b>	<b>29</b>
3.1 Results and Discussion . . . . .	31

3.2	Summary . . . . .	39
<b>Chapter 4</b>	<b>Role of Structural Saddling on Charge Migration . . .</b>	<b>41</b>
4.1	Results and Discussion . . . . .	43
4.2	Summary . . . . .	52
<b>Chapter 5</b>	<b>Imaging Charge Migration in Chiral Molecules . . . . .</b>	<b>53</b>
5.1	Results and Discussion . . . . .	57
5.1.1	Effect of imperfect orientation on electronic flux densities . . . . .	65
5.1.2	Imaging charge migration by TRXD . . . . .	67
5.2	Summary . . . . .	75
<b>Chapter 6</b>	<b>Conclusions and Future Directions . . . . .</b>	<b>77</b>
6.1	Conclusions . . . . .	77
6.2	Future Directions . . . . .	80
	<b>Bibliography . . . . .</b>	<b>83</b>
	<b>List of Publications . . . . .</b>	<b>105</b>
	<b>List of Publications . . . . .</b>	<b>105</b>

# List of Figures

- 1.1 An illustration of the overview of the impact of molecular symmetry during laser-induced charge migration in different molecules. (i) Planar molecules pyrrole and furan with  $C_{2v}$  and oxazole with  $C_s$  point group symmetries, (ii) structural saddling in copper corrole with  $C_2$  symmetry and (iii) R- and S-epoxypropane with  $C_1$  symmetry. Results of benzene and magnesium porphyrin are adapted from (Hermann et al., 2020) and (Nam et al., 2020), respectively. . . . . 10
- 3.1 Depiction of the electronic structure in the five-membered ring molecules. Pyrrole, furan, and oxazole are represented from left to right. (a) Ground state electron density (isocontours equally separated by 0.001 a.u.). (b) Natural transition orbitals. Orange and blue surfaces represent the particle and hole densities, respectively. (c) Difference electron densities between target excited and ground electronic states,  $\rho_m(\mathbf{r}) - \rho_0(\mathbf{r})$ . Red (blue) colour represents regions of density depletion (increase). The isosurface values are  $\pm 0.005$ ,  $\pm 0.02$ , and  $\pm 0.03$  for pyrrole, furan, and oxazole, respectively for both NTOs and transition densities. . . . . 32
- 3.2 Laser-induced population dynamics in heterocyclic five-membered ring molecules triggered by 20 fs sine-squared linearly polarized pulse along  $y$  axis. The label “resp” indicates the residual population of all other electronic states, which acts as a non-linear response during the excitation. The three molecules are shown in ball-and-stick representation, which are projected in the  $yz$  plane throughout in this work. White, grey, blue and red colours represent hydrogen, carbon, nitrogen and oxygen, respectively. (a) Pyrrole: carrier frequency resonant with the energy of the 5<sup>th</sup> electronic state (6.26 eV); peak intensity of  $3.7 \times 10^{13}$  W/cm<sup>2</sup>. (b) Furan: carrier frequency resonant with the energy of the 2<sup>nd</sup> electronic state (6.26 eV); peak intensity of  $2.8 \times 10^{13}$  W/cm<sup>2</sup>. (c) Oxazole: carrier frequency resonant with the energy of the 1<sup>st</sup> electronic state (6.37 eV); peak intensity of  $7 \times 10^{13}$  W/cm<sup>2</sup>. . . . . 33

3.3	Time-dependent difference electron and associated flux densities during charge migration in pyrrole at $1T$ , $2T$ and $6T$ . Here, $T = \tau/8$ with $\tau = 660$ attoseconds as the characteristic timescale of the charge migration in pyrrole. Ground-state electron density is subtracted in the time-dependent difference electron density at each subsequent time step. The colour of the streamline arrows varies from white to black according to their increasing intensity. The red and blue contours present the depletion and the enhancement of the difference electronic density with respect to the ground state density. For better visualisation, the projection of pyrrole in the $yz$ plane is superposed in ball-stick representation. . . . .	35
3.4	Same as Fig. 3.3 for furan with $\tau = 660$ attoseconds as the characteristic timescale. . . . .	36
3.5	Same as Fig. 3.3 for oxazole with $\tau = 650$ attoseconds as the characteristic timescale. . . . .	38
4.1	Ball-stick representation of unsubstituted copper corrole in different orientations, with the molecule in the $yz$ plane. Magenta, tan, black, and white spheres represent copper, nitrogen, carbon, and hydrogen atoms, respectively. . . . .	42
4.2	Population dynamics of selected electronic states of copper corrole. $ 0\rangle$ represents the ground electronic state, and $ 9\rangle$ represents the target electronic state with energy $E_9 = 3.45$ eV. The orange line labeled “resp” represents the electronic response in the presence of the field, leading to the residual population of the rest of the electronic states after the excitation. A cosine-squared linearly polarized pulse of 360 nm wavelength with peak intensities of $3.5 \times 10^{13}$ W/cm <sup>2</sup> is used to induce the population dynamics. The pulse is 10 fs short and polarized along the $y$ axis. Time zero defines the onset of field-free electron dynamics. . . . .	44
4.3	Time-resolved difference diffraction signals for copper corrole in (a) $Q_y - Q_z$ and (b) $Q_x - Q_y$ planes at different pump-probe delay times during field-free charge migration. Here, $T = \tau/40$ is chosen with $\tau = 1.2$ fs as the characteristic timescale of the charge migration. The intensity of the diffraction patterns is presented in units of $dP_e/d\Omega$ . The time-independent diffraction signal at zero delay time is subtracted at all subsequent delay times. . . . .	45
4.4	(a) Real and (b) imaginary part of $\mathcal{L}_{90}(\mathbf{Q})$ in the $Q_x - Q_y$ , $Q_y - Q_z$ , and $Q_z - Q_x$ planes, respectively (from left to right). . . . .	47



4.5	Time evolution of the electron density of the wavepacket during field-free charge migration in copper corrole. The electron density at zero time delay is subtracted at all subsequent delay times and the difference density is represented in the (a) $yz$ and (b) $xy$ planes. As in Fig. 4.3, $T = \tau/40$ is chosen with $\tau = 1.2$ fs as the characteristic timescale of the electron dynamics. . . . .	48
4.6	Time-dependent electronic flux densities for copper corrole in the (a) $yz$ and, (b) $xy$ planes at different pump-probe delay times during field-free charge migration. The laser excitation parameters are the same as in Fig. 4.2. The period $T = \tau/40$ is chosen as the oscillation period $\tau = 1.2$ fs of the electron dynamics. The black, violet, maroon, and gray dots represent carbon, copper, nitrogen, and hydrogen atoms, respectively. . . . .	49
4.7	The static diffraction signals corresponding to the ground state for (a) copper corrole and (b) copper porphyrin in the $Q_y - Q_z$ , $Q_y - Q_x$ and $Q_z - Q_x$ planes (from left to right). The signals are normalized with respect to their maximum values. . . . .	51
5.1	R- and S-enantiomers of epoxypropane in the molecular fixed frame. Gray, black and red spheres represent hydrogen, carbon and oxygen atoms, respectively. The chiral carbon is labelled by C. The $xy$ plane is the mirror plane and the normal axis lies along the $z$ direction. .	54
5.2	Population dynamics of selected electronic states for (a) R- and (b) S-epoxypropane. A sine-squared (carrier frequency: 7.67 eV; duration: 10 fs; peak intensity: $10.1 \times 10^{14}$ W/cm <sup>2</sup> ) linearly polarized pulse along the $x$ axis is used to excited the first optically accessible band in both enantiomers. $ 0\rangle$ represents the ground electronic state. Only the excited states at energies $E_2 = 7.51$ eV, $E_3 = 7.56$ eV, and $E_4 = 7.73$ eV are significantly populated throughout the dynamics. The time origin, $T = 0$ , defines the onset of field-free charge migration.	57
5.3	(a) Electronic charge distribution difference, $\rho(\mathbf{r}, t) - \rho(\mathbf{r}, 0)$ , and (b) corresponding flux densities (blue arrows) for both R- and S-enantiomers during field-free charge migration, at different times after the onset of the field-free charge migration. The field parameters are defined in the caption of Fig. 5.2. Orange and blue colours represent isosurface values of -0.0015 and +0.0015, respectively. . .	58

5.4	Population dynamics of selected electronic states for (a) R- and (b) S-epoxypropane. A sine-squared (carrier frequency: 7.75 eV; duration: 10 fs; peak intensity: $9.1 \times 10^{14}$ W/cm <sup>2</sup> ) linearly polarized pulse in the $yz$ plane is used to excite the first optically accessible band in both enantiomers. Only the excited states at energies $E_3 = 7.56$ eV, $E_4 = 7.73$ eV, and $E_5 = 7.84$ eV are significantly populated throughout the dynamics. . . . .	60
5.5	(a) Electronic charge distribution difference and (b) corresponding flux densities (blue arrows) for both R- and S-enantiomers during field-free charge migration, at different times after the laser pulse linearly polarized in the $yz$ plane. The field parameters are defined in the caption of Fig. 5.4. Orange and blue colours represent iso-surface values of -0.0015 and +0.0015, respectively. . . . .	61
5.6	Time evolution of (a) $x$ -, (b) $y$ - and (c) $z$ -components of the total dipole moment during and after excitation by a 10 fs sine-squared linearly polarized pulse along the $x$ axis. The field parameters are the same as in Fig. 5.2. . . . .	62
5.7	Time evolution of the cartesian components of the dipole moment along (a) $x$ -, (b) $y$ - and (c) $z$ -directions. The amplitude and phase along all the axes are different for both the enantiomers. The field parameters are the same as in Fig. 5.4. . . . .	63
5.8	(a) Electronic charge distribution difference and (b) corresponding flux densities (blue arrows) for both R- and S-enantiomers at different rotation angles with respect to $z$ axis, during field-free charge migration, at $T = 6$ fs for linearly polarized laser pulse in $yz$ plane. Isocontours at +0.0020 (blue) and -0.0020 (orange) for the enantiomers. . . . .	66
5.9	Time-dependent electronic flux densities for (a) R- and, (b) S-enantiomers of epoxypropane in the $xz$ plane at 2 fs, 6 fs, 10 fs, and 14 fs after the pump pulse. Violet, maroon and gray colors are representing carbon, oxygen and hydrogen atoms, respectively. Here, $z$ axis is defined as the chiral axis in the molecular frame of reference. . . . .	68
5.10	Time-independent diffraction patterns for (a) R- and (b) S- enantiomers of epoxypropane on left and right panels, respectively. The diffraction patterns are presented in $Q_z - Q_x$ plane in units of $dP_e/d\Omega$ . An ultrashort x-ray pulse of 8 keV mean energy is aimed to obtain 1.55 Å spatial resolution in these simulations. All diffracted photons up to 60° are collected in the detector. . . . .	69

5.11	Time-resolved diffraction patterns for (a) R- and, (b) S-enantiomers of epoxypropane in $Q_z - Q_x$ plane at 2 fs, 6 fs, 10 fs, and 14 fs. Intensity of the diffraction patterns is presented in units of $dP_e/d\Omega$ . Here, time-dependent diffraction signal at $T = 0$ fs is subtracted to the subsequent delay time. An ultrashort x-ray pulse of 8 keV mean energy is aimed to obtain 1.55 Å spatial resolution in these simulations. All diffracted photons up to $60^\circ$ are collected in the detector. . . . .	70
5.12	Time-derivative of electron density in momentum space, $ \partial_t \rho(\mathbf{Q}) $ , for (a) R- and, b) S-enantiomers of epoxypropane in $Q_z - Q_x$ plane at 2 fs, 6 fs, 10 fs, and 14 fs. . . . .	73
5.13	Asymmetry parameter $Y$ along (a) $Q_x$ and, (b) $Q_z$ axes as a function of the delay time. The 1D TRXD signal is obtained from Eq. (2.3.8) and integrated along the other axes. . . . .	74



# List of Symbols and Abbreviations

## Symbols

$\mathcal{H}_0$	Time-independent molecular Hamiltonian
$\mathcal{H}(t)$	Time-dependent Hamiltonian
$\mathcal{H}_{\text{int}}(t)$	Time-dependent interaction Hamiltonian
$ \Phi_k(\mathbf{r})\rangle$	Time-independent multi-electronic wave function
$ \Psi(\mathbf{r}, t)\rangle$	Laser-induced electronic wavepacket
$\rho(\mathbf{r}, t)$	Time-dependent electronic charge density
$\mathbf{j}(\mathbf{r}, t)$	Time-dependent electronic flux density
$dP/d\Omega$	Differential scattering probability
$dP_e/d\Omega$	Differential scattering probability of a free electron
$T$	Pump-probe time delay
$\tau$	Characteristic timescale of the charge migration

## Abbreviations

TDSE	Time-dependent Schrödinger equation
HF	Hartree-Fock
CIS	Configuration interaction singles
DFT	Density functional theory
TDDFT	Time-dependent density functional theory
TDDFT/CI	Hybrid time-dependent density functional theory-configuration interaction
TRXD	Time-resolved x-ray diffraction
EFD	Electronic flux density
DSP	Differential scattering probability
IRREP	Irreducible representation
NTOs	Natural transition orbitals



# Chapter 1

## Introduction

The motion of atoms within molecules associated with light-induced exciton dynamics, conformational changes, bond formation and breakage during chemical reactions occurs on the femtosecond ( $1 \text{ fs} = 10^{-15} \text{ s}$ ) timescale. Thus, understanding the dynamics of atoms (nuclei) during complex chemical and biological processes has started an era of femtochemistry (Zewail, 2000). Electrons are the glue that keeps the atoms within molecules together and their dynamics play a crucial role in the function and transformation of molecules. The distinctive timescale of electronic motion, responsible for electron-hole dynamics and charge migration processes in molecules can be even faster, ranges from a few femtoseconds to several hundreds of attoseconds ( $1 \text{ as} = 10^{-18} \text{ s}$ ).

When a molecule is exposed to an ultrashort laser pulse, electrons are the first to respond to the action of the incident laser. Depending on the energy and pulse duration of a coherent laser pulse, several interesting processes can take place in a molecule during laser-molecule interaction. A superposition of several electronic states in the form of an electronic wavepacket can be created if the energy of the laser is smaller than the ionization potential of the valence electron in a molecule and the energy bandwidth is of the order of few electron-volts. The characteristic timescale of the created wavepacket can be estimated from  $\tau = \hbar/\Delta E$ , where  $\Delta E$  is the energy difference between electronic states involved in the wavepacket. In general, the electronic motion associated with the wavepacket occurs on attosecond

timescale and not impacted by nuclear motion. Thus, a coherent electronic motion can be described as a coherent superposition of multiple electronic states with fixed nuclei configuration. Observations of the attosecond electronic motion was not possible until the realization of the coherent attosecond laser pulses. Before we discuss the main theme of this thesis, let us briefly recap the key mechanisms and early findings in attosecond physics, an essential ingredient for charge migration, in the next section.

## 1.1 Attosecond Physics

Recent developments in coherent light sources made the generation of attosecond pulses possible and gave a birth to a new era of ultrafast physics – attosecond physics. Attosecond pulses can be generated from a high-harmonic generation, which is a strong-field driven nonlinear process. In last two decades, attosecond pulses have been used to study a number of interesting ultrafast processes in atoms, molecules and solids. Pump-probe technique is the most common approach in attosecond experiments in which an ultrashort “pump” pulse induces an attosecond electronic motion, which is subsequently captured by the second “probe” pulse. The induced motion can be interrogated at different instances during the dynamics by varying the delay between the pump and probe pulses. Time-resolved photoionization (emission) spectroscopy, attosecond transient-absorption spectroscopy, two-colour high-harmonic spectroscopy are few commonly used spectroscopy methods on attosecond timescale. Not only generating attosecond pulses but its characterization is essential before performing any attosecond experiment. Attosecond streaking and RABBITT (reconstruction of attosecond beating by interference of two-photon transitions) are two commonly used attosecond pulse characterization techniques. Moreover, these two methods are also used to interrogate attosecond processes in atoms, molecules and solids as both the methods are based on time-resolved photoionization concept. Attosecond streaking is closely related to RABBITT in which isolated attosecond pulse is used instead of attosecond pulse train for photoionization (Krausz and Ivanov, 2009).

Soon after the realization of attosecond pulses in 2001 (Hentschel et al., 2001;



Paul et al., 2001), time-resolved spectroscopy of Auger relaxation in krypton is demonstrated (Drescher et al., 2002). Over the years, several fundamental attosecond processes in different atomic systems have been experimentally observed such as real-time observation of valence electron in krypton via attosecond transient absorption spectroscopy (Goulielmakis et al., 2010), characterization of electron wavepacket in helium (Mauritsson et al., 2010), measurement of photoemission time-delay in neon (Schultze et al., 2010), real-time electron dynamics in the vicinity of Fano resonance in helium (Gruson et al., 2016), tunnelling dynamics of electron in neon (Uiberacker et al., 2007), to name but a few.

Not only ultrafast electronic motion in atoms but also in molecules and solids has been investigated by attosecond spectroscopy. Few selected examples include attosecond time-delay in photoelectrons emitted from localized core and delocalized conduction-band states in crystalline tungsten (Cavalieri et al., 2007), light-driven insulator-conductor phase transition in a dielectric (Schiffrin et al., 2013), electron dynamics between valence and conduction energy bands in silicon using attosecond transient absorption spectroscopy (Schultze et al., 2014), nonlinear polarization and light-matter energy transfer in solids (Sommer et al., 2016). Moreover, attosecond pulse driven dissociative dynamics in diatomic molecules have been explored in  $\text{H}_2$  (Sansone et al., 2010; Kelkensberg et al., 2011) and  $\text{O}_2$  (Siu et al., 2011). In later part of this chapter, we will discuss attosecond spectroscopy of “more” complicated molecules.

Attosecond pulses, produced by high-harmonic generation process, have two serious limitations: Relatively low intensity (fluence) and limited range of available photon energies. In the last decade, alternate source of coherent ultrashort pulses, based on particle acceleration technology, came into existence. Thanks to technological advances that have made possible to generate intense ultrashort pulses from recently operational novel x-ray source: X-ray free-electron laser (XFEL), which offers to circumvent these limitations upto certain extent (Ishikawa et al., 2012; Pellegrini et al., 2016; Emma et al., 2010). Laser pulses with few femtoseconds pulse duration in energy regime ranges from extreme ultraviolet to hard x-ray are routinely employed to perform various interesting experiments at different

XFEL sources such as LCLS, SACLA, and European XFEL. Moreover, feasibility to generate attosecond x-ray pulses was demonstrated experimentally in recent years (Hartmann et al., 2018; Duris et al., 2020).

### 1.1.1 Time-Resolved X-ray Diffraction

Since the discovery of x-rays, diffraction of x-rays from matter has been used to unveil the arrangement of atoms inside a matter with atomic-scale spatial resolution. Also, insights about the excited electronic states of atoms and molecules can be obtained via scattering of x-rays from a matter. Thus, x-ray diffraction has become a well-established method in several areas of science to access atomic-scale structural information of complex materials, ranging from molecules to biological complexes. Moreover, utilizing the Fourier relationship between the electron density of an object and the diffraction intensity (i.e., elastic x-ray scattering), coherent diffractive imaging became a powerful lensless technique to obtain three-dimensional structural information of nonperiodic and periodic samples.

The availability of ultrashort x-ray pulses from XFELs have enabled to extend static x-ray diffraction into time domain with exceptional temporal resolution (Lindroth et al., 2019). Time-resolved x-ray diffraction (TRXD) within pump-probe configuration has become a method of choice to obtain snapshots of a temporarily-evolving electronic charge distribution in matter with spatiotemporal resolution on atomic and electronic scales (Peplow, 2017). The concept of “molecular movies”, which track the motion of atoms on femtosecond timescale, can be extended with the availability of the ultrashort, tunable, and high-energy x-ray pulses from XFEL, which promises to provide “electronic movies” that take place on few femtosecond to attosecond timescale (Dixit et al., 2012; Vrakking and Elsaesser, 2012). A series of diffraction signals, obtained at different instants of the motion at various pump-probe time delay, may be stitched together to make a movie of the electronic motion with unprecedented spatiotemporal resolution. In this context, a straightforward extension of x-ray diffraction from the static to the time domain would seem to suggest that the diffraction signal encodes information related to the instantaneous electron density on attosecond timescale. However, it has been established that

the TRXD signal is not related to the instantaneous electron density and different formalisms of TRXD have been developed over the years (Henriksen and Møller, 2008; Dixit et al., 2012; Dixit and Santra, 2013; Bennett et al., 2018; Simmermacher et al., 2019a; Dixit et al., 2013, 2014; Santra et al., 2014; Dixit and Santra, 2017; Kowalewski et al., 2017).

To demonstrate the capabilities of x-rays from XFELs, aligned 2,5-diiodobenzonitrile is tested as a first molecule from which static x-ray diffraction has been performed at LCLS (Küpper et al., 2014). Frequency-resolved TRXD was employed to disentangle dissociative and bound electronic states during vibrational motion in iodine (Ware et al., 2019); and vibrational motion in iodine was imaged by TRXD on femtosecond timescale (Glowia et al., 2016). Anisotropic TRXD measurements have been performed to determine transition dipole moment and assign excited electronics states in molecules (Yong et al., 2018). Light-induced cis-trans photochemical structural changes in photoactive yellow protein (Pande et al., 2016), and structural changes during ring opening electrocyclic chemical reaction in cyclohexadiene (Minitti et al., 2015, 2014) were imaged by TRXD. Furthermore, the changes in the electron density during ring opening in 1,3-cyclohexadiene were discussed experimentally and theoretically using TRXD (Yong et al., 2020). In this thesis, we will employ TRXD to image the dynamics of an electronic wavepacket in selected molecules, which we will discuss in later chapter.

## 1.2 Charge Migration

As discussed earlier, an interaction of the coherent laser pulse with a molecule leads the creation of a coherent superposition of several electronic states. If the energy of the coherent laser pulse is high enough to remove an electron from an inner-shell state by photoionization, a hole can be created and the ionized molecule is driven to a non-equilibrium state. Owing to the large density of ionic states, the formation of a hole can be seen as a coherent superposition of several ionic electronic states. The hole is spatially localized in the beginning. As the time progresses, the coherent superposition evolves in time, which leads the migration of the hole around the atoms within the molecular scaffold (Kuleff and Cederbaum, 2014). Cederbaum

and Zobeley were first to introduce the notion of charge migration on attosecond timescale associated with the hole dynamics (Cederbaum and Zobeley, 1999). It is assumed that the nuclei are frozen during the charge migration, which is completely different from nuclei-driven electron transfer in molecules (May and Kühn, 2008). The first theoretical prediction of charge migration in difluoropropadienone has triggered a number of theoretical study in variety of molecules with the emphasis of multielectron effects such as 2-propyn-1-ol, N-methyl acetamide, oligopeptide Gly-Gly-NH-CH<sub>3</sub>, 4-methylphenol, 2-Phenylethyl-N,N-dimethylamine (PENNA), tetrapeptides, glycine to name but a few (Breidbach and Cederbaum, 2003, 2005; Hennig et al., 2005; Remacle and Levine, 2006; Kuleff et al., 2005; Kuleff and Cederbaum, 2014). Two experimental proposals with appropriate theoretical description on charge migration in polypeptide molecules have been discussed (Lépine et al., 2014). Predictions made by Cederbaum and others have not been verified till 2014 when attosecond spectroscopy reached to an advance level.

As mentioned earlier, attosecond spectroscopy during the initial phase was limited to simple diatomic molecules like H<sub>2</sub> and O<sub>2</sub>. However, as time progressed, attosecond spectroscopy steadily advanced toward the investigation of more complicated molecules with the ability to initiate and interrogate coherent charge migration. In 2014, Calegari and co-workers have performed first experiment to probe charge migration in amino acid phenylalanine using pump-probe method in which an attosecond pump pulse was used to create a hole wavepacket and a near infrared/visible probe pulse was applied to probe the charge migration (Calegari et al., 2014). Subsequently, two-colour high-harmonic spectroscopy was used to observe the charge migration in iodoacetylene spatiotemporally (Kraus et al., 2015). In this experiment, an intense infrared pulse was used for a strong-field ionization of iodoacetylene and a resultant hole wavepacket was probed by high-harmonic spectroscopy. It was observed that the orientation of iodoacetylene with respect to the ionizing pulse has a significant impact on the charge migration (Kraus et al., 2015). By combined experimental and theoretical investigation of the charge migration in tryptophan, it has been established that the nuclear dynamics do not significantly alter the coherence induced by the attosecond pulse during the early

stages of the wavepacket dynamics (Lara-Astiaso et al., 2018). Later, time-resolved mapping of the correlation-driven charge migration in the nucleic-acid base adenine was performed by double ionization pump-probe method (Mansson et al., 2021). Recently, high-harmonic spectroscopy was applied to probe charge migration in  $\text{N}_2$  and  $\text{CO}_2$  with 50 attoseconds temporal resolution (He et al., 2022). The influences of the length, bond order, and halogenation on the charge migration in halogenated hydrocarbon chains have been explored theoretically (Folorunso et al., 2021). Detailed reviews on charge migration in molecules of chemical and biological interest, and relevant state-of-the-art attosecond spectroscopy and theoretical methods have been documented in Refs. (Nisoli et al., 2017; Wörner et al., 2017; Merritt et al., 2021).

All the reported observations of charge migrations in different molecules are performed using various spectroscopic methods within pump-probe configuration. Direct imaging of charge migration in real-time and in real-space (four-dimensional) is still missing – one of the main themes of this thesis.

## 1.3 Aim of This Thesis

There are numerous theoretical works on charge migration in different molecules. However, there are still several open questions such as sensitivity of the charge migration with respect to the molecular structural and electronic symmetries. In other words, whether symmetry as a fundamental property of a molecule will be imprinted on the charge migration or can one deduce generic rules on charge migration based on the symmetries of the molecules? This thesis aims to address such questions. To investigate the role of molecular symmetries on charge migration, an overview about the choice of molecules is presented in Fig. 1.1. In this thesis, we will explore charge migration corresponding to valence electron excitation in neutral molecules.

Benzene as one of most symmetric molecules has been investigated from charge migration perspective in detail. Control over aromaticity in benzene is understood by analysing attosecond charge migration (Ulusoy and Nest, 2011). A pincer-type flow during charge migration in benzene has been established, which indicates

inactive role of a significant fraction of electrons during the charge migration. Furthermore, it has been found that the nature and direction of the charge migration can be controlled by selective excitation using optimized laser parameters (Hermann et al., 2016a; Jia et al., 2017; Hermann et al., 2017a, 2020). At this juncture, it is natural to envisage how the charge migration will alter if one reduces the symmetry of the molecule by transiting from six-membered benzene ( $\mathcal{D}_{6h}$  point group) to five-membered ring-shaped molecules. This will be the starting point of the present thesis. Both cyclopentene and cyclopentadiene are homocyclic and nonaromatic pentagon molecules of carbon atoms. Moreover, both molecules are ionic, making them less attractive for the present purpose. On the other hand, pyrrole, furan and oxazole are five-membered ring-shaped neutral molecules. Thus, these three molecules with  $\mathcal{C}_{2v}$  and  $\mathcal{C}_s$  point group symmetries will serve our first purpose to explore the role of symmetry reduction on charge migration.

To explore the role of the symmetry on charge migration, we will transit from a planar to non-planar molecule as a second example. Magnesium porphyrin is another most symmetric and planar molecule in which attosecond charge migration has been studied in detail (Nam et al., 2020; Tremblay et al., 2021; Barth and Manz, 2006; Barth et al., 2006; Köksal and Koç, 2017). Corroles have out-of-plane atoms which is a reason for the saddling in their molecular structure, whereas porphyrins are planar in nature. Corroles and porphyrins are macrocyclic organic molecules as they sustain a conjugation channel bearing a large number (18) of  $\pi$  electrons. Due to a slightly smaller number of atoms, corroles are commonly known as reduced dimensional models for porphyrins (Johnson and Kay, 1965), with whom they share similar electronic properties. The chemistry of porphyrins and corroles is a never-ending field of exciting problems, for both fundamental and practical reasons (Mingos and Dahl, 2012). Over the years, many significant research works have been performed to understand ultrafast light-induced processes in porphyrins from a theoretical perspective (Tremblay et al., 2021; Nam et al., 2020; Köksal and Koç, 2017; Barth and Manz, 2006; Barth et al., 2006). In contrast, corroles have not received similar attention in the context of light-induced ultrafast processes (Lemon, 2020). As a part of this thesis, we have taken a first step towards

exploring ultrafast charge migration in metal-coordinated corroles where we will explore the role of structural saddling on the charge migration in copper corrole.

After studying charge migration in molecules with certain symmetries, we will explore charge migration in molecules without any symmetry. For this purpose, chiral molecules are best suited. Chirality is a general property observed in nature, and can be defined as the geometric property of a molecule of being non-superposable on its mirror image. Enantiomers – a pair of chiral molecules – possess similar physical properties but they show strong enantiomeric preference during chemical reactions. Distinguishing and understanding the chirality of molecules is essential in a broad range of sciences. One example is the important role that homochirality plays in life on earth (Bada, 1995; Blackmond, 2010; Meierhenrich, 2013). Therefore, detecting and measuring the enantiomeric excess and handedness of chiral molecules play a crucial role in chemistry, biology and pharmacy (Mori, 2011; Fischer and Hache, 2005; Inoue and Ramamurthy, 2004). As a result, development of evermore reliable methods to discern enantiomers is an ongoing quest, which has received considerable attention in recent years. In this part of the thesis, we will explore how chiral control over coherent electronic motion can be achieved by choosing the different orientations of an ultrashort linearly polarized pulse, which is used to drive an ultrafast charge migration process by the excitation of a small number of low-lying excited states from the ground electronic state of R- and S-epoxypropane. Moreover, we will explore the conditions required to understand charge migration in oriented and floppy chiral molecules.

Another important aspect of this thesis is a four-dimensional imaging of charge migration. For this purpose, spatial representation of charge migration is essential. As the coherent electronic wavepacket associated with the charge migration evolves in time, the electronic charge distribution migrates from one point in space to another point within a molecule. Following the quantum version of the continuity equation, time-dependent electronic charge distribution and thus the charge migration is accompanied by time-dependent electronic flux density (EFD) (Sakurai, 2006). Not only the EFD provides mechanistic information about ultrafast process but also a directional representation of the spatial distribution of the charge migra-

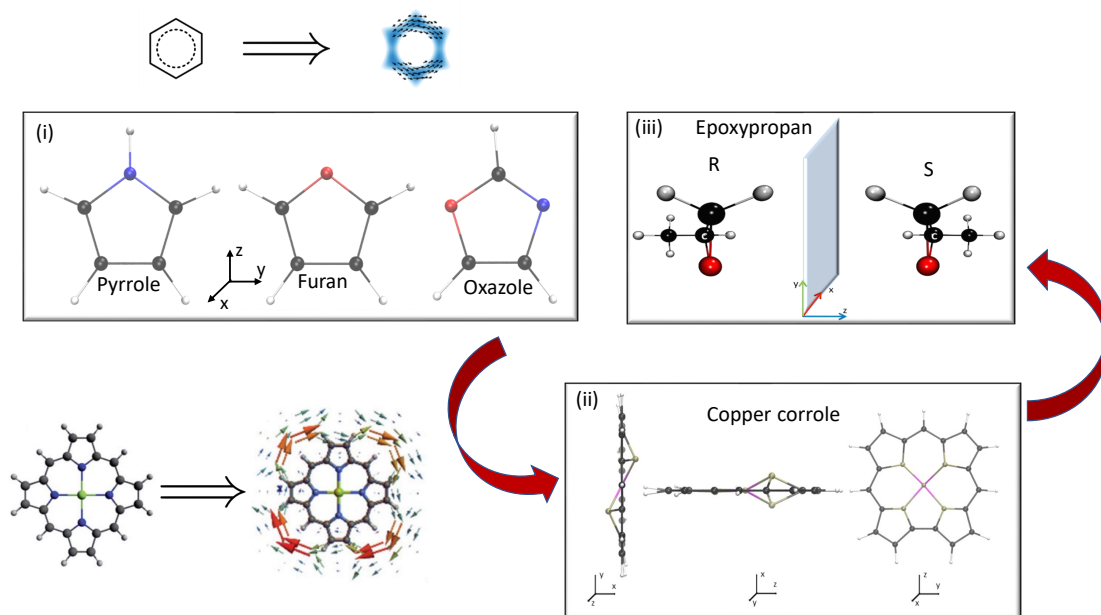


Figure 1.1: An illustration of the overview of the impact of molecular symmetry during laser-induced charge migration in different molecules. (i) Planar molecules pyrrole and furan with  $C_{2v}$  and oxazole with  $C_s$  point group symmetries, (ii) structural saddling in copper corrole with  $C_2$  symmetry and (iii) R- and S-epoxypropane with  $C_1$  symmetry. Results of benzene and magnesium porphyrin are adapted from (Hermann et al., 2020) and (Nam et al., 2020), respectively.

tion along the direction of flow. The EFD is a vector quantity, whereas the charge distribution is a scalar quantity. Over the years, EFD has emerged as an important method to gain detailed insights about the underlying mechanism of ultrafast charge migration in systems ranging from molecules to nano-materials (Barth and Manz, 2006; Barth et al., 2006; Nagashima and Takatsuka, 2009; Giri et al., 2020; Okuyama and Takatsuka, 2009; Giri et al., 2021, 2022; Shao et al., 2020; Hermann and Tremblay, 2016; Pohl et al., 2019; Shao et al., 2021; Sobottka et al., 2020; Diestler, 2012; Takatsuka and Yonehara, 2011; Patchkovskii, 2012; Okuyama and Takatsuka, 2012; Diestler et al., 2013; Takatsuka et al., 2014; Hermann et al., 2014; Yamamoto and Takatsuka, 2015; Hermann et al., 2016a; Bredtmann et al., 2014). In 2020, it was established that TRXD from an electronic wavepacket is related to the EFD associated with the charge migration. Laser-induced charge migration in benzene was used to establish this connection (Hermann et al., 2020). Following this work, charge migration and ring current associated with the hole wavepacket



in oxazole was discussed in the context of TRXD (Carrascosa et al., 2021). Also, stimulated resonant x-ray Raman process was used to prepare a hole wavepacket in oxazole and the resultant charge migration was imaged by TRXD (Yong et al., 2021). Recently, it was demonstrated that the combination of time-resolved electron and x-ray homodyne diffraction has potential to provide a real-space picture of charge migration in molecule without the influence of nuclear motion (Yong et al., 2022).

In this thesis, we will use time-dependent electronic charge distribution and associated EFD to unravel the influences of the molecular symmetries in the charge migration and its underlying mechanism in different molecules.

## 1.4 Outline

The thesis is primarily divided into six main chapters and bibliography.

A brief overview of ultrafast processes in matter is discussed in **Chapter 1**. The recent developments of attosecond physics with the generation of the coherent attosecond pulses and their key applications in atoms and solids are introduced. The concept of TRXD using ultrashort x-ray pulses within pump-probe configuration and the recent results of TRXD are discussed. Following the attosecond physics and TRXD, the notion of the charge migration with recent theoretical and experimental findings are presented. A detailed aim of the present thesis with an overview is offered at the end of this chapter.

**Chapter 2** is dedicated for the theoretical framework of inducing and four-dimensional imaging of the charge migration in molecules. A brief overview of the electronic structure theory, based on wave function and density functional methods, is presented. Concepts of time-dependent density functional theory and time-dependent configuration interaction are introduced to construct the laser-induced electronic wavepacket associated with the charge migration. A theory of electronic continuity equation is introduced for spatiotemporal analysis of the charge migration. This chapter ends with a brief theory of TRXD and technical details of the numerical simulations performed in this thesis .

In **Chapter 3**, we investigate a connection between the charge migration and molecular symmetry. For this purpose, charge migration in three planar molecules, pyrrole, furan and oxazole, is presented. The effects of the electronegativity of the foreign atoms are discussed by comparing the charge migration in pyrrole and furan. Moreover, the effect of symmetry reduction from  $C_{2v}$  to  $C_s$  is analysed by a comparative study of charge migration in oxazole with pyrrole and furan.

**Chapter 4** contains a detailed discussion on the effect of the molecular structural saddling on charge migration in copper corrole. A linearly polarized pulse is used to trigger the charge migration in copper corrole. Time-resolved difference electronic charge and flux densities are used to quantify the role of the saddling on charge migration, which is subsequently imaged by TRXD. The simulated results are compared for planes containing the saddling and plane without saddling at different instances of the charge migration. To ensure the impact of the saddling on the charge migration, we have also compared the static x-ray diffraction signal corresponding to ground states of copper corrole and copper porphyrin in which the structural saddling is absent and its structure is planar.

Charge migration in molecules without any symmetry, i.e., chiral molecules is investigated in **chapter 5**. The control over charge migration in space-oriented R- and S-enantiomers of epoxyp propane is discussed by tuning the parameters of linearly polarized laser pulse. In the first case, we have applied a linearly polarized pulse along an axis to induce charge migration in both enantiomers. In the second case, we tune the direction of the polarization of the linear pulse in a plane containing normal axis. This results drastically different charge migration in both enantiomers. We have also investigated the charge migration in loosely-oriented floppy chiral molecules. Time-resolved difference electronic charge and flux densities are employed to validate our findings. Furthermore, TRXD is employed to image charge migration in both enantiomers. This chapter is concluded with the introduction of an asymmetry parameter associated with TRXD to discern the enantiomers.

We conclude our findings in this thesis with future direction in **Chapter 6**.

## Chapter 2

# Theoretical Framework for Laser-Induced Charge Migration

Atomic units are used throughout in this chapter unless stated otherwise. The time evolution of an electronic charge distribution in a molecule within non-relativistic framework can be described by time-dependent Schrödinger equation (TDSE) as

$$i\frac{d}{dt}|\Psi_{\text{tot}}(\mathbf{r}, \mathbf{R}, t)\rangle = \mathcal{H}(t)|\Psi_{\text{tot}}(\mathbf{r}, \mathbf{R}, t)\rangle, \quad (2.0.1)$$

where  $\mathbf{r}$  and  $\mathbf{R}$  represent the electronic and nuclear coordinates, respectively. The total time-dependent Hamiltonian,  $\mathcal{H}(t)$ , can be written as a sum of time-independent Hamiltonian for a molecule,  $\mathcal{H}_0$ , and the time-dependent interaction Hamiltonian between a molecule and a laser,  $\mathcal{H}_{\text{int}}(t)$ , as

$$\mathcal{H}(t) = \mathcal{H}_0 + \mathcal{H}_{\text{int}}(t). \quad (2.0.2)$$

The molecular Hamiltonian within Born-Oppenheimer approximation can be written as

$$\mathcal{H}_0 = -\sum_i \frac{1}{2} \nabla_i^2 - \sum_{A,i} \frac{Z_A}{|\mathbf{r}_{iA}|} + \frac{1}{2} \sum_{i \neq j} \frac{1}{|\mathbf{r}_{ij}|}, \quad (2.0.3)$$

where the first term stands as the kinetic energy for electrons followed by the electron-nucleus and electron-electron interaction terms with  $Z_A$  as the nuclear

charge of the  $A^{\text{th}}$  atom (Tannor, 2007). The applicability of the Born-Oppenheimer approximation is justified in this thesis as we are interested in the laser-induced charge migration taking place on attosecond timescale. Within Born-Oppenheimer approximation, TDSE for electrons with a fixed nuclear configuration is written as

$$i\frac{d}{dt}|\Psi(\mathbf{r}, t)\rangle = \mathcal{H}(t)|\Psi(\mathbf{r}, t)\rangle, \quad (2.0.4)$$

where time-dependent wave function,  $|\Psi(\mathbf{r}, t)\rangle$ , is expanded as

$$|\Psi(\mathbf{r}, t)\rangle = \sum_k C_k(t)|\Phi_k(\mathbf{r})\rangle = \sum_k |\Psi_k(\mathbf{r}, t)\rangle. \quad (2.0.5)$$

Here,  $C_k(t)$  is a time-dependent expansion coefficient and  $|\Phi_k(\mathbf{r})\rangle$  is a time-independent multi-electronic wave function. Solving the TDSE for electrons in the presence of a laser is a challenging task. In the following, we will first discuss theoretical methods to obtain  $|\Phi_k(\mathbf{r})\rangle$ , which will be followed by techniques to construct time-dependent coefficient  $C_k(t)$  in the presence of a laser.

## 2.1 Electronic Structure Theory

It is well-known that the time-independent molecular Hamiltonian,  $\mathcal{H}_0$ , is not exactly solvable except for few systems such as hydrogen (Szabo and Ostlund, 2012). The difficulty in solving  $\mathcal{H}_0$  is a drastic increase in computational cost toward the exact solution as the number of electrons increases. A set of appropriate approximations and a large number of mathematical operations are employed to obtain solutions of  $\mathcal{H}_0$  as given in Eq. (2.0.3), upto some level of accuracy. In the following, we will discuss two approximate methods to solve  $\mathcal{H}_0$ : the first one relies on wave function based approach, whereas the other is density-based approach.

### 2.1.1 Wave Function Based Methods

Independent-electron model is the simplest approach to solve  $\mathcal{H}_0$  in which electrons are considered as independent and do not interact with each other. Within this model, electron-electron interaction is completely ignored, i.e., the last term of

Eq. (2.0.3) is omitted. Going beyond the independent-electron model is Hartree-Fock method, which accounts average interaction among the electrons and the multi-electronic wave function is expressed in the form of a Slater determinant. Numerous theoretical methods are developed over the years by considering different levels of the electron-electron correction to improve the results obtained by Hartree-Fock method. These methods are known as post Hartree-Fock method. Configuration Interaction (CI) method is one of the most popular and robust post Hartree-Fock methods (Szabo and Ostlund, 2012; Jensen, 2017; Helgaker et al., 2014).

Total electronic wave function within CI method is expressed in terms of the linear combination of several Slater determinants as

$$|\Phi_{\text{CI}}^{(\lambda)}\rangle = D_0^{(\lambda)}|\Phi_{\text{HF}}^{(0)}\rangle + \sum_{ar} D_a^{r(\lambda)}|\Phi_{\text{HF}}^{(0)}\rangle_a^r + \sum_{abrs} D_{ab}^{rs(\lambda)}|\Phi_{\text{HF}}^{(0)}\rangle_{ab}^{rs} + \cdots, \quad (2.1.1)$$

where  $|\Phi_{\text{HF}}^{(0)}\rangle$  is the Hartree-Fock wave function, which is treated as a reference wave function,  $D'$ 's are coefficients of the configuration interaction. Electrons are excited from occupied  $\{a, b, \cdots\}$  to virtual  $\{r, s, \cdots\}$  molecular orbitals to construct the excited-state Slater determinants from a ground-state Slater determinant. An exact solution of the molecular Hamiltonian can be obtained by considering all possible excitations. However, the number of possible excitations increases drastically as the number of electrons in a molecular system increases, which makes full CI numerically impractical to implement for a moderate size molecular system. To make a delicate balance between the computational cost and accuracy of the wave function, either the rank of the excitation can be restricted to CI singles (CIS), or CI doubles (CID) and so on, or the excitation can be restricted to a specific configuration space. We have considered only single excitations to all the results presented in this thesis.

Hartree-Fock and post Hartree-Fock methods are computationally expensive as they have to keep track of all the spatial coordinates of all the electrons in a molecule explicitly. To reduce computational cost, an alternate density-based method becomes popular and practical over the years. In the following section,

let us briefly discuss the mathematical framework of Density Functional Theory (DFT).

### 2.1.2 Density Based Methods

Let us start our discussion about DFT by writing time-independent Schrödinger equation corresponding to  $\mathcal{H}_0$  as

$$[\mathcal{T}_e + \mathcal{V}_{ei} + \mathcal{W}_{ee}] |\Psi_0(\mathbf{r})\rangle = \mathcal{E}_0 |\Psi_0(\mathbf{r})\rangle, \quad (2.1.2)$$

where  $\mathcal{T}_e$  is the kinetic energy operator,  $\mathcal{V}_{ei}$  is the attraction between electron and nucleus, and  $\mathcal{W}_{ee}$  is the electron-electron interaction terms.  $|\Psi_0(\mathbf{r})\rangle$  and  $\mathcal{E}_0$  are the ground state wave function and corresponding energy, respectively.  $\mathcal{V}_{ei}$  characterize the molecular system within non-relativistic framework, whereas the form of  $\mathcal{T}_e$  and  $\mathcal{W}_{ee}$  are universal.

Hohenberg and Kohn demonstrated in their seminal work that any observable of a molecular system can be deduced from their ground-state density,  $\rho_0(\mathbf{r})$ , without the requirement of a multi-electronic wave function  $|\Psi_0(\mathbf{r})\rangle$  (Hohenberg and Kohn, 1964). Moreover, a one-to-one correspond between  $v_{ei}(\mathbf{r})$  and  $\rho_0(\mathbf{r})$  has been established with  $|\Psi_0(\mathbf{r})\rangle$  is a unique functional of  $\rho_0(\mathbf{r})$ . This leads to the conclusion that the ground-state density contains all the relevant information of a molecular system. This is the foundation of DFT. The ground-state energy functional within DFT is defined as

$$E[\rho_0] = \langle \Psi[\rho_0] | \mathcal{H}_0 | \Psi[\rho_0] \rangle. \quad (2.1.3)$$

However, the exact form of the energy functional can be obtained variationally. The energy functional can be expressed in terms of single-particle orbitals,  $\phi_\mu$ , as

$$E[\rho] = T_s[\rho] + W_H[\rho] + E_{xc}[\rho] + \int d\mathbf{r} \rho(\mathbf{r}) v_{ei}(\mathbf{r}). \quad (2.1.4)$$

Here,  $T_s$  is the kinetic energy of a non-interacting system with electronic density,

$\rho$ , and can be written as

$$T_s[\rho] = -\frac{1}{2} \sum_{i=\mu}^N \int d\mathbf{r} \phi_\mu^*(\mathbf{r}) \nabla^2 \phi_\mu(\mathbf{r}), \quad (2.1.5)$$

and the classical Hartree term  $W_H$  is expressed as

$$W_H[\rho] = \frac{1}{2} \int d\mathbf{r} \int d\mathbf{r}' \frac{\rho(\mathbf{r})\rho(\mathbf{r}')}{|\mathbf{r} - \mathbf{r}'|}. \quad (2.1.6)$$

The exchange-correlation energy functional,  $E_{xc}$ , contains all information about a molecular system by construction. Kohn-Sham (KS) equation is obtained by minimizing the energy functional in Eq. (2.1.4) using variational principle as (Kohn and Sham, 1965)

$$\left( -\frac{1}{2} \nabla^2 + v_s[\rho_0](\mathbf{r}) \right) |\phi_\mu(\mathbf{r})\rangle = \epsilon_\mu |\phi_\mu(\mathbf{r})\rangle. \quad (2.1.7)$$

Here, the effective single-particle potential is defined as

$$v_s[\rho](\mathbf{r}) = v_{ei}[\rho](\mathbf{r}) + v_H[\rho](\mathbf{r}) + v_{xc}[\rho](\mathbf{r}). \quad (2.1.8)$$

Here, the Hartree and exchange-correlation potentials are defined as  $v_H[\rho](\mathbf{r}) = \partial W_H[\rho] / \partial \rho(\mathbf{r})$ , and  $v_{xc}[\rho](\mathbf{r}) = \partial E_{xc}[\rho] / \partial \rho(\mathbf{r})$ , respectively. KS equation is equivalent to single-electron Schrödinger equation, and its solution is obtained self consistently.

### Time-Dependent Density Functional Theory

Basic idea of the ground-state DFT is extended to Time-Dependent DFT (TDDFT) to calculate the excitation energies of the excited states, frequency-dependent response properties, and other time-dependent properties (Gross et al., 1996; Marques and Gross, 2004; Marques et al., 2012; Casida, 2009). The building blocks of the TDDFT are two theorems: Runge-Gross theorem (Runge and Gross, 1984), which is a time-dependent extension of the Hohenberg-Kohn theorem (Hohenberg and Kohn, 1964), and the Van Leeuwen theorem (Van Leeuwen, 1999). Runge

and Gross showed that, for a multi-electronic molecular system evolving from a ground-state  $|\Psi(t = t_0)\rangle = |\Psi_0\rangle$ , there is a one-to-one mapping between external potential  $v_{ext}(\mathbf{r}, t)$  and time-dependent density  $\rho(\mathbf{r}, t)$  with  $\mathcal{V}_{ext}(t) = \sum_{i=\mu}^N v_{ext}(\mathbf{r}, t)$  as the scalar external potential. Time-dependent KS (TDKS) equation analogous to single-electron TDSE can be written as

$$i \frac{\partial}{\partial t} |\phi_\mu(\mathbf{r}, t)\rangle = \left( -\frac{1}{2} \nabla^2 + v_s(\mathbf{r}, t) \right) |\phi_\mu(\mathbf{r}, t)\rangle. \quad (2.1.9)$$

Here, TDKS orbitals of non-interacting electrons are used to obtain the time-dependent density as

$$\rho(\mathbf{r}, t) = \sum_{i=\mu}^N |\phi_\mu(\mathbf{r}, t)|^2. \quad (2.1.10)$$

The time-dependent density evolves in the presence of the TDKS potential. In general, the exact expression of the time-dependent exchange-correlation potential is not known. Thus, it is not very straightforward to solve TDKS equation as given in Eq. (2.1.9). In this thesis, we have adopted first-order linear response approach to solve Eq. (2.1.9).

Linear-Response TDDFT (LR-TDDFT) is a first-order perturbative solution of the TDKS equation, which describes the molecular system in the presence of a weak perturbation (Gross et al., 1996; Marques and Gross, 2004; Marques et al., 2012). The first-order correction to density within LR-TDDFT approach can be written using Taylor series expansion as (Ernzerhof, 1994)

$$\rho^{(1)}(\mathbf{r}, t) = \int \int dt' d\mathbf{r}' \chi_{\text{eff}}(\mathbf{r}, t, \mathbf{r}', t') \hat{v}_{\text{eff}}^{(1)}(\mathbf{r}', t'). \quad (2.1.11)$$

Here,  $\hat{v}_{\text{eff}}^{(1)}(\mathbf{r}', t')$  is the first-order correction of the TDKS potential and consists of three terms same as mentioned in Eq. (2.1.8). The last term due to non-trivial multi-electronic effects, i.e., the exchange correlation term, has the following form

$$\hat{v}_{\text{XC}}^{(1)}(\mathbf{r}, t) = \int \int dt' d\mathbf{r}' \hat{f}_{\text{XC}}(\mathbf{r}, t, \mathbf{r}', t') \rho^{(1)}(\mathbf{r}', t'), \quad (2.1.12)$$

where the time-dependent exchange-correlation kernel,  $\hat{f}_{\text{XC}}(\mathbf{r}, t, \mathbf{r}', t')$ , can be writ-



ten as

$$\hat{f}_{\text{XC}}(\mathbf{r}, t, \mathbf{r}', t') = \left. \frac{\delta \hat{v}_{\text{XC}}^{(1)}[\rho](\mathbf{r}, t)}{\delta \rho(\mathbf{r}', t')} \right|_{\rho(\mathbf{r}, t=0)}. \quad (2.1.13)$$

The interacting and non-interacting response functions are connected using the notion of the Fourier space. The density-density response function in the Fourier space is

$$\chi_{\text{eff}}(\mathbf{r}, \mathbf{r}', \omega) = \sum_{ar} \left[ \frac{\rho_{ar}(\mathbf{r}') \rho_{ra}(\mathbf{r})}{\omega - \omega_{ra} + i\eta} - \frac{\rho_{ra}(\mathbf{r}') \rho_{ar}(\mathbf{r})}{\omega + \omega_{ra} + i\eta} \right], \quad (2.1.14)$$

where a transition from an occupied molecular orbital “ $a$ ” to a virtual molecular orbital “ $r$ ” is considered. To solve the above equation self consistently, it can be modified like a Dyson-type equation as

$$\begin{aligned} \chi(\mathbf{r}, \mathbf{r}', \omega) &= \chi_{\text{eff}}(\mathbf{r}, \mathbf{r}', \omega) \\ &+ \int \int d\mathbf{r}'' d\mathbf{r}''' \chi(\mathbf{r}, \mathbf{r}'', \omega) \left[ \frac{1}{|\mathbf{r}'' - \mathbf{r}'''}| + \hat{f}_{\text{XC}}(\mathbf{r}'', \mathbf{r}''', \omega) \right] \chi_{\text{eff}}(\mathbf{r}''', \mathbf{r}', \omega). \end{aligned}$$

The energies of the excited electronic states can be extracted from the poles of  $\chi(\mathbf{r}, \mathbf{r}', \omega)$  with transition frequencies  $\omega_{ra} = (\epsilon_r - \epsilon_a)$ . A non-Hermitian eigenvalue equation, known as Casida equation, is solved to obtain the excitation energies of electronic states. Moreover, by eliminating the de-excitation process using Tamm-Doncoff approximation, we arrive the following equation in compact form as (Hirata and Head-Gordon, 1999)

$$\mathbf{A}\mathbf{X}_\lambda = \Omega_\lambda \mathbf{X}_\lambda. \quad (2.1.15)$$

The above equation is equivalent to the CIS method. Within Tamm-Doncoff approximation, a CIS-type wave function can be expressed explicitly for each excited state. This method thus works as a bridge between the CIS and TDDFT methods and termed as hybrid TDDFT-CI approach.

So far, we have discussed methods to solve  $\mathcal{H}_0$  within Born-Oppenheimer approximation. The stationary part of the time-dependent wave function  $|\Phi_k(\mathbf{r})\rangle$  can be obtained using hybrid TDDFT-CI approach. In this thesis, we have expressed these time-independent wave function as a linear combination of the CIS functions as given in Eq. (2.1.1). In the following, we will present a brief discussion about

the theory of laser-induced charge migration – the main focus of this thesis.

## 2.2 Laser-Induced Charge Migration

To characterize the charge migration in a molecular system, density operator is the key quantity and can be written as

$$\hat{\varrho}(\mathbf{r}, t) = |\Psi(\mathbf{r}, t)\rangle\langle\Psi(\mathbf{r}, t)|. \quad (2.2.1)$$

The time evolution of an electronic charge distribution can be described in terms of the reduced density matrix formalism where the dissipation acts as the effect of the environment. Let us introduce the dissipative Liouville-von Neumann (LvN) equation to characterize such type of dynamics in a molecule as

$$\frac{\partial}{\partial t}\hat{\varrho}(\mathbf{r}, t) = -i[\mathcal{H}_{\text{int}}(t), \hat{\varrho}(\mathbf{r}, t)] + \mathcal{L}_D\hat{\varrho}(\mathbf{r}, t), \quad (2.2.2)$$

where  $\mathcal{L}_D$  is the dissipative Liouvillian. The population of the electronic states can be extracted from the diagonal elements in the CIS eigenstate basis. Thus, the above equation is expressed in terms of Lindblad form. The dissipative Liouvillian within Lindblad formalism can be written as

$$\mathcal{L}_D\hat{\varrho}(\mathbf{r}, t) = \frac{1}{2}\sum_d\left\{\left[\hat{L}_d\hat{\varrho}(\mathbf{r}, t), \hat{L}_d^\dagger\right] + \left[\hat{L}_d, \hat{\varrho}(\mathbf{r}, t)\hat{L}_d^\dagger\right]\right\}. \quad (2.2.3)$$

Here,  $\hat{L}_d$  is the Lindblad operator and has the following form

$$\hat{L}_d = \sqrt{\Gamma_{\nu\rightarrow\lambda}}|\Phi_\lambda(\mathbf{r})\rangle\langle\Phi_\nu(\mathbf{r})|, \quad (2.2.4)$$

where  $\Gamma_{\nu\rightarrow\lambda}$  is the transition rate between  $|\Phi_\nu\rangle$  and  $|\Phi_\lambda\rangle$  states, and can be estimated using Fermi's Golden rule.

The density operator can be expressed in a matrix form using a orthonormal basis  $\{|\Phi_k(\mathbf{r})\rangle\}$ , and the matrix elements can be written as

$$\varrho_{kl}(t) = \langle\Phi_k(\mathbf{r})|\hat{\varrho}(\mathbf{r}, t)|\Phi_l(\mathbf{r})\rangle. \quad (2.2.5)$$

## 2.2. Laser-Induced Charge Migration

---

Before we discuss the solution of Eq. (2.2.2) in terms of the density matrix, let us write the interaction Hamiltonian responsible for the charge migration as

$$\mathcal{H}_{\text{int}}(t) = -\hat{\mu} \cdot \mathbf{E}(t), \quad (2.2.6)$$

where  $\hat{\mu}$  is the dipole operator and  $\mathbf{E}(t)$  is the electric field of the laser pulse.

The time evolution of the direct terms of the density matrix in Eq. (2.2.2) can be written as

$$\frac{d\rho_{mn}(t)}{dt} = -iE_j(t) \sum_i (\mu_{ni}\hat{\rho}_{in} - \hat{\rho}_{ni}\mu_{in}) + \sum_i (\Gamma_{i \rightarrow n}\hat{\rho}_{ii} - \Gamma_{n \rightarrow i}\hat{\rho}_{nn}). \quad (2.2.7)$$

Here,  $E_j$  is the  $j^{\text{th}}$ -component of  $\mathbf{E}(t)$ , which depends on the polarization of the laser pulse, and  $\mu_{ni} = \langle \Phi_n | \hat{\mu} | \Phi_i \rangle$ . Similarly, the time-evolution of the cross terms of the density matrix is written as

$$\frac{d\rho_{mn}(t)}{dt} = -i\omega_{mn}\hat{\rho}_{mn} - iE_j(t) \sum_i (\mu_{mi}\hat{\rho}_{in} - \hat{\rho}_{mi}\mu_{in}) - \gamma_{mn}\hat{\rho}_{mn}, \quad (2.2.8)$$

where the dephasing rate is  $\gamma_{mn} = \gamma_{nm} = (1/2) \sum_l (\Gamma_{m \rightarrow l} + \Gamma_{n \rightarrow l})$ . The diagonal elements of the density matrix,  $\rho_{kk}(t)$ , are the probability of finding a molecular system in the basis  $\{|\Phi_k\rangle\}$  and known as population of the  $k^{\text{th}}$  electronic state. The time-dependent expansion coefficient in Eq. (2.0.5) can be written as  $C_k(t) = \rho_{kk}(T_p) \exp(-iE_k t)$  with  $T_p$  as the pulse duration of laser pulse and  $E_k$  is the energy of the  $k^{\text{th}}$  electronic state.

After constructing the time-dependent expansion coefficient and the wave function, let us proceed to understand laser-driven charge migration in terms of electronic charge and flux densities in the following section.

### 2.2.1 Electronic Continuity Equation

The flow of an electronic charge distribution after the end of the laser pulse can be visualized in terms of time-dependent electron density, which can be calculated from the expectation value of the density operator after solving Eq. (2.2.2). The

time-dependent electron density using Eq. (2.0.5) can be written as

$$\rho(\mathbf{r}, t) = \sum_{kl} C_k^*(t) C_l(t) \langle \Phi_k(\mathbf{r}) | \hat{\rho}(\mathbf{r}) | \Phi_l(\mathbf{r}) \rangle. \quad (2.2.9)$$

Here, the one-electron density operator,  $\hat{\rho}(\mathbf{r})$ , has the following form

$$\hat{\rho}(\mathbf{r}) = \sum_k \delta(\mathbf{r} - \mathbf{r}_k). \quad (2.2.10)$$

The time-dependent electron density allows us to visualize the temporal evolution of an electronic charge distribution in space. Moreover, the direction of the flow of the charge distribution can be obtained by time-dependent electronic flux density, which is written as

$$\mathbf{j}(\mathbf{r}, t) = \sum_{kl} C_k^*(t) C_l(t) \langle \Phi_k(\mathbf{r}) | \hat{j}(\mathbf{r}) | \Phi_l(\mathbf{r}) \rangle. \quad (2.2.11)$$

Here, the flux density operator,  $\hat{j}$ , has the following form

$$\hat{j}(\mathbf{r}) = \frac{1}{2} \sum_k [\delta(\mathbf{r} - \mathbf{r}_k) \hat{p}_k - \hat{p}_k^\dagger \delta(\mathbf{r} - \mathbf{r}_k)], \quad (2.2.12)$$

where the momentum of the  $k^{\text{th}}$  electron is given by the momentum operator as  $\hat{p}_k = -i\nabla_k$ .

The connection between the time-dependent electronic charge and flux densities can be established by taking a time-derivative of the density matrix, and is expressed as

$$\frac{\partial}{\partial t} \rho(\mathbf{r}, t) = -\nabla \cdot \mathbf{j}(\mathbf{r}, t). \quad (2.2.13)$$

This is known as the electronic continuity equation that maintains the charge conservation of a molecular system in terms of  $\rho(\mathbf{r}, t)$  and  $\mathbf{j}(\mathbf{r}, t)$ .

In general, transition dipole moments in length and velocity gauges are compared to ensure the accuracy of a wave function obtained via "high-level" quantum chemistry calculations. The dipole moments in length and velocity gauges can be obtained from electronic charge and electronic current densities, respectively.

Till now, we have discussed how TDSE can be solved and laser-induced charge migration can be studied using electronic charge and flux densities. In the following section, we will briefly discuss the theoretical framework of time-resolved x-ray diffraction (TRXD) to image the laser-induced charge migration.

## 2.3 Time-Resolved X-ray Diffraction

In this thesis, we are interested to employ non-resonant time-resolved x-ray diffraction to capture temporarily-evolving charge distribution. Moreover, we have applied quantum electrodynamics (QED) treatment of x-ray-molecule interaction. The corresponding interaction Hamiltonian for TRXD within QED framework can be written as (Craig and Thirunamachandran, 1998)

$$\mathcal{H}_{\text{int}}^x = \frac{\alpha^2}{2} \int d\mathbf{r} \psi^\dagger(\mathbf{r}) \mathcal{A}^2(\mathbf{r}) \psi(\mathbf{r}), \quad (2.3.1)$$

where  $\alpha$  is the fine-structure constant,  $\psi^\dagger(\mathbf{r})[\psi(\mathbf{r})]$  is electron creation (annihilation) field operator and  $\mathcal{A}(\mathbf{r})$  is a vector potential of x-ray, which has the following form

$$\mathcal{A}(\mathbf{r}) = \sum_{\mathbf{k},s} \sqrt{\frac{2\pi}{V\omega_{\mathbf{k}}\alpha^2}} \{ \hat{\mathbf{a}}_{\mathbf{k},s} \epsilon_{\mathbf{k},s} e^{i\mathbf{k}\cdot\mathbf{r}} + \hat{\mathbf{a}}_{\mathbf{k},s}^\dagger \epsilon_{\mathbf{k},s}^* e^{-i\mathbf{k}\cdot\mathbf{r}} \}. \quad (2.3.2)$$

Here,  $\epsilon_{\mathbf{k},s}$  is the polarization vector with  $s$  as the polarization index and  $\omega_{\mathbf{k}}$  is the photon energy of the  $\mathbf{k}^{\text{th}}$  mode.  $\hat{\mathbf{a}}_{\mathbf{k},s}(\hat{\mathbf{a}}_{\mathbf{k},s}^\dagger)$  is the photon creation (annihilation) operator and  $V$  is the quantization volume.

Differential Scattering Probability (DSP) is the key quantity in TRXD, which represents the number of diffracted photons per unit solid angle and is written as

$$\frac{dP}{d\Omega} = \frac{V\alpha^3}{(2\pi)^3} \int_0^\infty d\omega_{\mathbf{k}_s} \omega_{\mathbf{k}_s}^2 \sum_j \sum_{\{n'\}} \langle \Phi_j(\mathbf{r}); \{n'\} | \hat{\rho}_f(t) | \Phi_j(\mathbf{r}); \{n'\} \rangle. \quad (2.3.3)$$

Here,  $\hat{\rho}_f$  is the final density operator of the entire system, i.e., x-ray and molecule.  $|\{n'\}\rangle$  represents a complete set of numbers that specify the number of photons in all field modes. The total density operator at the time of measurement can be

written as

$$\hat{\rho}_f(t) = \lim_{t_f \rightarrow \infty} \lim_{t_0 \rightarrow -\infty} \hat{U}_{\text{tot}}(t_f, t_0) \hat{\rho}_{\text{in}}^s \hat{U}_{\text{tot}}^\dagger(t_f, t_0), \quad (2.3.4)$$

where  $\hat{U}_{\text{tot}}(t_f, t_0)$  is the total time-evolution operator. First-order time-dependent perturbation theory is employed to evaluate the first-order correction to the density operator as

$$\begin{aligned} \hat{\rho}^{(1)} &= \lim_{t_f \rightarrow \infty} \lim_{t_0 \rightarrow -\infty} \sum_{\{n\}, \{\bar{n}\}} \hat{\rho}_{\{n'\}, \{\bar{n}\}}^x \\ &\times \int_{t_0}^{t_f} \int_{t_0}^{t_f} dt_1 dt_2 \times \left[ \hat{U}_{\text{tot}}(t_f, t_1) \mathcal{H}_{\text{int}}^x \hat{U}_{\text{tot}}(t_1, t_0) |\Psi_{\{n\}}^{(0)}(\mathbf{r}, t_0)\rangle \right. \\ &\times \langle \Psi_{\{\bar{n}\}}^{(0)}(\mathbf{r}, t_0) | \hat{U}_{\text{tot}}^\dagger(t_2, t_0) \mathcal{H}_{\text{int}}^{x\dagger} \hat{U}_{\text{tot}}^\dagger(t_f, t_2) \rangle \left. \right]. \end{aligned} \quad (2.3.5)$$

Here,  $\hat{\rho}_{\{n'\}, \{\bar{n}\}}^x$  represents the populations and coherences of all the occupied field modes associated with the incident x-ray pulse.

After substituting the expressions from Eqs. (2.3.1), (2.3.2), and (2.3.5) to Eq. (2.3.3), the expression of DSP can be written as

$$\begin{aligned} \frac{dP}{d\Omega} &= \sum_{\mathbf{k}_1, s_1, \mathbf{k}_2, s_2} \int_{-\infty}^{\infty} \int_{-\infty}^{\infty} dt_1 dt_2 \int_0^{\infty} d\omega_{\mathbf{k}_s} \\ &\times \frac{\omega_{\mathbf{k}_s} \alpha^3}{2\pi V \sqrt{\omega_{\mathbf{k}_1}, \omega_{\mathbf{k}_1}}} (\epsilon_{\mathbf{k}_1, s_1} \cdot \epsilon_{\mathbf{k}_s, s_s}^*) (\epsilon_{\mathbf{k}_2, s_2}^* \cdot \epsilon_{\mathbf{k}_s, s_s}) \\ &\times \left[ \int d\mathbf{r} \int d\mathbf{r}' \langle \Psi(\mathbf{r}, t_2) | \hat{\rho}(\mathbf{r}') \hat{U}(t_2, t_1) \hat{\rho}(\mathbf{r}) | \Psi(\mathbf{r}, t_1) \rangle \right. \\ &\times e^{-i(\mathbf{k}_2 - \mathbf{k}_s) \cdot \mathbf{r}'} e^{i(\mathbf{k}_1 - \mathbf{k}_s) \cdot \mathbf{r}} \text{Tr}[\hat{\rho}_{\text{in}}^x \hat{a}_{\mathbf{k}_2, s_2}^\dagger \hat{a}_{\mathbf{k}_1, s_1}] e^{-i\omega_{\mathbf{k}_1} t_1} e^{i\omega_{\mathbf{k}_2} t_2} e^{-i\omega_{\mathbf{k}_s} (t_2 - t_1)} \left. \right], \end{aligned}$$

where

$$\text{Tr}[\hat{\rho}_{\text{in}}^x \hat{a}_{\mathbf{k}_2, s_2}^\dagger \hat{a}_{\mathbf{k}_1, s_1}] = \sum_{\{m\}} \sum_{\{n\}, \{\bar{n}\}} \rho_{\{n\}, \{\bar{n}\}}^x \langle \{m\} | \hat{a}_{\mathbf{k}_1, s_1} | \{n\} \rangle \times \langle \{\bar{n}\} | \hat{a}_{\mathbf{k}_2, s_2}^\dagger | \{m\} \rangle. \quad (2.3.6)$$

Here,  $\{m\} = \hat{a}_{\mathbf{k}_{1(2)}, s_{1(2)}} | \{n\} \rangle$ .

Let us introduced two new time variables as  $\gamma = \frac{t_1 + t_2}{2}$  and  $\delta = t_2 - t_1$  to simplify the expression of DSP. Moreover, we can also replace  $\epsilon_{\mathbf{k}_1, s_1}$  and  $\epsilon_{\mathbf{k}_2, s_2}$  with  $\epsilon_{\mathbf{k}_{\text{in}}, s_{\text{in}}}$  as x-ray pulse has small bandwidth and angular spread. Using these above

approximations the expression for DSP can be written as

$$\begin{aligned} \frac{dP}{d\Omega} &= \frac{d\sigma_{\text{th}}}{d\Omega} \int_{-\infty}^{\infty} d\gamma \int_{-\infty}^{\infty} d\delta \int_0^{\infty} d\omega_{\mathbf{k}_s} \frac{\omega_{\mathbf{k}_s}}{(2\pi\omega_{\mathbf{k}_{in}})^2 \alpha} e^{-i\omega_{\mathbf{k}_s}\delta} \\ &\times \int d\mathbf{r} \int d\mathbf{r}' \left\langle \Psi\left(\mathbf{r}, \gamma + \frac{\delta}{2}\right) \left| \hat{\rho}(\mathbf{r}') \hat{U}\left(\gamma + \frac{\delta}{2}, \gamma - \frac{\delta}{2}\right) \hat{\rho}(\mathbf{r}) \right| \Psi\left(\mathbf{r}, \gamma - \frac{\delta}{2}\right) \right\rangle \\ &\times e^{-i\mathbf{k}_s \cdot (\mathbf{r} - \mathbf{r}')} G^{(1)}\left(\mathbf{r}', \gamma + \frac{\delta}{2}; \mathbf{r}, \gamma - \frac{\delta}{2}\right), \end{aligned} \quad (2.3.7)$$

where  $d\sigma_{\text{th}}/d\Omega$  is the Thomson scattering cross section and  $G^{(1)}(\mathbf{r}', \gamma + \frac{\delta}{2}; \mathbf{r}, \gamma - \frac{\delta}{2})$  is the first-order correlation function for x-ray pulse and has the following form

$$\begin{aligned} G^{(1)}\left(\mathbf{r}', \gamma + \frac{\delta}{2}; \mathbf{r}, \gamma - \frac{\delta}{2}\right) &= \frac{2\pi\omega_{\mathbf{k}_{in}}}{V} \sum_{\mathbf{k}_1, s_1, \mathbf{k}_2, s_2} \text{Tr}[\hat{\rho}_{\text{in}}^x \hat{a}_{\mathbf{k}_2, s_2}^\dagger \hat{a}_{\mathbf{k}_1, s_1}] \\ &\times e^{i(\omega_{\mathbf{k}_2} - \omega_{\mathbf{k}_1})\gamma} e^{i(\omega_{\mathbf{k}_2} + \omega_{\mathbf{k}_1})\frac{\delta}{2}} e^{-i\mathbf{k}_2 \cdot \mathbf{r}'} e^{i\mathbf{k}_1 \cdot \mathbf{r}}. \end{aligned}$$

For a coherent ensemble of x-ray pulses with a coherence length larger than the size of the object,  $\mathbf{k}_1$  and  $\mathbf{k}_2$  can be approximated to  $\mathbf{k}_{in}$ . Under this approximation, the expression for DSP can be rewritten as

$$\begin{aligned} \frac{dP}{d\Omega} &= \frac{d\sigma_{\text{th}}}{d\Omega} \int_0^{\infty} d\omega_{\mathbf{k}_s} \frac{\omega_{\mathbf{k}_s}}{\omega_{\mathbf{k}_{in}}} \int_{-\infty}^{\infty} d\gamma \frac{I(\mathbf{r}_0, \gamma)}{\omega_{\mathbf{k}_{in}}} \int_{-\infty}^{\infty} \frac{d\delta}{2\pi} C(\delta) e^{-i(\omega_{\mathbf{k}_s} - \omega_{\mathbf{k}_{in}})\delta} \\ &\times \int d\mathbf{r} \int d\mathbf{r}' \left\langle \Psi\left(\mathbf{r}, \gamma + \frac{\delta}{2}\right) \left| \hat{\rho}(\mathbf{r}') e^{-i\mathcal{H}_0\delta} \hat{\rho}(\mathbf{r}) \right| \Psi\left(\mathbf{r}, \gamma - \frac{\delta}{2}\right) \right\rangle e^{-i\mathbf{Q} \cdot (\mathbf{r} - \mathbf{r}')}, \end{aligned}$$

where the pulse duration,  $\tau$ , dependent term is included in  $C(\delta) = \exp\left(-\frac{2\ln 2\delta^2}{\tau^2}\right)$  and  $\mathbf{Q} = \mathbf{k}_{in} - \mathbf{k}_s$  is the momentum transfer. The above equation is considered as the key equation for TRXD. Let us assume  $|E_i - \langle \mathcal{H}_0 \rangle_t| \ll 1/\tau$  holds, where  $E_i$  is eigen-energy corresponding to  $i^{\text{th}}$  eigenstate of the wavepacket, and  $\langle \mathcal{H}_0 \rangle_t$  is the mean energy of the wavepacket. After performing the  $\delta$ -integral, the expression of the DSP for a short x-ray pulse reduces as (Dixit et al., 2014)

$$\begin{aligned} \frac{dP}{d\Omega} &= \frac{dP_e}{d\Omega} \int_0^{\infty} d\omega_{\mathbf{k}_s} \frac{\omega_{\mathbf{k}_s}}{\omega_{\mathbf{k}_{in}}} \sum_f \frac{\tau_l}{\sqrt{8\pi \ln 2}} e^{-(\tau_l^2/8 \ln 2)(\omega_{\mathbf{k}_{in}} - \omega_{\mathbf{k}_s} + \tilde{E} - E_f)^2} \\ &\times \int d\mathbf{r} \int d\mathbf{r}' \langle \Psi(\mathbf{r}, T) | \hat{\rho}(\mathbf{r}') | \Phi_f \rangle \langle \Phi_f | \hat{\rho}(\mathbf{r}) | \Psi(\mathbf{r}, T) \rangle \times e^{-i\mathbf{Q} \cdot (\mathbf{r} - \mathbf{r}')}. \end{aligned}$$

Here,  $\frac{dP_e}{d\Omega} = \frac{d\sigma_{\text{th}}}{d\Omega} \int_{-\infty}^{\infty} d\gamma \frac{I(\mathbf{r}_0, \gamma)}{\omega_{\mathbf{k}_{in}}}$  is the DSP for a free electron and  $\mathbf{T}$  is the pump-probe time delay. For a small energy-transfer within the bandwidth of the x-ray pulse during the diffraction,  $\omega_{\mathbf{k}_s}$  can be approximated as  $\omega_{\mathbf{k}_{in}}$ . Within this assumption, the final expression of DSP can be simplified as

$$\frac{dP}{d\Omega} = \frac{dP_e}{d\Omega} \sum_f \left| \int d\mathbf{r} \langle \Phi_f | \hat{\rho}(\mathbf{r}) | \Psi(\mathbf{T}) \rangle e^{-i\mathbf{Q} \cdot \mathbf{r}} \right|^2. \quad (2.3.8)$$

Here, the summation over  $f$  includes all zeroth-order states included in the dynamics, which amounts to detect all the scattered photons within a given solid angle, irrespective of the mean photon energy. In this thesis, we have used the above expression for DSP to simulate the time-resolved diffraction signals for different molecular systems.

Refs. (Kowalewski et al., 2017; Simmermacher et al., 2019b) discussed different roles of the time-independent and time-dependent diffraction signals to the total diffraction signal. Moreover, a detailed discussion about probing electronic coherences in the wavepacket have been documented in Refs. (Dixit et al., 2012; Simmermacher et al., 2019a). Furthermore, the time resolution in TRXD depends on several factors like temporal duration on x-ray pulse, jitter between pump and probe pulse, pump-probe time delay etc.

## 2.4 Technical Details

In this thesis, ultrafast laser-induced charge migration is simulated using the hybrid TDDFT/CI methodology (Klinkusch and Tremblay, 2016; Hermann and Tremblay, 2016). This combination of methods provides a good balance between accuracy and computational efficiency. A generic  $N$ -electron wavepacket,  $|\Psi(\mathbf{r}, t)\rangle$ , is represented at any given time  $t$  as a linear combination of the ground state Slater determinant and singly excited many-body excited states as given in Eq. (2.0.5).

In the hybrid TDDFT/CI method, all expansion coefficients  $\{D_{0,k}, D_{a,k}^r\}$  are obtained from LR-TDDFT. This step is performed using standard quantum chemistry programs. The information from the quantum chemistry package is post-processed using the open-source toolbox detCI@ORBKIT. The contributions of



the different Slater determinants extracted from the quantum chemistry programs are first pruned by removing all contributions below some numerical threshold (here chosen as 0.001), and then renormalized. In the basis of pseudo-CI eigenfunctions chosen for the propagation, the Hamiltonian is considered diagonal. The matrix elements of the dipole moment operator in Eq. (2.2.6) are computed by numerical integration. Finally, by using Eqs. (2.0.2), (2.2.6), and (2.0.5), the time-evolution of the coefficients  $C_k(t)$  in Eq. (2.0.5) is performed by direct numerical integration of Eq. (2.0.1) using a preconditioned adaptive step size Runge-Kutta algorithm (Tremblay and Carrington Jr, 2004).

Integrating the time-dependent many-electron wavepacket in Eq. (2.0.5) leads to the one-electron quantum continuity equation as given in Eq. (2.2.13). From the many-body wave function, the expectation value of the one-electron density operator yields the one-electron electronic density [see Eq. (2.2.10)]. The expectation value of the operator  $\hat{j}(\mathbf{r})$  in Eq. (2.2.12) yields the flux density. The molecular orbitals to compute the integrals are expressed as linear combinations of atom-centered Gaussian functions, and all integrals are computed analytically. The electronic charge and flux densities thus obtained satisfy very accurately the continuity equation, Eq. (2.2.13). Details on the computation of the one-electron integrals from the many-body wave function using the detCI@ORBKIT toolbox are given in Refs. (Hermann et al., 2016b; Pohl et al., 2017; Hermann et al., 2017b).

It is assumed that the the probe x-ray pulse duration is much shorter than the timescale of the induced charge migration. Thus, TRXD signal is simulated using the expression for DSP as given in Eq. (2.3.8) (Dixit et al., 2014). The signal probes the coherences between eigenstates of the unperturbed Hamiltonian,  $|\Phi_k\rangle$ , contained in an electronic wavepacket.

All many-electron dynamical simulations are performed using in-house codes (Tremblay et al., 2011; Tremblay and Carrington Jr, 2004; Tremblay et al., 2008; Tremblay and Saalfrank, 2008; Tremblay et al., 2008). The integrals required to compute the TRXD signals and electronic flux densities are calculated using ORBKIT (OKg). Mayavi (Ramachandran and Varoquaux, 2011) and Matplotlib (Hunter, 2007) are used to visualize the electronic flux densities and the time-

resolved x-ray signals, respectively.

## Chapter 3

# Charge Migration in Heterocyclic Five-Membered Planner Molecules

Recent developments in laser technologies facilitate to generate intense ultrashort laser pulses. The availability of such laser pulses allows us to study ultrafast processes in molecules on their natural timescale. During laser-molecule interaction, electrons are the first to respond the action of an ultrashort laser pulse. As a result of this interaction, an electronic wavepacket is created, which sets an electronic charge distribution into motion. The migration of electronic charge around the atoms of the molecular scaffold affects the outcomes of chemical reactions and biological functions (Cederbaum and Zobeley, 1999; Kuleff et al., 2005; Breidbach and Cederbaum, 2003; Remacle and Levine, 2006; Breidbach and Cederbaum, 2005; Nisoli et al., 2017; Bredtmann et al., 2014). Thus, inducing and controlling the charge migration in molecules have emerged as one of the cornerstone topics of attosecond science in recent years (Folorunso et al., 2021; Kraus et al., 2015; Calegari et al., 2014; He et al., 2022).

Charge migration of valence electrons and corresponding electronic flux density (EFD) in ring-shaped molecules have received ample attention in recent years. Attosecond charge migration in magnesium porphyrin has been studied by means of EFD (Nam et al., 2020; Tremblay et al., 2021; Barth and Manz, 2006; Barth et al., 2006; Köksal and Koç, 2017). Moreover, multidirectional angular EFD

has been investigated by selective excitation in benzene (Hermann et al., 2016a; Jia et al., 2017; Hermann et al., 2017a, 2020). At this juncture, it is natural to envisage how the nature of the charge migration will alter by transiting from six-membered benzene to five-membered ring-shaped molecules. This is the main aim of this chapter. For this purpose, pyrrole, furan and oxazole, which are five-membered neutral ring-shaped aromatic molecules, will serve our purpose. These three heterocyclic aromatic molecules are present in many important biological systems as a fundamental unit and have enormous applications (Domingos et al., 2021). Series of detailed calculations for electronic properties of pyrrole, furan and oxazole have been performed (Christiansen et al., 1999; Roos et al., 2002; Lee and Boo, 1996; Serrano-Andres et al., 1993; Wan et al., 2000; Burel et al., 2002; Palmer et al., 1995; Christiansen and Jørgensen, 1998). Also, few non-equilibrium dynamics in three molecules have been documented in Refs. (Cao et al., 2016; Geng et al., 2020; Carrascosa et al., 2021; Barbatti et al., 2010, 2006; Yong et al., 2021).

This chapter provides a detailed and comparative study of adiabatic attosecond charge migration of valence electrons in pyrrole, furan and oxazole. In the following, we will discuss how the charge migration is sensitive to the symmetry reduction, i.e., progressing from benzene with  $\mathcal{D}_{6h}$  symmetry to these five-membered ring-shaped molecules with  $\mathcal{C}_{2v}$  and  $\mathcal{C}_s$  symmetries. Furthermore, we will investigate how the nature of electronic charge and flux densities during charge migration is altered by the presence of foreign atoms, i.e., nitrogen in pyrrole, oxygen in furan; and nitrogen and oxygen in oxazole.

In this chapter, to achieve the convergence of the laser-induced charge migration simulations,  $N_{\text{states}} = 24, 22$ , and 32 lowest-lying bound excited states are used for pyrrole, furan and oxazole, respectively. The CAM-B3LYP functional and aug-cc-pVQZ basis sets on all atoms are used to compute these electronic states (Yanai et al., 2004; Dunning Jr, 1989). All electronic structure calculations are preformed with the Gaussian16 program (Frisch et al., 2016).

## 3.1 Results and Discussion

To compare the charge migration in pyrrole, furan, and oxazole on equal footing, a few conditions are considered. The first one is a static consideration, where the target excited states are chosen to have a similar character. In particular, the selected states must contain a strong signature of the lower symmetry in oxazole, and the effect of the electronegativity of the foreign atoms must be readily observable. This can be achieved by exciting states that create nodal structure around the foreign atoms. Further, in order to populate a target excited state, it must be optically accessible. That is, the intensity of the transition from the ground to target excited state (proportional to the transition dipole moment  $\mu^2$ ) must be high. From a dynamical perspective, charge migration should be faster than the timescale of nuclear rearrangement, ideally in the sub-femtosecond regime, yet accessible with a few-femtosecond laser pulse. The target excited states satisfying both constraints will thus have similar energies and transition dipoles. Further, understanding the dynamics of the electronic density and EFD after such a pump pulse is greatly simplified if the wavepacket is composed of only a few components in the excited state manifold. This is achieved by exciting only a small fraction of electronic populations and optimizing the laser parameters (field intensity and carrier frequency), thereby leading to a controlled degree of charge migration.

The charge distribution corresponding to the ground electronic state of the three molecules is presented in Fig. 3.1(a). All three molecules are projected in the  $yz$  plane throughout this chapter. Pyrrole and furan are symmetric with respect to reflection about the  $z$  axis that bisects molecule through the foreign atoms and the opposing CC bond, and the ground state densities both transform according to the totally symmetric point irreducible representation (IRREP) of the  $C_{2v}$  point group. The presence of the nitrogen atom (blue) appears to favour delocalization of the electrons over the whole ring in the  $\pi$ -orbitals. The more strongly electronegative oxygen atom (red) leads to a more compact ground state density in furan (central panel), which is more concentrated at the foreign atom. Due to the presence of both oxygen and nitrogen atoms on the two sides of the pentagon, oxazole is not

symmetric with respect to a reflection in the plane and retains only the operations of the  $C_s$  point group.

To identify interesting target state in each molecule, the natural transition orbitals (NTOs) of all states up to the ionisation threshold have been inspected. The NTOs of the lowest excited state accessible via a linearly polarised field along the

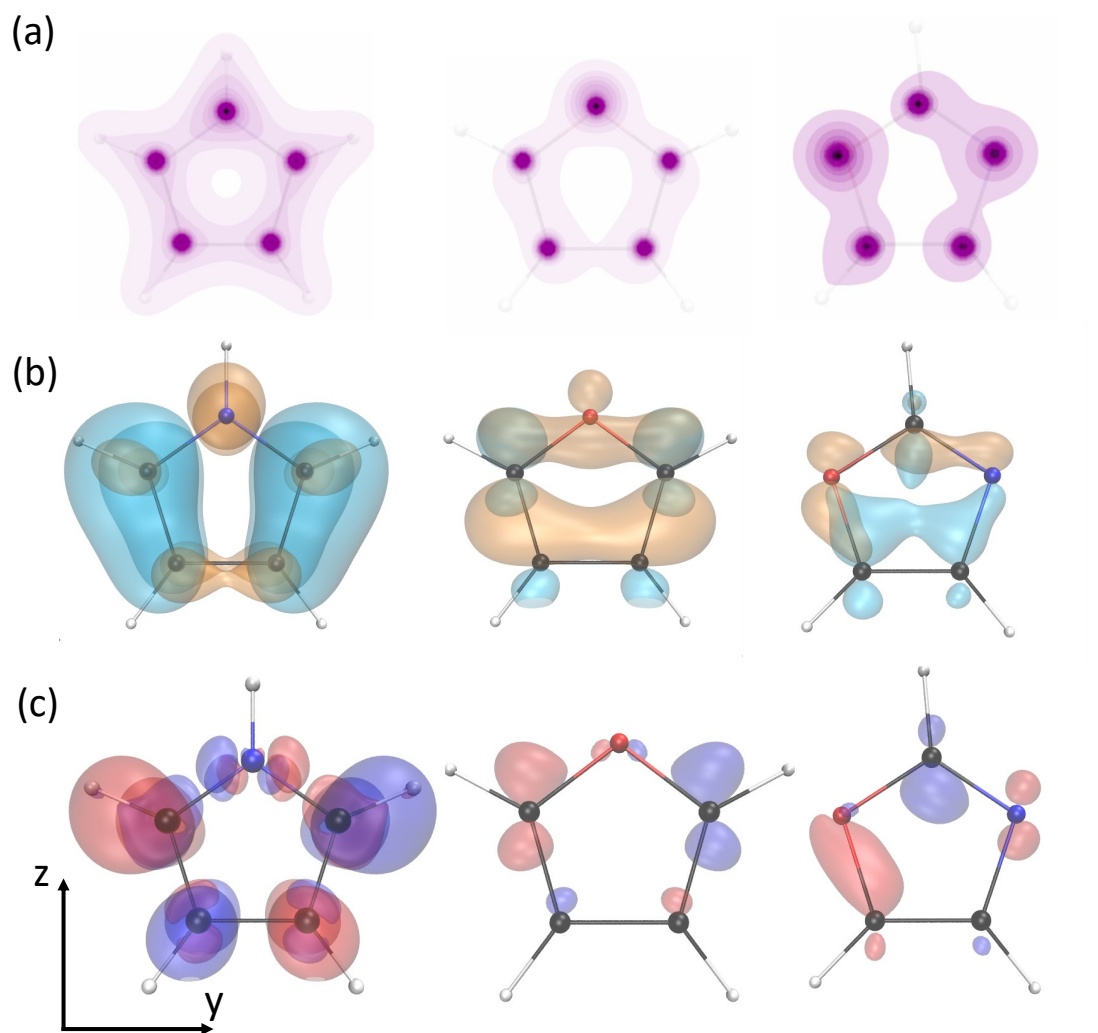


Figure 3.1: Depiction of the electronic structure in the five-membered ring molecules. Pyrrole, furan, and oxazole are represented from left to right. (a) Ground state electron density (isocontours equally separated by 0.001 a.u.). (b) Natural transition orbitals. Orange and blue surfaces represent the particle and hole densities, respectively. (c) Difference electron densities between target excited and ground electronic states,  $\rho_m(\mathbf{r}) - \rho_0(\mathbf{r})$ . Red (blue) colour represents regions of density depletion (increase). The isosurface values are  $\pm 0.005$ ,  $\pm 0.02$ , and  $\pm 0.03$  for pyrrole, furan, and oxazole, respectively for both NTOs and transition densities.

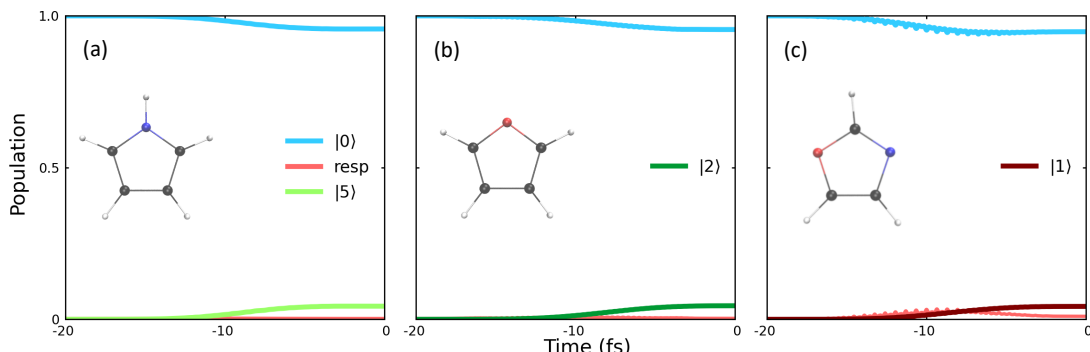


Figure 3.2: Laser-induced population dynamics in heterocyclic five-membered ring molecules triggered by 20 fs sine-squared linearly polarized pulse along  $y$  axis. The label “resp” indicates the residual population of all other electronic states, which acts as a non-linear response during the excitation. The three molecules are shown in ball-and-stick representation, which are projected in the  $yz$  plane throughout in this work. White, grey, blue and red colours represent hydrogen, carbon, nitrogen and oxygen, respectively. (a) Pyrrole: carrier frequency resonant with the energy of the 5<sup>th</sup> electronic state (6.26 eV); peak intensity of  $3.7 \times 10^{13}$  W/cm<sup>2</sup>. (b) Furan: carrier frequency resonant with the energy of the 2<sup>nd</sup> electronic state (6.26 eV); peak intensity of  $2.8 \times 10^{13}$  W/cm<sup>2</sup>. (c) Oxazole: carrier frequency resonant with the energy of the 1<sup>st</sup> electronic state (6.37 eV); peak intensity of  $7 \times 10^{13}$  W/cm<sup>2</sup>.

$y$  axis are shown in Fig. 3.1(b). These correspond to the fifth, second and first excited states in pyrrole, furan, and oxazole, respectively. The transition intensities of these target excited states are much higher than the transition intensities from the ground to all other excited states of the respective molecule. NTOs offer a compact depiction of electronic transitions from a reference state in terms of particle and hole densities (Martin, 2003). In all three molecules, the excitation indeed creates nodal structure around the foreign atoms but the excitation characters are radically different. The hole density (blue) in pyrrole is found to be delocalized on both sides of the ring on the carbon atoms, with a clear  $\pi$  character and a node along the  $y$  axis. The particle density (orange) is more strongly localized close to the atoms of the ring, with a  $\pi$  character around the nitrogen atom. The structure is very different in furan, where the hole density is localized around the carbon atoms and exhibits a stronger in-plane bonding character (reminiscent of a  $\sigma$  character, in opposition to an out-of-plane  $\pi$ -character). The same character is found in the particle density, which is delocalized along the C-O-C fragment, as well as through space between the two C=C bonds. Both excitations in pyrrole and furan

retain the structure of the  $C_{2v}$  point group. The NTO densities in oxazole are more similar to the furan case, although it is the hole density that has the through-space structure.

The difference densities between the ground and target states are also shown in Fig. 3.1(c). The strong  $\pi$ -type characters, i.e., the out-of-plane bonding characters of the excitation in pyrrole is noticed. In opposition to  $\pi$  character, a clear nodal structure in the plane of the molecule analogous to the  $\sigma$  character of the excitations in furan and oxazole can be readily recognized. More importantly, the difference densities reveal the symmetry of the excited states, which are found to transform according to the  $B_2$  IRREP of the  $C_{2v}$  point group for pyrrole and furan. These important differences should lead to markedly different charge migration dynamics after laser excitation.

Keeping in mind the dynamical requirements described above, we have employed a linearly polarized pulse along the  $y$  direction to induce the charge migration. The resultant population dynamics is presented in Fig. 3.2. The pulses for three molecules have comparable peak intensities, with similar carrier frequencies tuned at the respective target transitions. The peak intensities of the pulses, in excess of  $10^{13}\text{W}/\text{cm}^2$ , are tuned to obtain similar population in the target states, hence leading to a similar contrast in the charge migration patterns. As evident from the figure, the target excited states reach around 4% population in all three cases. The values of the transition dipole ( $\mu^2$ ) to the target excited states are  $0.9898\text{ }ea_0$ ,  $1.1071\text{ }ea_0$ , and  $1.0048\text{ }ea_0$  for pyrrole (fifth), furan (second), and oxygen (first), respectively. This compares favourably to all other transitions with values lower than  $0.25\text{ }ea_0$  in all three molecules.

The population in all off-resonant electronic states are termed as “resp” in the figure, as they mediate the non-linear response of the electron density to the strong external laser pulse. Electronic response is found to be more important in oxazole than in either pyrrole or furan. During the pulse, the population of these non-resonant states is exactly zero for pyrrole and furan, but non-zero in oxazole. This is because of the strong transition dipole moments to other excited states in oxazole, which stems from its different chemical nature compared to the other two



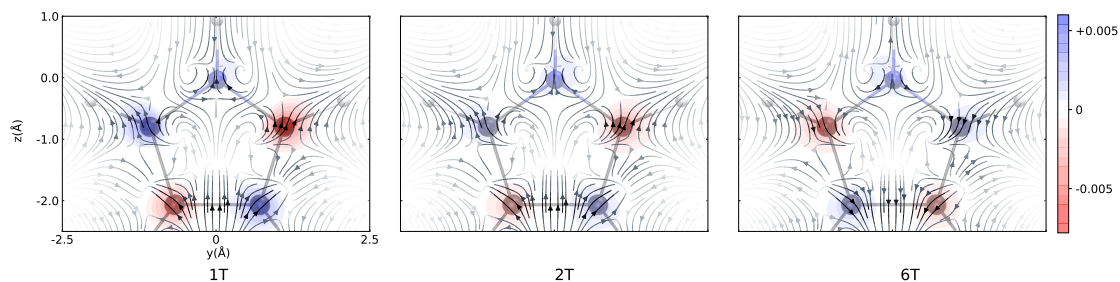


Figure 3.3: Time-dependent difference electron and associated flux densities during charge migration in pyrrole at  $1T$ ,  $2T$  and  $6T$ . Here,  $T = \tau/8$  with  $\tau = 660$  attoseconds as the characteristic timescale of the charge migration in pyrrole. Ground-state electron density is subtracted in the time-dependent difference electron density at each subsequent time step. The colour of the stream-line arrows varies from white to black according to their increasing intensity. The red and blue contours present the depletion and the enhancement of the difference electronic density with respect to the ground state density. For better visualisation, the projection of pyrrole in the  $yz$  plane is superposed in ball-stick representation.

molecules. The field-free charge migration sets into motion at time zero, after the pulse. Since the target excited states in the three systems have similar excitation energies with respect to the ground electronic state, the charge migration will have a similar oscillation period around 650 as.

To shed light on the effect of symmetry and electronegativity on field-free charge migration on its characteristic timescale, we analyze snapshots of the time-dependent difference electron density and the associated EFD. For the former, the contribution from the electronic ground state is subtracted from the wavepacket at each time step.

Figure 3.3 presents the the difference density and the EFD at three time steps for pyrrole. The overall behaviour of the difference densities at all times reflects that they are mostly located around the atoms, which indicates charge localization. This corresponds well to the picture offered by the density difference in the left panel of Fig. 3.1(c). The strong charge localisation around the atoms should not affect strongly the bonding properties in pyrrole. Consequently, it is unlikely that the excitation chosen would lead to any bond breaking, ring-opening or other photochemical reaction. Moreover, the difference densities are positive and negative in alternate carbon atoms, whereas nitrogen is always surrounded by the positive

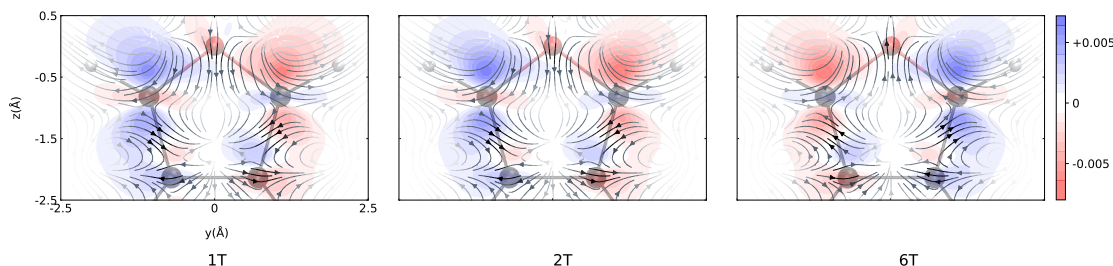


Figure 3.4: Same as Fig. 3.3 for furan with  $\tau = 660$  attoseconds as the characteristic timescale.

electron density. At 1T and 2T, the positive contour around nitrogen is tilted towards the positive  $y$  axis as evident from the figure. This situation is reversed at 6T. The difference densities around carbon atoms are anti-symmetric about  $y$  axis at all time. The overall intensity of the difference density reduces from 1T to 2T. There is a phase shift of  $\pi/2$  from 2T to 6T, which is in accordance with the half time-period of the charge migration as evident from the figure. The characteristic timescale for the charge migration in pyrrole is  $\tau = 660$  attoseconds.

The electron flow can be understood better in terms of the EFD. As evident from Fig. 3.3, the direction of the electron flow is mostly around the atoms. The streamlines start from the atomic positions and terminate around the bonds at all times. This reflects the atom-to-bond charge migration in pyrrole, which corresponds well to the picture offered by the NTO in Fig. 3.1(b). Indeed, the particle density is observed to be strongly localized around the atoms. Consequently, the streamlines appear as piecewise disjoint lines of flow around each atom. From a symmetry point of view, there is no general electron flow from left to right or from upward to downward. At 1T, the flow around the bottom two carbon atoms is upward inside and downward outside of the pyrrole ring. Similar to the difference densities, the streamlines follow the same phase reversal from 2T to 6T. The EFD transforms according to the the totally symmetric IRREP of the  $\mathcal{C}_{2v}$  point group at all times.

At this juncture it is natural to ask how the above findings will alter if one replaces nitrogen by a more electronegative atom, say oxygen. To explore the question further, let us analyze the difference density and the EFD for furan at

three time steps as presented in Fig. 3.4. The electronic ground state density and the NTO of the target transition in Fig. 3.1 already indicate a significant change in the charge migration dynamics. Unlike for pyrrole, the positive and negative contours of the difference electron densities are distributed not only around the atoms but also around the bonds, and the latter is higher in intensity. They are anti-symmetric about the  $y$  axis except around the oxygen atom. These findings are in agreement with the density difference profile observed in Fig. 3.1(c).

The bond strengthening (weakening) shown by this increase (decrease) in the electronic densities around the bonds is primarily visible on the two sides of the oxygen atom. In contrast to pyrrole, these will affect the bond strength and potentially cause bonds to break, resulting in ring opening on either side of the foreign atom. Exciting furan with short, intense laser pulses of the form used in this work is therefore more likely to trigger photochemical processes on longer timescales. Interestingly, the difference density around the oxygen is negative at all times, reflecting the larger electronegativity of oxygen compared to the carbon atoms of the ring. Since the oxygen substitution preserves all operations of the  $C_{2v}$  point group, the density difference upon charge migration in furan retains the same  $B_2$  IRREP as for pyrrole.

From the EFD for furan displayed in Fig. 3.4, a swirling type of motion between the atoms of the ring is evident. The streamlines show a flow downward through the bonds between the oxygen and its nearest carbon atoms, and going upward to the hydrogen atoms at time steps 1T and 2T. The direction of the flow is completely reversed at 6T. These patterns are consistent with the NTO picture in Fig. 3.1(b), which show a stronger in-plane bonding character and more nodal structure in the plane of the molecule for the target excitation. Despite the apparent complexity of the flow patterns, they transform according to the the totally symmetric IRREP of the  $C_{2v}$  point group at all times. It can be concluded that the stronger in-plane bonding character of the target excitation in a ring bearing a more electronegative atom does not affect the symmetry of the charge migration.

For the charge migration in pyrrole and furan, both molecules belong to  $C_{2v}$  point group. The symmetry of the five-membered ring can be reduced by substitu-

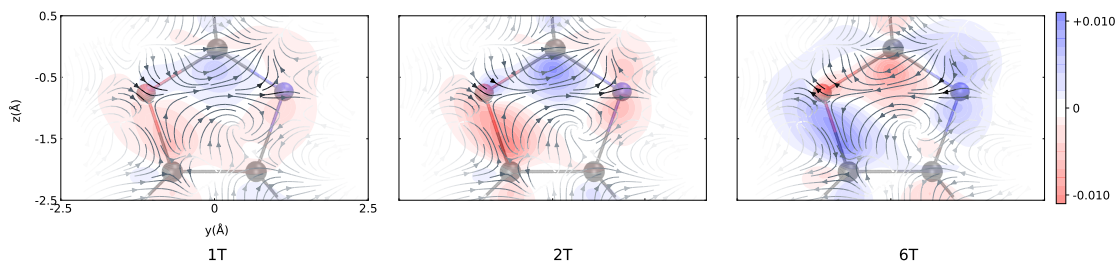


Figure 3.5: Same as Fig. 3.3 for oxazole with  $\tau = 650$  attoseconds as the characteristic timescale.

tion of two carbon atoms by both nitrogen and oxygen. To understand this further symmetry reduction, let us explore the charge migration in oxazole, which has  $C_s$  symmetry.

As a result of the symmetry reduction, the charge migration in oxazole changes drastically as two carbon atoms are replaced by one nitrogen and one oxygen atoms on the opposite sides of the pentagon ring (see Fig. 3.5). Due to the presence of the different atoms in the ring, the difference electron densities are entirely different in comparison to pyrrole and furan, and do not exhibit any symmetric behaviour upon rotation with respect to the  $z$  axis or reflection in the  $xz$  plane. The regions of the density increase/depletion are not specific to the bonds or atoms. The dumbbell structure observed at all time step in the difference electron density around nitrogen atom hints at a strong contribution of a  $p$ -type orbital in the molecular plane. At 1T, the negative contours are present around the bonds and positive contours are situated in the space between nitrogen, oxygen and carbon atoms. In general, there is no strong correlation between the difference density plots during charge migration and the ones reported in Fig. 3.1(c).

To have a better understanding of the charge migration mechanism in oxazole, let us analyze the time-resolved EFD after laser excitation, as depicted in Fig. 3.5. The multiple directions of the flux densities provide a picture of the charge migration that is consistent with the NTO densities depicted in Fig. 3.1(b). A swirling motion is observed, separated in bottom and top contributions that barely exchange electrons at all times. This is intriguing, since the excitation using a  $y$  polarized pulse would likely create nodal structure along this direction. As such,

a left-right separation of the charge migration should be expected, as was the case for pyrrole and furan. From the NTOs in Fig. 3.1(b), it appears that the top part of the particle density only migrates towards the hole density located between the two foreign atoms. We attribute this feature to their electronegativity, that prefer to retain the excited electron localized in this fragment. On the other hand, the bottom part of the charge migration sees a transfer of the particle localized on the CO bond to the CC bond across the ring. This part of the charge migration operates through space rather than following the bonds, in stark contrast with the more symmetrical pyrrole and furan. The bonds connecting to the oxygen atom experience the strongest bond strength oscillations, whereas bonds connected to the nitrogen atom see less pronounced fluctuations. Much like the case of furan, it can be inferred from the electronic density and EFD snapshots that oxazole could probably undergo further photochemical reactions.

## 3.2 Summary

In summary, we have investigated the role of symmetry reduction and of electronegativity on adiabatic attosecond charge migration in selected heterocyclic five-membered aromatic ring molecules. Time-dependent transition electron and flux densities were used to unravel the mechanism of charge migration induced by selective laser pulses. To compare the charge migration on three molecules on equal footing, transition with similar energetics were used to reach target excited states with high transition intensities and nodal structure close to the foreign atoms. It has been found that laser-induced charge migration and the corresponding EFD are significantly different in the three molecules in spite of these constraints. Moreover, variations in electronic densities and EFDs reveal bond strengthening or weakening upon excitation by light, which is useful to infer photochemical potential in these molecules. For the laser pulses used in this chapter, it was inferred that pyrrole is less likely to undergo ring-opening reactions than furan and oxazole.

The presence of the nitrogen in pyrrole and oxygen in furan make the charge migration in both molecules significantly different. In pyrrole, a signature of charge localization is observed during charge migration as the difference electron densities

are positioned around the atoms. In contrast, electron density depletion/increase upon light-induced charge migration in pyrrole are delocalized around the atoms and around the bonds, which indicate bond-to-atom charge transfer in furan. The charge migration patterns observed in both cases are totally symmetric. For oxazole, the difference electron densities documenting the charge migration dynamics display no symmetry outside of the  $yz$  plane as a result of the lower symmetry, from  $C_{2v}$  in furan and pyrrole to  $C_s$ . In this case, charge migration takes the form of a swirling motion through space.

We believe that our results on attosecond charge migration in heterocyclic five-membered rings will motivate further theoretical investigations in other types of molecular systems, where studies of structure-migration relationships are still few and far apart. Further, state-of-the-art emerging experimental techniques, such as attosecond transient-absorption spectroscopy (Kraus et al., 2015; Calegari et al., 2014), high-harmonic generation spectroscopy (Folorunso et al., 2021; He et al., 2022; Dixit et al., 2018; Chandra et al., 2019), or time-resolved x-ray diffraction (Dixit et al., 2012, 2014), to name but a few, will provide potent probes for our findings in heterocyclic five-membered ring molecules in coming future.

## Chapter 4

# Role of Structural Saddling on Charge Migration

Technological advancements in recent years have allowed us to control the synthesis of different types of corroles with interesting coordination chemistry. The properties of the central metal in metal-corroles are always the focus of ample attention. Due to the intriguing coordination chemistry and its compatibility with a variety of transition metals (Nardis et al., 2019), metal-corroles have demonstrated potential for applications as photosensitizers (Jiang et al., 2019; Mahammed and Gross, 2019) and catalysts (Dogutan et al., 2011; Gross et al., 2000; Mahammed et al., 2003), to name but a few. Copper corrole is one of the first systems bearing a transition metal in which copper was experimentally inserted in the  $N_4$  coordination core of the corrole ring. Unlike other metal-corrole complexes, copper corrole is found to have a saddling in its equilibrium structure (see Fig. 4.1), which makes this molecule very interesting for different applications (Ghosh et al., 2000; Luobeznova et al., 2004; Bröring et al., 2007; Pierloot et al., 2010). A combined study of x-ray absorption spectroscopy and TDDFT have been performed to understand the electronic structure of copper corrole (Lim et al., 2019). Moreover, the role of the saddling on the electronic structure properties of low-lying electronic states in copper corrole was explored by analysing the results of planar and saddled geometries (Pierloot et al., 2010). Furthermore, static x-ray diffraction with

density functional analysis confirmed the saddling feature of copper corroles (Alemayehu et al., 2009; Bröring et al., 2007). Several theoretical works have been carried out to understand the saddling in copper corroles (Ghosh et al., 2000; Luobeznova et al., 2004; Alemayehu et al., 2009; Lim et al., 2019).

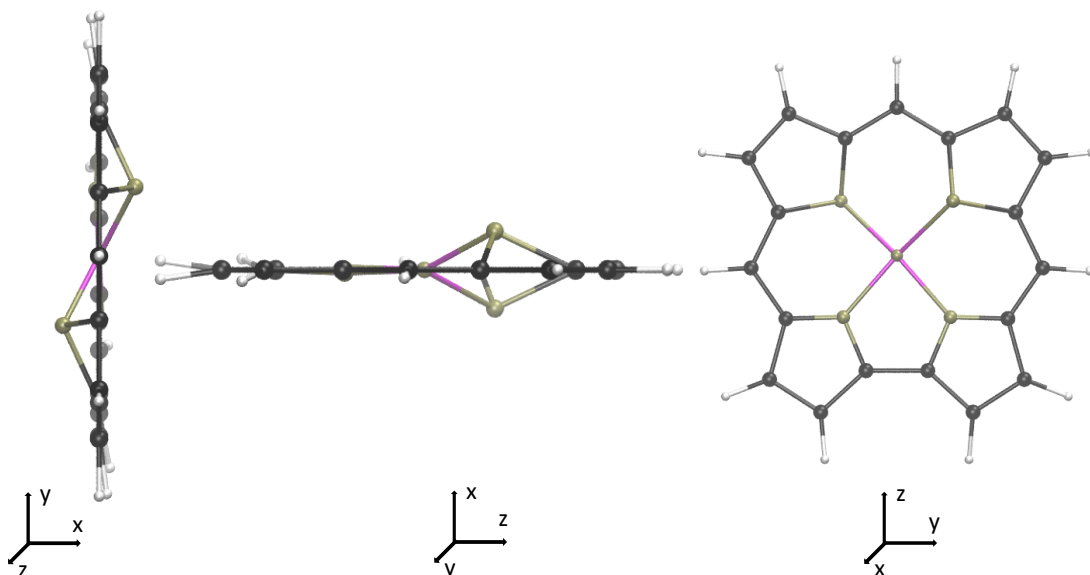


Figure 4.1: Ball-stick representation of unsubstituted copper corrole in different orientations, with the molecule in the  $yz$  plane. Magenta, tan, black, and white spheres represent copper, nitrogen, carbon, and hydrogen atoms, respectively.

*A priori*, it is not obvious how the saddling in a molecular structure will affect the charge migration on attosecond timescale, during which the effect of nuclear vibrations is insignificant. Moreover, what would be the signature of the structural saddling in any experimental probe signal, if any? The main aim of this chapter is to investigate such crucial questions. In this chapter, we discuss time-resolved imaging of charge migration in an unsubstituted copper corrole within a pump-probe configuration. An ultrashort pump pulse induces charge migration in copper corrole, which is imaged by TRXD at various pump-probe delay times. Additionally, we will analyse time-dependent EFDs to understand the mechanistic details of the charge migration associated with the induced dynamics. The time-dependent EFDs provide an additional information about the direction of the electron flow during charge migration in copper corrole.

In this chapter,  $N_{\text{states}} = 80$  lowest-lying excited states below the ionization



threshold are used to achieve the convergence of the excitation dynamics induced by the pump pulse in copper corrole. The states are computed using the CAM-B3LYP functional (Yanai et al., 2004) and aug-cc-pVDZ basis sets (Dunning Jr, 1989) on all atoms, as implemented in Gaussian16 (Frisch et al., 2016).

## 4.1 Results and Discussion

The molecular structure of the unsubstituted copper corrole in ball-stick representation is shown in Fig. 4.1. All axes and coordinates are described in the molecular frame of reference, and it is assumed that the molecule is oriented in the  $yz$  plane of the laboratory frame. From the projections in the two other planes, the saddling in copper corrole is evident, which makes this particular type of corrole appealing for detailed investigations.

To trigger the charge migration, a 10 fs cosine-squared linearly polarized pulse along the  $y$  axis is employed. The wavelength and the peak intensity of the pump pulse are chosen to 360 nm and  $3.5 \times 10^{13}$  W/cm<sup>2</sup>, respectively. It has been experimentally demonstrated that a coherent transfer of population from ground to excited states is possible with such intensity in molecular systems (Prokhorenko et al., 2005). The resulting population dynamics of the electronic states during the pump pulse is presented in Fig. 4.2.

Transfer of population from the electronic ground state to other excited states starts as the pump pulse interacts and the electron dynamics in copper corrole sets into motion. As evident from Fig. 4.2, only a small amount of population around 9.4% is transferred to the ninth electronic excited state, and most of the population remains in the ground state, i.e., 89% at the end of the pulse. Small population transfer from the ground to excited states is common in various excitation schemes during experiments (Liu et al., 2018; Glowacki et al., 2016), as it can be achieved in a more controlled manner with lower field intensities. The rest of the electronic populations, termed as “resp” in Fig. 4.2, is distributed among other excited states with insignificant probability. The insignificant contributions from other states involved in the electronic response during the excitation can be neglected for further analysis. The energy difference between the ground and the ninth excited states

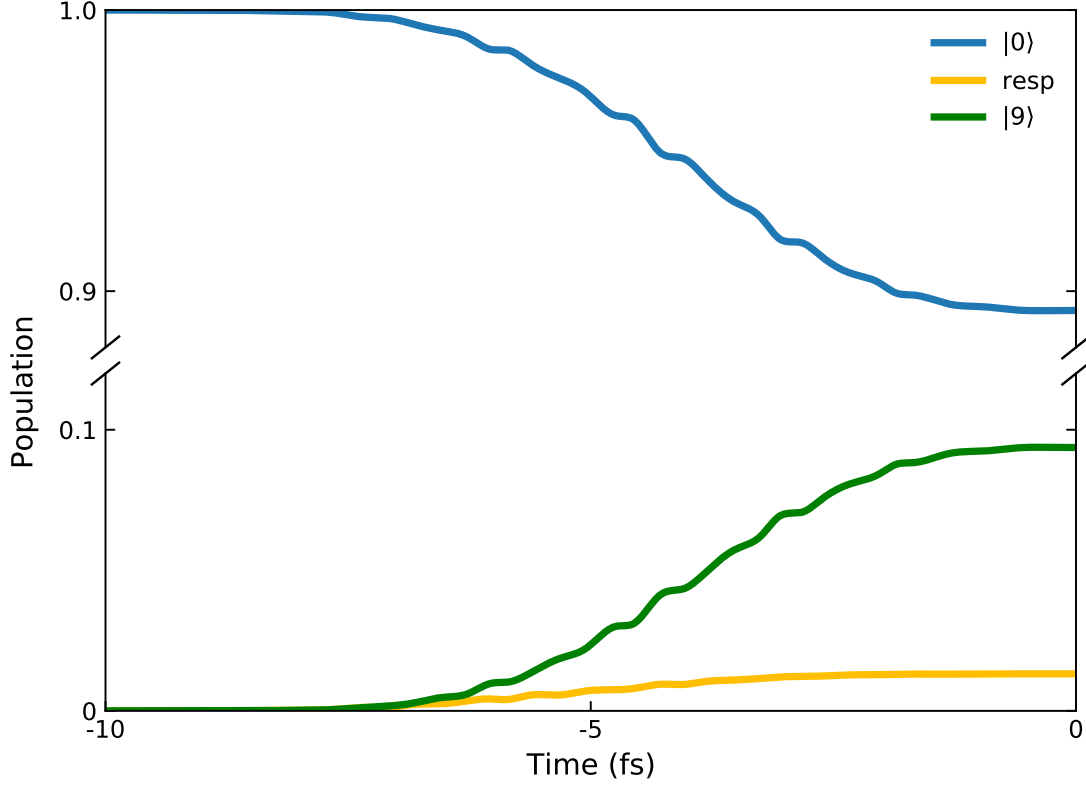


Figure 4.2: Population dynamics of selected electronic states of copper corrole.  $|0\rangle$  represents the ground electronic state, and  $|9\rangle$  represents the target electronic state with energy  $E_9 = 3.45$  eV. The orange line labeled “resp” represents the electronic response in the presence of the field, leading to the residual population of the rest of the electronic states after the excitation. A cosine-squared linearly polarized pulse of 360 nm wavelength with peak intensities of  $3.5 \times 10^{13}$  W/cm<sup>2</sup> is used to induce the population dynamics. The pulse is 10 fs short and polarized along the  $y$  axis. Time zero defines the onset of field-free electron dynamics.

is  $\Delta E = 3.45$  eV. Focusing only on the dominantly populated state allows us to estimate a characteristic timescale for the electron dynamics as  $\tau = \hbar/\Delta E = 1.2$  fs. Time zero in Fig. 4.2 represents the onset of field-free charge migration, i.e., after the pump pulse ended.

After triggering the charge migration by a short, intense pump pulse, we employ TRXD in a pump-probe configuration to probe the dynamics using a probe pulse much shorter than  $T = 30$  as. Figure 4.3 presents time-resolved diffraction signals at different pump-probe time delays during the field-free charge migration dynamics. As the saddling is present in both the  $zx$  and  $xy$  planes, while the

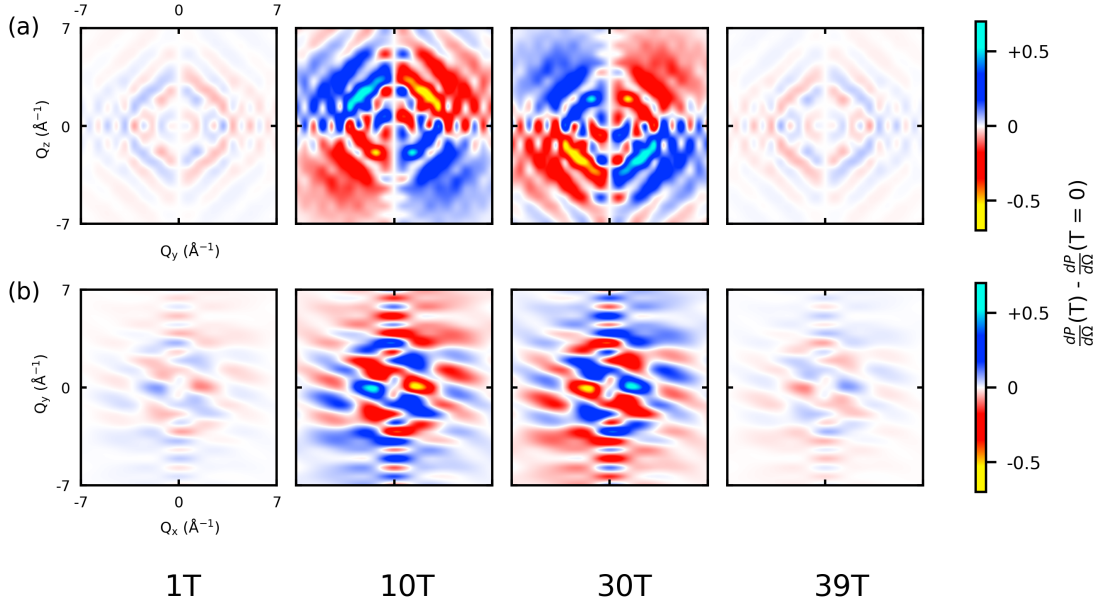


Figure 4.3: Time-resolved difference diffraction signals for copper corrole in (a)  $Q_y - Q_z$  and (b)  $Q_x - Q_y$  planes at different pump-probe delay times during field-free charge migration. Here,  $T = \tau/40$  is chosen with  $\tau = 1.2$  fs as the characteristic timescale of the charge migration. The intensity of the diffraction patterns is presented in units of  $dP_e/d\Omega$ . The time-independent diffraction signal at zero delay time is subtracted at all subsequent delay times.

molecule lies in the  $yz$  plane without any saddling (see Fig. 4.1), the diffraction signals are presented in  $Q_y - Q_z$  and  $Q_x - Q_y$  planes, which are used to emphasize the role of saddling during the charge migration. For representation purpose, the total signal at the zero pump-probe delay time is subtracted from the total signals at different subsequent delay times. Ground and the 10 lowest-lying excited states are used to simulate the TRXD signal, i.e.,  $f = [0, 10]$  in Eq. (2.3.8).

At a glance, it seems that the overall intensity variation of the diffraction signals in the  $Q_y - Q_z$  [Fig. 4.3(a)] and  $Q_x - Q_y$  [Fig. 4.3(b)] planes is approximately the same at all delay times, up to the phase and the signal magnitude. The global maxima and smaller local features migrate up and down in the  $Q_y - Q_z$  plane. In the upper panels, the signal is found to be antisymmetric with respect to reflection about the  $Q_y = 0$  line. At the beginning of the charge migration, i.e., at delay time  $T$ , the signal also exhibits reflection symmetry with respect to the  $Q_z = 0$  line around low  $\mathbf{Q}$  region. This feature in the signal is also true around the characteristic timescale  $\tau = 1.2$  fs =  $40T$ , which is clearly visible from the signal at  $39T$  [the last

figure of Fig. 4.3(a)]. Note that the total signal, which is not the difference signal, is strictly anti-symmetric at  $\tau = 0$  and  $40T$ , and the snapshots at  $T$  and  $39T$  are chosen at the onset of symmetry reduction. This scenario changes significantly at the two intermediate delay times,  $10T$  and  $30T$ . The intensity of the signal exhibits an extremum close to the center, with local maxima at around values of  $\pm 1$  in  $Q_y$  and  $Q_z$ . The extremum is initially more intense and diffused in the upper half of the plane, i.e., at positive values along the  $Q_z$  axis at delay time  $10T$ . The symmetry reduction can be understood using a simplified model of the charge migration as a superposition of  $|0\rangle$  and  $|9\rangle$  electronic states. As derived from Eq. (2.3.8) [also see SI of Ref. (Hermann et al., 2020)], the time-dependent part of the TRXD signal in such superposition state reads

$$\frac{dP(T)}{d\Omega} \propto \cos(\omega_{09}T) \operatorname{Re}[\mathcal{L}_{09}(\mathbf{Q})] - \sin(\omega_{09}T) \operatorname{Im}[\mathcal{L}_{09}(\mathbf{Q})], \quad (4.1.1)$$

where  $\omega_{09} = (E_9 - E_0)/\hbar$  is the transition frequency between the  $|0\rangle$  and  $|9\rangle$  states, and

$$\mathcal{L}_{09}(\mathbf{Q}) = \sum_f \left[ \int d\mathbf{r} \int d\mathbf{r}' \langle \Phi_0 | \hat{\rho}(\mathbf{r}) | \Phi_f \rangle \langle \Phi_f | \hat{\rho}(\mathbf{r}') | \Phi_9 \rangle e^{i\mathbf{Q} \cdot (\mathbf{r} - \mathbf{r}')} \right]. \quad (4.1.2)$$

As evident from the middle column of Fig. 4.4, the real and imaginary parts of  $\mathcal{L}_{09}(\mathbf{Q})$  in the  $Q_y - Q_z$  plane have different symmetry under reflection over the  $Q_z$  axis. Thus, symmetry reduction occurs by oscillation between these two  $\operatorname{Re}[\mathcal{L}_{09}(\mathbf{Q})]$  and  $\operatorname{Im}[\mathcal{L}_{09}(\mathbf{Q})]$  terms.

Let us analyse the signal at  $30T$ , which deserves a separate discussion. Signal depletion is observed in the  $Q_z = Q_y$  direction at both delay times as documented in the top panels of Fig. 4.3. In real space, this direction includes the nitrogen atom that buckles *above* the molecular ( $yz$ ) plane. Regions of signal enhancements (in blue and cyan) are found along the  $Q_z = -Q_y$  direction, coinciding with the  $z = -y$  direction, which contains the nitrogen atom buckling *below* the molecular ( $yz$ ) plane. Left-right reflection about the  $y = 0$  line is the only symmetry element remaining in the projection of the molecule in the  $yz$  plane, which gives rise to the

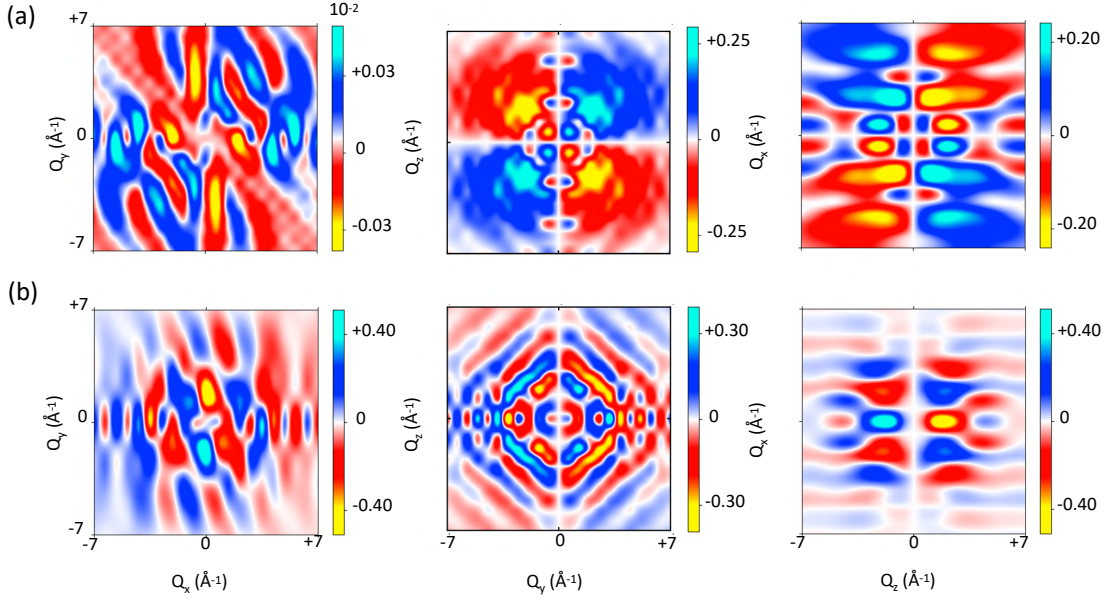


Figure 4.4: (a) Real and (b) imaginary part of  $\mathcal{L}_{90}(\mathbf{Q})$  in the  $Q_x - Q_y$ ,  $Q_y - Q_z$ , and  $Q_z - Q_x$  planes, respectively (from left to right).

pattern observed in the TRXD signal. Hence, interference effects due to electronic coherences lead to the symmetry reduction of the TRXD signal. The asymmetry of the maxima with respect to the  $Q_z = 0$  line observed at both delay times, 10T and 30T, correlates in both cases with signal depletion for the nitrogen above the corrole plane or with signal enhancement for the nitrogen below the plane.

The signal in the  $Q_y - Q_z$  plane at the beginning and end of the characteristic timescale transforms according to the  $B_1$  irreducible representation (IRREP) of the  $\mathcal{C}_{2v}$  point group. However, at other delay times, the signal transforms according to the  $A''$  IRREP of the  $\mathcal{C}_s$  point group [see the second and third figures of Fig. 4.3(a)]. Incidentally, this is also the point group of the molecule projected in the  $yz$  plane; see right panel of Fig. 4.1. Let us understand this symmetry alteration by analysing the time-dependent difference density during field-free charge migration, as shown in Fig. 4.5. As reflected from the top panels, the difference density in the  $yz$  plane is found to transform according to the  $A''$  IRREP of the  $\mathcal{C}_s$  point group. This IRREP belongs to the point group of the plane projection of the molecule. Also, it is known that the Fourier transform of a transition density belonging to the  $\mathcal{C}_s$  point group corresponds to the  $\mathcal{C}_{2v}$  point group (Defranceschi and Berthier, 1990).

The temporal evolution of the signals in the  $Q_x - Q_y$  plane for different delay

times is significantly different than the signals in the  $Q_y - Q_z$  plane [see Figs. 4.3(a) and 4.3(b)]. The presence of the twisted structures in the diffraction signals seems a signature of the saddled structure of copper corrole during charge migration. Both the TRXD signal [Fig. 4.3(b)] and the difference density [Fig. 4.5(b)] retain exactly the same structure at all times, albeit with phase reversal and intensity variations during the dynamics. Both the signal and the difference density transform according to the  $A_u$  IRREP of the  $C_i$  point group, to which belongs the projection of the molecule in the  $xy$  plane. It was shown that the Fourier transform of a transition density belonging to the  $C_i$  point group will belong to the same group (Defranceschi and Berthier, 1990).

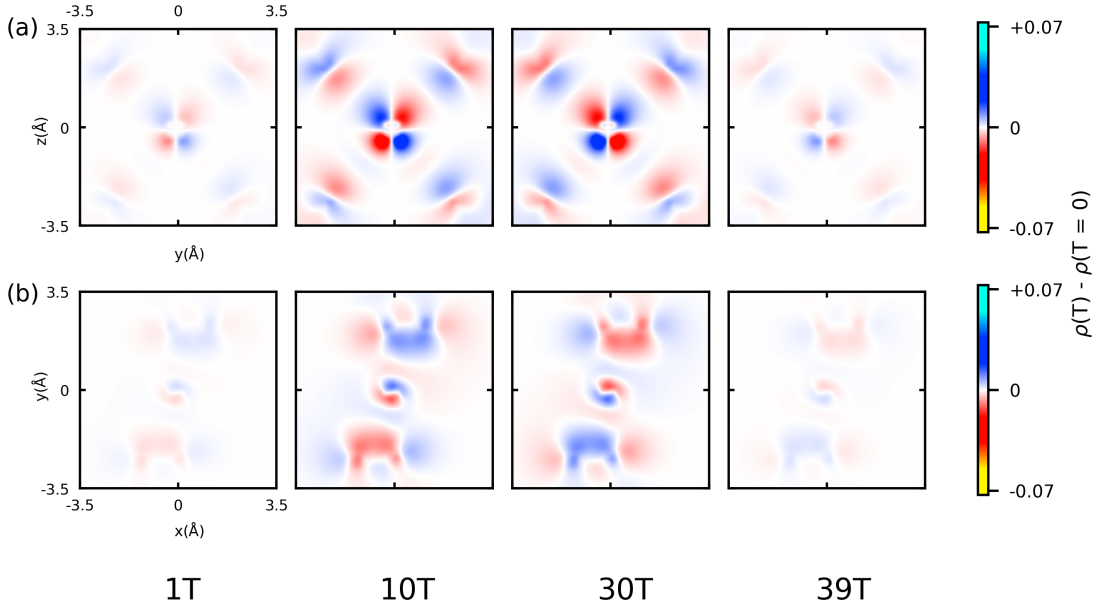


Figure 4.5: Time evolution of the electron density of the wavepacket during field-free charge migration in copper corrole. The electron density at zero time delay is subtracted at all subsequent delay times and the difference density is represented in the (a)  $yz$  and (b)  $xy$  planes. As in Fig. 4.3,  $T = \tau/40$  is chosen with  $\tau = 1.2$  fs as the characteristic timescale of the electron dynamics.

To better understand the connection between the results shown in Figs. 4.3 and 4.5, let us analyse the key expression for TRXD, which reveals that the difference diffraction signal encodes the Fourier transform of the transition electron density  $\int d\mathbf{r} \langle \Phi_f | \hat{\rho}(\mathbf{r}) | \Phi_k \rangle e^{-i\mathbf{Q} \cdot \mathbf{r}}$  [see Eq. (2.3.8)]. Also, the difference density of an electronic wavepacket consists of several terms of transition electron density, i.e.,

$\langle \Phi_f | \hat{\rho}(\mathbf{r}) | \Phi_k \rangle$ . Note that it is well established that the TRXD is simply not related to the Fourier transform of the instantaneous electron density of the wavepacket,  $\int d\mathbf{r} \langle \Psi(\mathbf{T}) | \hat{\rho}(\mathbf{r}) | \Psi(\mathbf{T}) \rangle e^{-i\mathbf{Q}\cdot\mathbf{r}}$ ; and electronic coherences and the transition electron density play crucial roles in TRXD (Dixit et al., 2012). From the top panels of Fig. 4.3, it is evident that the electronic coherences do not destroy the symmetry relations between the transition density and its Fourier transform at early and later delay times, but they induce symmetry reduction in the TRXD signal at intermediate delay times during the dynamics. This finding is specific to this particular example and the choice of exciting field is likely to affect the times at which symmetry reduction occurs due to interferences.

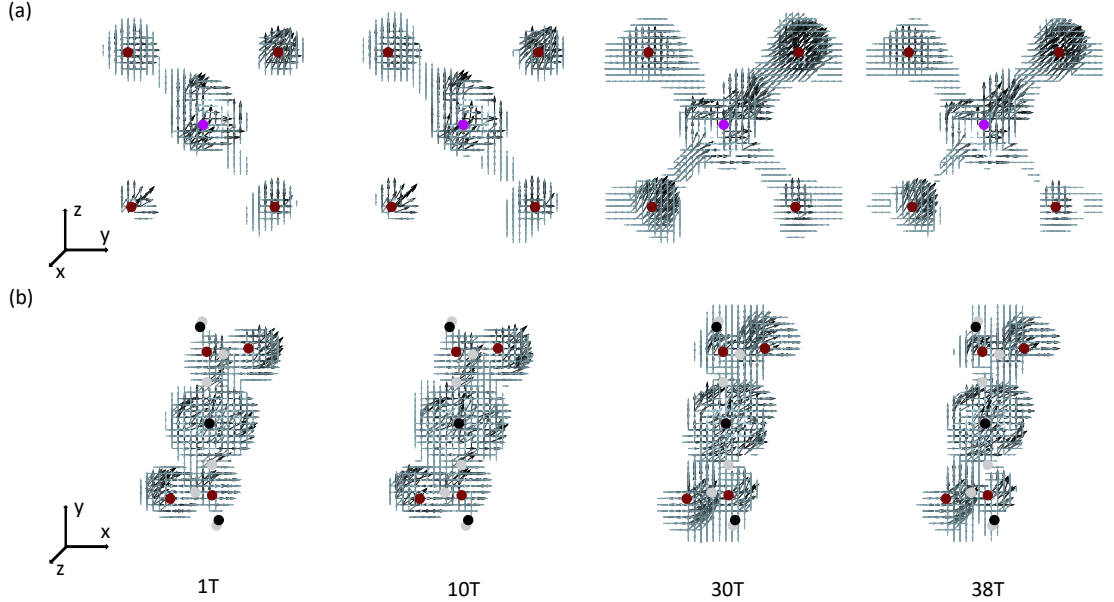


Figure 4.6: Time-dependent electronic flux densities for copper corrole in the (a)  $yz$  and, (b)  $xy$  planes at different pump-probe delay times during field-free charge migration. The laser excitation parameters are the same as in Fig. 4.2. The period  $T = \tau/40$  is chosen as the oscillation period  $\tau = 1.2$  fs of the electron dynamics. The black, violet, maroon, and gray dots represent carbon, copper, nitrogen, and hydrogen atoms, respectively.

Let us explore the charge migration in real space to complement the mechanistic picture of the charge migration, which could provide a deeper understanding of the time-resolved diffraction signal in detail. Knowledge of the dominant components of the electronic wavepacket allows one to analyse the charge migration at different instances in real space. Recently, it has been discussed that the analysis of the

transient EFD provides a detailed understanding of the electron dynamics as the flux density maps the direction of the electron flow in real space (Hermann et al., 2020; Tremblay et al., 2021).

Figure 4.6 presents the EFDs associated with the laser-induced charge migration at the same instances as in Fig. 4.3. The central part of the corrole ring containing the nitrogens and the copper is zoomed in to emphasize the dominant contribution to the flux densities. It is evident from Fig. 4.6(a) that the charge migration is taking place between the nitrogen atoms via the copper atom. Most of the charge seems to be displaced from the in-plane nitrogen in the bottom left to the nitrogen atom saddled above the surface in the top right, which corresponds to the  $Q_z = Q_y$  line in momentum space. As reflected from Fig. 4.3, the TRXD signals decrease along the  $Q_z = Q_y$  line, so we assign this migration pattern to a hole displacement during the dynamics. Synchronously, the nitrogen atom below the plane (top left) and the one in the bottom right appear to feed electrons to the copper atom, which corresponds well to the region of the TRXD signal increase along the  $Q_z = -Q_y$  line in the TRXD signal; see Fig. 4.3(a). The view of the flux densities in the  $xy$  plane provides complementary information. As evident from Fig. 4.6(b), out-of-plane nitrogen atoms are also connected to each other via the copper atom. This is revealed by the synchronous changes in the direction of the rotation of the flux densities around the nitrogen atoms. At T and 10T, the flux densities in the upper two nitrogen atoms rotate anti-clockwise, whereas they rotate clockwise for the bottom ones. This picture is reversed in the last two time steps at 30T and 39T.

Analysis of the EFDs in Fig. 4.6 also shows that the flux densities in the diagonal nitrogen atoms are different in magnitudes and directions. The present findings are in stark contrast with similar laser-induced charge migration dynamics in planar molecules, such as benzene and porphyrin in which the flux densities and the charge migration dynamics are observed to be symmetric at all times (Hermann et al., 2020; Barth and Manz, 2006; Barth et al., 2006). In this sense, the asymmetry in the EFDs appears to be a signature of the saddling in copper corrole during charge migration dynamics, which could be measured as a symmetry reduction



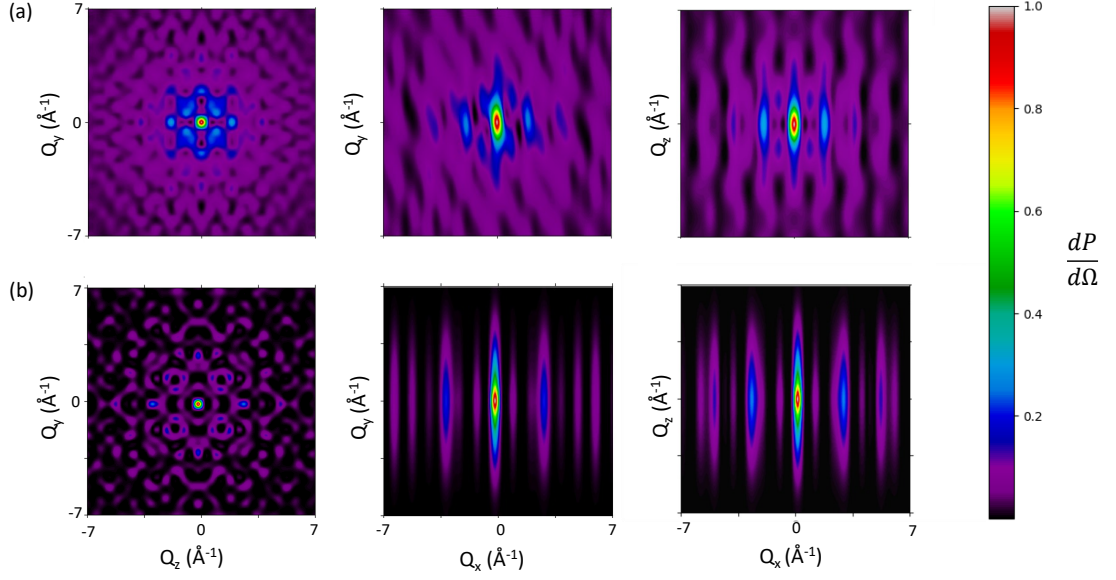


Figure 4.7: The static diffraction signals corresponding to the ground state for (a) copper corrole and (b) copper porphyrin in the  $Q_y - Q_z$ ,  $Q_y - Q_x$  and  $Q_z - Q_x$  planes (from left to right). The signals are normalized with respect to their maximum values.

in the time-resolved diffraction signals. Although the distortion of the molecular structure due to the saddling occurs in the  $xy$  plane, the signature of this symmetry reduction would rather be observed in the projection in the plane of the molecule, i.e., the  $yz$  plane. On the other hand, the connection between nitrogen atoms diametrically opposite of the copper atom is present in both the real-space and momentum-space views of the electron dynamics.

To further confirm our claim that the diagonal symmetry is related to the saddled structure of the copper corrole, we simulate the static diffraction signal of copper porphyrin in the ground state, which exhibits a non-saddled structure. For copper porphyrin in the ground state, the static diffraction signals are perfectly symmetric along the  $Q_x = 0$  and  $Q_y = 0$  planes. Moreover, owing to the non-saddled planar structure of copper porphyrin, the static diffraction signals in the  $Q_x - Q_y$  and  $Q_x - Q_z$  planes are identical, as reflected in Fig. 4.7(b). This is not the case for the signal of the saddled, nonplanar copper corrole shown in Fig. 4.7(a).

## 4.2 Summary

In summary, the present chapter discussed a first step towards understanding the interplay between ultrafast charge migration, structural deformation, and symmetry reduction in time-resolved x-ray imaging. We investigated laser-induced dynamics in copper corrole, which has an interesting saddled geometry with only slightly reduced symmetry. A linearly-polarized pump pulse is used to trigger electron dynamics, which is imaged by TRXD with atomic-scale spatiotemporal resolution. We find that the difference diffraction signals are sensitive to the saddled structure, and this asymmetry is reflected in the EFDs. For the studied excitation, the saddled nitrogen atoms in copper corrole are found to facilitate the coherent charge migration between nitrogen and copper atoms. We believe that our results on imaging electron dynamics in symmetry-reduced systems will motivate further theoretical and experimental research, in particular on light-induced ultrafast processes in various metal-corroles.

## Chapter 5

# Imaging Charge Migration in Chiral Molecules

Understanding the chirality is essential for a broad range of sciences including the origin of homochirality on earth. A molecule without inversion symmetry or a symmetry plane which is not superimposable with its own mirror image is known as a chiral molecule. A pair of such chiral molecules is known as an enantiomers. Enantiomers exhibit identical physical properties, but show a strong enantiomeric preference during chemical and biological reactions. Discerning the enantiomeric excess and handedness of chiral molecules is crucial in chemistry, biology, and pharmaceuticals.

Experimental methods based on chiral light-matter interaction, such as Coulomb-explosion imaging (Pitzer et al., 2013, 2016; Herwig et al., 2013), microwave spectroscopy (Patterson et al., 2013; Eibenberger et al., 2017), Raman optical activity (Barron et al., 1973; Barron, 2009) and laser-induced mass spectrometry (Bornschlegl et al., 2007; Li et al., 2006) have become practice to discern enantiomers in gas phase. Moreover, ionization based photoelectron circular dichroism approaches (Harding, 2005; Böwering et al., 2001; Nahon et al., 2006; Janssen and Powis, 2014; Ritchie, 1976; Powis, 2000) not only allow probing chirality in the multiphoton (Lux et al., 2012; Lehmann et al., 2013; Lux et al., 2015; Beaulieu et al., 2016a) and strong-field regimes (Dreissigacker and Lein, 2014; Beaulieu et al.,

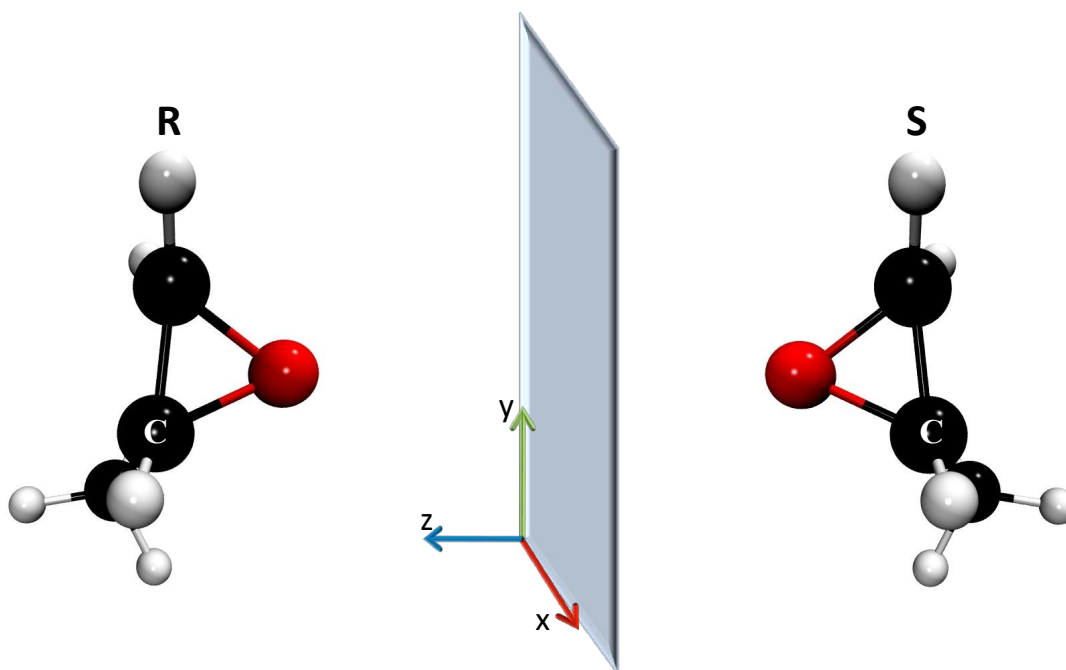


Figure 5.1: R- and S-enantiomers of epoxypropane in the molecular fixed frame. Gray, black and red spheres represent hydrogen, carbon and oxygen atoms, respectively. The chiral carbon is labelled by C. The  $xy$  plane is the mirror plane and the normal axis lies along the  $z$  direction.

2016b; Rozen et al., 2019), but also help us to understand molecular relaxation dynamics (Comby et al., 2016) and photoionization time delay (Beaulieu et al., 2017). Analogously, laser-induced photoelectron circular dichroism was recently used to obtain time-resolved chiral signal (Beaulieu et al., 2018; Harvey et al., 2018). In particular, Beaulieu et al. have employed time-resolved vibronic dynamics associated with a photoexcited electronic wavepacket to explain time-resolved chiral signal (Beaulieu et al., 2018). Recently, the signature of chirality is also probed by chiral high-harmonic generation (Cireasa et al., 2015; Smirnova et al., 2015; Wang et al., 2017; Harada et al., 2018; Baykusheva and Wörner, 2018; Neufeld et al., 2019; Baykusheva et al., 2019). In most of the aforementioned methods, left- and right-circularly polarized light were used to probe chirality in gas phase for randomly orientated chiral molecules. An alternate method based on pairs of linearly polarized laser pulses with skewed mutual polarization was proposed recently (Yachmenev and Yurchenko, 2016).

Recently, it has been demonstrated experimentally and theoretically that chiral

---

molecules can be oriented in a specific direction (Tutunnikov et al., 2018, 2020). When a linearly polarized laser pulse along  $x$  direction is employed, the chiral molecules try to align themselves in such a way that the most polarizable axis in molecules will be along the  $x$  direction. There will be an equal probability of alignment along the  $\pm x$  direction and molecules can rotate freely in the perpendicular plane, i.e., a chiral molecule would lie along this alignment axis and rotate about it. Orientational averaging would imply that observed signals would present no signature of chirality. A time-delayed second laser pulse with skewed polarization, linearly polarized in the  $xy$  plane at  $45^\circ$  between both axes, induces a dipole in the molecule. It is given by  $d_i = \sum_j \alpha_{ij} E_j$ , where  $\alpha_{ij}$  is the polarizability component and  $E_j$  is the electric field component of the laser pulse. As a result of the induced dipole, a torque  $\vec{\tau} = \vec{d} \times \vec{E}$  is induced along the aligned molecular axis. The analysis of the components of the torque yields a nonzero value of the average of the time derivative of the torque along  $z$  direction. The torque inducing this new alignment is proportional to the off-diagonal elements of the polarizability tensor. For nonchiral molecules, the off-diagonal elements have the same sign, so all molecules will experience the same torque. For chiral molecules, the off-diagonal elements of the polarizability tensor have opposite signs for different enantiomers. This implies that enantiomers will experience a torque in opposite directions, leading to opposite orientations, related by reflection symmetry (see Fig. 5.1).

On the other hand, if a circularly polarized laser pulse is applied, the interaction with the chiral molecules will be different. For  $E = E_0[\cos(\omega t)\hat{x} + \sin(\omega t)\hat{y}]$ , the components of the induced torque will be  $\tau_x = -E_0^2[\alpha_{zx} \cos(\omega t) + \alpha_{zy} \sin(\omega t)] \sin(\omega t)$ ,  $\tau_y = E_0^2[\alpha_{zx} \cos(\omega t) + \alpha_{zy} \sin(\omega t)] \cos(\omega t)$ , and  $\tau_z = -E_0^2[\alpha_{xy} \sin(\omega t) + \alpha_{yx} \cos(\omega t)]$ . The average value of the  $z$  component yields zero as we analyse the above expressions. For the other components of the induced torque, even if the components are different for the enantiomers as the polarizability tensors change sign, there is no simple  $\pi$ -phase change relation for the enantiomers. Therefore, the interaction with a circularly polarized laser pulse can break the symmetry of the enantiomers, but unidirectional orientation cannot be achieved.

In this chapter, we explore charge migration in chiral molecules by studying

ultrafast charge migration induced by a linearly polarized intense laser pulse for a specific orientation of molecules. It is not immediately obvious whether the charge migration in a space-fixed excited enantiomer pair should remain same or not. The answer is encoded in the EFDs, which maps the direction of electron flow. The time-dependent behaviour of EFDs in chiral molecules out-of-equilibrium remains uncharted territory. This is one of the main focuses of the present chapter. As will be discussed below, the EFD can become markedly different in an enantiomer pair under specific laser-excitation conditions, which would lead to different experimental signals. To illustrate the role of time-resolved EFD in chiral molecules, epoxypropane (1,2-propylene oxide, see Fig. 5.1) is used as a chiral molecule. Epoxypropane has been used in chiral high-harmonic generation (Cireasa et al., 2015), as well as being observed in interstellar media (McGuire et al., 2016; Bergantini et al., 2018).

Four-dimensional imaging of pump-induced charge migration in epoxypropane is done by TRXD. In this chapter, we will establish that TRXD and EFD analysis provide complementary information about the charge migration in epoxypropane driven by linearly polarized light. Moreover, we demonstrate that TRXD within pump-probe configuration offers an alternative to probe the handedness of chiral molecules. Note that confirming the handedness of chiral molecules by determining their spatial arrangement is known as absolute configuration determination (McMorrow and Als-Nielsen, 2011; Bijvoet et al., 1951; Santoro et al., 2020). X-ray crystallography is the one of the most reliable methods to determine the absolute configuration (Flack and Bernardinelli, 1999).

In this chapter, all  $N_{\text{states}} = 31$  lowest-lying excited states below the ionization threshold are used to obtain convergence, checked by repeating the laser-driven dynamics simulations with  $N_{\text{states}} = \{16, 21, 26, 31\}$ . The states are computed using the CAM-B3LYP functional (Yanai et al., 2004) and aug-cc-pVTZ basis sets (Dunning Jr, 1989) on all atoms, as implemented in Gaussian16 (Frisch et al., 2016).

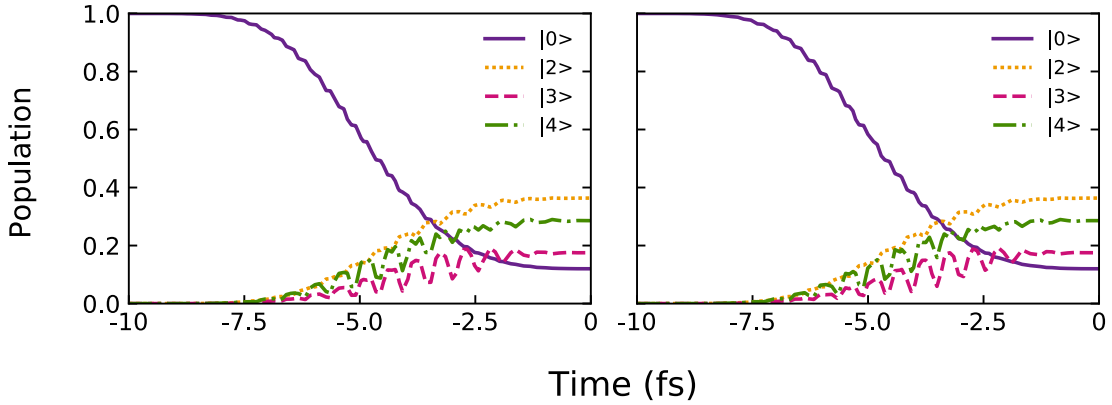


Figure 5.2: Population dynamics of selected electronic states for (a) R- and (b) S-epoxypropane. A sine-squared (carrier frequency: 7.67 eV; duration: 10 fs; peak intensity:  $10.1 \times 10^{14}$  W/cm<sup>2</sup>) linearly polarized pulse along the  $x$  axis is used to excite the first optically accessible band in both enantiomers.  $|0\rangle$  represents the ground electronic state. Only the excited states at energies  $E_2 = 7.51$  eV,  $E_3 = 7.56$  eV, and  $E_4 = 7.73$  eV are significantly populated throughout the dynamics. The time origin,  $T = 0$ , defines the onset of field-free charge migration.

## 5.1 Results and Discussion

To reveal the charge migration of enantiomers in an external laser pulse, it suffices to drive the system out-of-equilibrium, which transfers some population from ground electronic to a few selected excited states. In Fig. 5.2, the time-evolution of the many-electron state populations in the two enantiomers of epoxypropane is shown for a 10 fs sine-squared linearly polarized pulse along the  $x$  axis, with a 162 nm wavelength (7.67 eV) and  $10.1 \times 10^{14}$  W/cm<sup>2</sup> peak intensity. As evident from the figure, the state populations are identical for both enantiomers at all times. The small oscillations in the population of individual electronic states are due to the permanent dipole moments of these states, which interact with the laser pulse. These oscillations do not affect the population transfer dynamics. At the end of the pulse, i.e., at  $T = 0$ , approximately 83% population is transferred from the initial ground electronic state to a coherent superposition of the 2<sup>nd</sup> ( $P_2 = 36\%$ ), 3<sup>rd</sup> ( $P_3 = 18\%$ ), and 4<sup>th</sup> ( $P_4 = 29\%$ ) excited states. The timescales associated with different charge migration processes can be estimated from the energy difference between the different populated states,  $\tau = h/\Delta E$ . Due to significant popula-

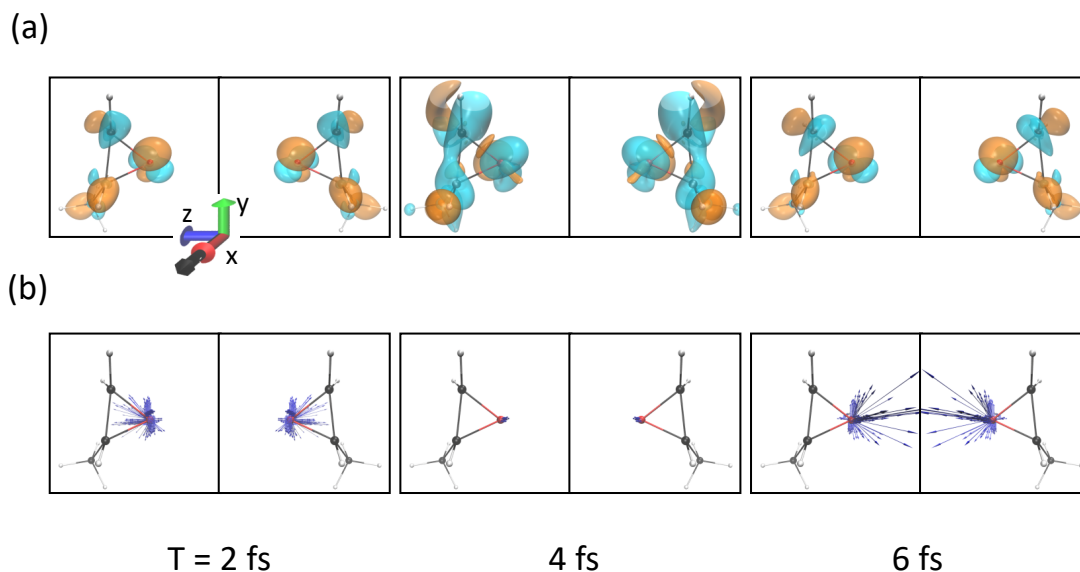


Figure 5.3: (a) Electronic charge distribution difference,  $\rho(\mathbf{r}, t) - \rho(\mathbf{r}, 0)$ , and (b) corresponding flux densities (blue arrows) for both R- and S-enantiomers during field-free charge migration, at different times after the onset of the field-free charge migration. The field parameters are defined in the caption of Fig. 5.2. Orange and blue colours represent isosurface values of -0.0015 and +0.0015, respectively.

tion in the ground electronic state after the pulse, the largest energy difference of  $\Delta E = 7.89$  eV leads to the fastest timescale for charge migration, within the attosecond regime (524 as). However, as most of the electronic population is transferred to the excited states, the dominant contribution to the charge migration will stem from interference effects among these three excited states. The timescale associated with these periodic processes range from 12.5 fs to 82.7 fs, and the charge migration is thus predominantly happening on the femtosecond timescale.

Although the populations are identical, it is not straightforward to infer whether the time-dependent charge distributions and associated EFDs [ $\mathbf{j}(\mathbf{r}, t)$  in Eq. (2.2.13)] corresponding to an electronic wavepacket are identical or not for both the enantiomers. Figure 5.3(a) presents the time-dependent charge distribution differences for both the enantiomers at three different times after laser excitation. The system is prepared using the pulse defined in Fig. 5.2 in a superposition state consisting majority of the ground state and of the 2<sup>nd</sup>, 3<sup>rd</sup> and 4<sup>th</sup> excited states. The charge distribution at the onset of field-free charge migration (i.e., at T = 0) is subtracted



from the charge distributions at later times to reveal the charge migration. At all times, the charge distribution differences for the enantiomers form mirror images, and the chirality of the enantiomer pair is preserved (see Fig. 5.3). The charge distribution at time  $T = 6$  fs is also found to be approximately similar to the distribution at  $T = 2$  fs. This is an indicative of a partial recurrence in the dynamics. Because the electronic wavepacket is a superposition of many electronic states with incommensurate energy differences, complete recurrence is not possible. Interestingly, the oscillations in the charge distribution do not appear to involve the chiral carbon atom (see also Fig. 5.1). This is due to the fact that all states excited by the chosen pulse do not involve strong reorganization of the electron density close to the chiral center. Prominent charge migration is taking place around the oxygen atom only. Negative isocontour values (orange), corresponding to electron depletion, are found at time  $T = 2$  fs and time  $T = 6$  fs, whereas they are changed to positive isocontour values (blue) at time  $T = 4$  fs. There is a small change of the isocontour for other carbon atoms except chiral carbon.

The variations of the one-electron density document charge migration but it is the EFD,  $\mathbf{j}(\mathbf{r}, t)$ , that yields spatially-resolved mechanistic information about the processes hidden within [see Eq. (2.2.13)]. These EFDs are shown as blue arrows in Fig. 5.3(b) for the same selected snapshots as above. At all times, most of the flux densities are localized around the oxygen atom. This confirms that the chiral carbon centre is not involved in this particular charge migration dynamics, since many-body excited states inducing a nodal structure at the chiral center are found at higher energies in epoxypropane. It is interesting to observe that the direction of the flux densities have opposite phases at  $T = 2$  fs and  $T = 6$  fs, although the magnitudes are almost equal. This picture contrasts with the one offered by the charge distribution differences at these two times, which are approximately similar in particular around the top carbon atom. This phase reversal in the flux densities describes a change in the flow direction of the electrons, and this information can not be obtained from the charge distribution dynamics. Approaching this partial recurrence in the charge migration process could lead to the observed sign reversal in the flow of electrons.

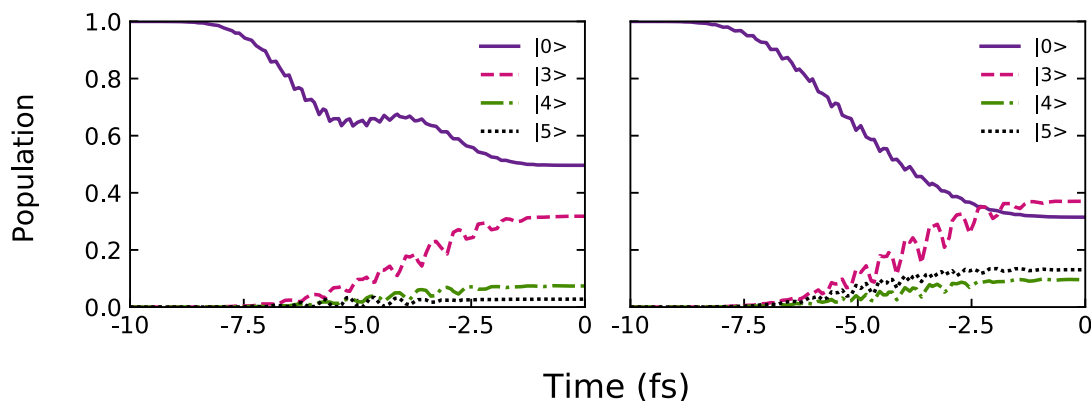


Figure 5.4: Population dynamics of selected electronic states for (a) R- and (b) S-epoxypropane. A sine-squared (carrier frequency: 7.75 eV; duration: 10 fs; peak intensity:  $9.1 \times 10^{14}$  W/cm<sup>2</sup>) linearly polarized pulse in the  $yz$  plane is used to excite the first optically accessible band in both enantiomers. Only the excited states at energies  $E_3 = 7.56$  eV,  $E_4 = 7.73$  eV, and  $E_5 = 7.84$  eV are significantly populated throughout the dynamics.

Note that the charge distributions and the EFDs, such as the ones depicted in Fig. 5.3, are related by the mirror reflection for both the enantiomers at all times. It is known that the mirror reflection of observables of one enantiomer along the mirror plane gives the same observable for other enantiomer due to the mirror symmetry of the chiral pair in the field. A sign change upon reflection is a fundamental measure of chirality and it is evident from Fig. 5.3. The general trends discussed above remain unchanged for any other field-free charge migration process in which the system is first prepared by laser pulses linearly polarized along the  $z$  axis,  $y$  axis, or for any laser polarization lying in the  $xy$  plane. In this case, the populations of electronic states will remain identical at all times for both the enantiomers, whereas the time-dependent charge distributions and EFDs will retain the mirror symmetry of the chiral pair. This naturally brings up the question, how these results will change when we use linearly polarized pulses along a plane including  $z$  axis.

Figure 5.4 shows the population dynamics for selected electronic states during a 10 fs sine-squared pulse of  $9.1 \times 10^{14}$  W/cm<sup>2</sup> peak intensity and 160 nm wavelength (7.75 eV). The electric field is linearly polarized at 45° between the axes in the  $yz$  plane. To achieve significant population among low-lying excited states, the

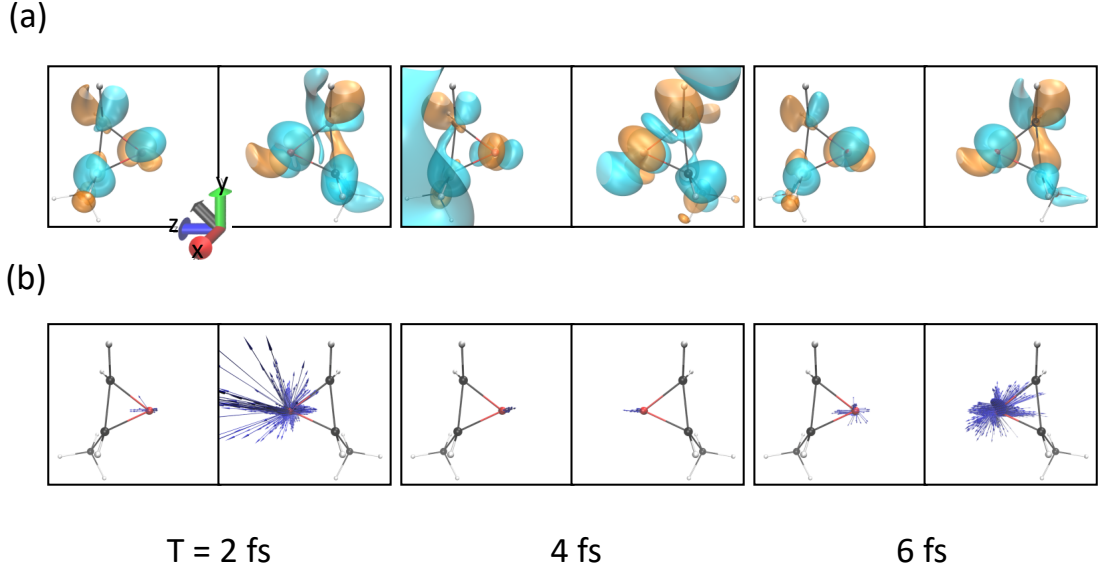


Figure 5.5: (a) Electronic charge distribution difference and (b) corresponding flux densities (blue arrows) for both R- and S-enantiomers during field-free charge migration, at different times after the laser pulse linearly polarized in the  $yz$  plane. The field parameters are defined in the caption of Fig. 5.4. Orange and blue colours represent isosurface values of  $-0.0015$  and  $+0.0015$ , respectively.

pulse parameters are tuned slightly compared to the previous case. As opposed to polarization along the axes, the population dynamics for both enantiomers differ drastically. For the R-enantiomer, 50% population remains in the ground state at the end of the pulse, whereas it is 70 % depleted for the S-enantiomer. The dominant state at the end of the pulse is found to be the 3<sup>rd</sup> one ( $P_3 = 32\%$  and  $37\%$  for R- and S-enantiomers, respectively). The latter enantiomer populates also more efficiently the 4<sup>th</sup> and 5<sup>th</sup> excited states ( $P_4 = 10\%$  and  $P_5 = 13\%$ , respectively), providing a more democratic population distribution than in the R-enantiomer ( $P_4 = 7\%$  and  $P_5 = 2\%$ ). It appears obvious that the field-free charge migration in the two enantiomers following such linearly polarized excitation in the  $yz$  plane will be radically different.

The charge distribution differences and EFDs for both the enantiomers are shown in Fig. 5.5. In this case, only contributions to the electronic wavepacket stemming from the 3<sup>rd</sup>, 4<sup>th</sup>, and 5<sup>th</sup> excited states are considered. Fast oscillating contributions from the ground state are removed. As could be inferred from the population at the pulse end, the charge migration dynamics differs drastically for

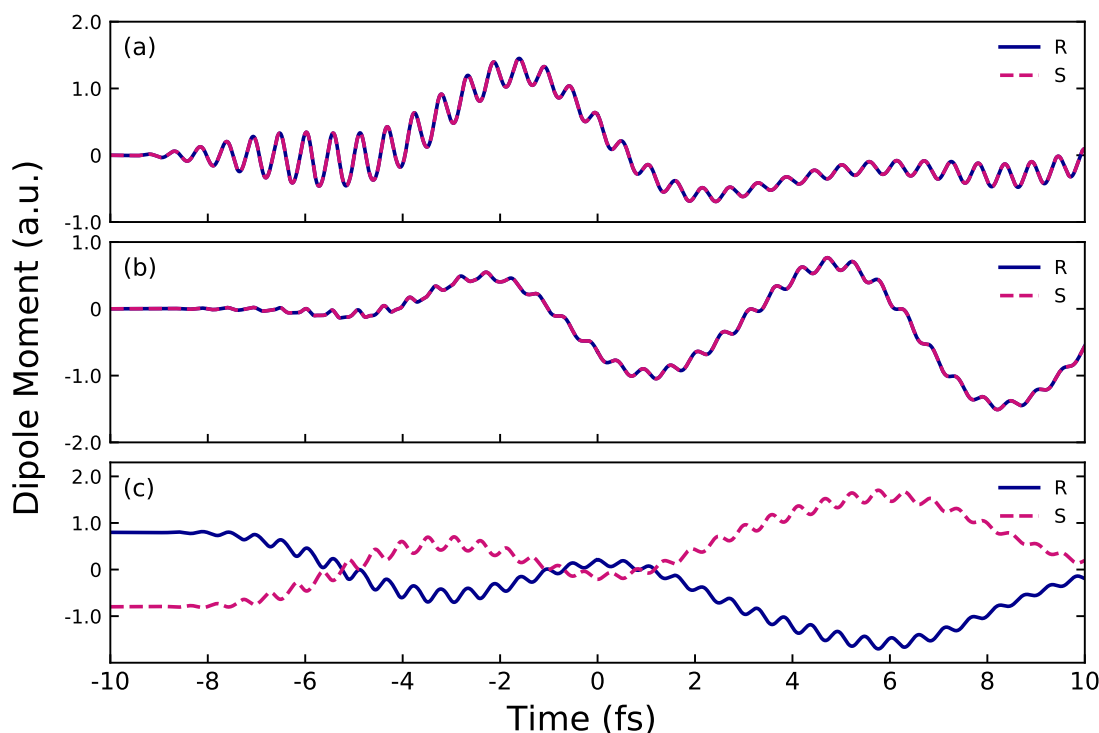


Figure 5.6: Time evolution of (a)  $x$ -, (b)  $y$ - and (c)  $z$ -components of the total dipole moment during and after excitation by a 10 fs sine-squared linearly polarized pulse along the  $x$  axis. The field parameters are the same as in Fig. 5.2.

the two enantiomers. Moreover, neither the charge distributions nor the EFDs are mirror images for both enantiomers, unlike in the case of excitation by linearly polarized pulses in the  $xy$  plane. Again, the EFDs are concentrated around the oxygen atom. This is confirmed by looking at the flux densities [blue arrows in Fig. 5.5(b)], which reveals that no electrons are flowing around nor through the chiral center. As in the previous excitation scenario, the charge distributions are similar for both the enantiomers at times  $T = 2$  fs and 6 fs, in particular around the oxygen atom (see Fig. 5.5). Although the relation to the evolution of the coherences in the system is as clear as above, the flux densities are also found to be in opposite directions in these two snapshots. Apart from the significant difference in the magnitude of the flux densities in the enantiomers, the nature of the evolution of the EFDs is also very different. At  $T = 2$  fs, the EFDs are equally distributed along  $z$  axis and  $x$  axis but at  $T = 4$  fs all of them are directed towards  $x$  axis and they are distributed along all the direction for the R-enantiomer at  $T = 6$  fs. In contrast, for the S-enantiomer, at  $T = 2$  fs and  $T = 6$  fs most of the EFDs

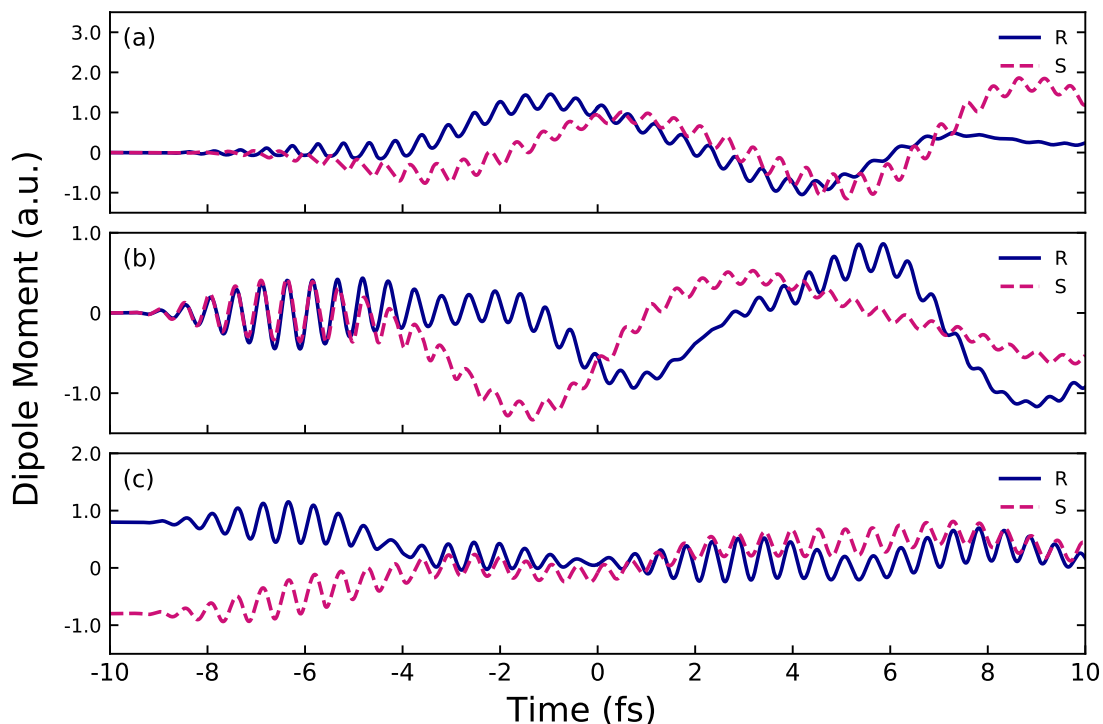


Figure 5.7: Time evolution of the cartesian components of the dipole moment along (a)  $x$ -, (b)  $y$ - and (c)  $z$ -directions. The amplitude and phase along all the axes are different for both the enantiomers. The field parameters are the same as in Fig. 5.4.

are distributed in the  $xy$  plane but they are directed towards the positive  $z$  axis at  $T = 2$  fs, whereas they are directed towards negative  $z$  axis in later time.

The previous simulations establish unequivocally that the field-free charge migration induced by linearly polarized pulse behaves differently for laser polarization along an axis or in the  $xy$  plane than for pulses polarized in a plane including the normal axis. This laser-induced charge migration process is documented by charge distribution differences and time-dependent EFDs, for a specific choice of molecular orientation. Importantly, these observations remain generally valid for any orientation of the molecule, as long as the molecule retains its orientation during the laser preparation phase.

These findings cannot be applied to aligned non-chiral molecules. For example, rotating the S-enantiomer by  $180^\circ$  about the  $y$  axis, the rotated S-enantiomer and R-enantiomer are not the same. Consequently, the population dynamics driven by a linearly polarized pulse carefully chosen according to the prescriptions described

below will be different. To explain the physical origin of the radically different flux densities in enantiomer pairs, induced by linearly polarized light, time-evolution of the dipole moment components for the enantiomers are calculated. The enantiomers show mirror symmetry perpendicular to the  $z$  axis in the absence of an external field (see Fig. 5.1). It is the presence or the absence of a mirror symmetry for the enantiomer pair in the field that determines the chirality of the charge migration, and this property is inherited by the subsequent field-free charge migration process.

The different Cartesian components of the total dipole moment are shown in Fig. 5.6 during excitation using a sine-squared linearly polarized pulse along the  $x$  axis and during subsequent field-free charge migration. The parameters of the pulse are chosen as in Fig. 5.2. It is evident from the figure that  $x$ - and  $y$ -components of the dipole moment are identical at all times for both the enantiomers. On the contrary, the evolution of the  $z$ -component is opposite in sign for the R- and S-enantiomers as the  $z$  axis is the chiral axis in this case (see Fig. 5.1). This mirror symmetry of the chiral pair can be seen by the opposite signs of the permanent dipole for the R- and S-enantiomers prior to the laser excitation, i.e., at  $T = -10$  fs. Upon excitation according to the first scenario, the pulse creates an electronic wavepacket, which follows the mirror symmetry of the enantiomer pair. The field generates a non-uniform time-dependent electronic distribution with different projections onto  $z$  axis. However, the electronic populations remain the same, as the orientation of the molecule relative to the  $xy$  plane is arbitrary. All linearly polarized pulses along any axis or in the  $xy$  plane will lead to a field-molecule interaction that preserves the mirror symmetry. Therefore, the  $x$ - and  $y$ -components of the time-evolving dipole moment will be identical for both enantiomers [see Figs. 5.5(a) and 5.5(b)]. However, the projection of the  $z$ -component along the normal axis will remain the same in magnitude but opposite in phase by reflection symmetry among the enantiomers. This statement is supported by our simulations, revealing an identical behaviour for the  $z$ -component of the dipole moment at all times for any initial molecular orientation [see Fig. 5.5(c) for a specific example]. Note that the  $\pi$ -phase variation in chiral molecules is a very widely known phenomenon, and

is also the mechanism for photoelectron circular dichroism, photoexcitation circular dichroism, microwave three wave mixing, nonlinear based chiral detection methods such as high-harmonic generation to detect chirality within the electric dipole approximation, etc. (Harding, 2005; Nahon et al., 2006; Powis, 2000; Yachmenev and Yurchenko, 2016; Leibscher et al., 2019; Beaulieu et al., 2018; Cireasa et al., 2015; Smirnova et al., 2015; Neufeld et al., 2019).

On the contrary, when the linear polarization of the pulse is rotated into a plane including the  $z$  axis and any of the two other axes, the time-evolution of all components of the dipole moment is different in magnitude and phase (see Fig. 5.7). For a pulse linearly polarized in the  $yz$  plane, the pulse interacts coherently with the components of the dipole along both these axes simultaneously, imposing a specific phase relation among them. The relation between the  $y$ -component of the dipole moment is the same for both enantiomers, while it is of opposite phase in the  $z$ -direction, therefore the torque experienced by the two enantiomers will be different. This creates a different coherent non-uniform distribution of excitations in the R- and S-enantiomers. The different populations induced by linearly polarized pulse lead to distinct charge migration patterns, which can be mapped by the evolution of the charge distributions and by the time-dependent EFDs.

### 5.1.1 Effect of imperfect orientation on electronic flux densities

Till now, we have discussed the EFDs in an oriented chiral molecule, i.e., with fixed spatial orientation. In general, most of the gas-phase methods deal with the ensembles of randomly oriented chiral molecules. Moreover, large and floppy chiral molecules are not easy to fix in the space. In the following, we consider the case where a chiral molecule is not fully fixed in the space and has some uncertainty in its orientation. For this purpose, we will introduce the notion of average EFD, which is incoherently averaged over different molecular orientations. To study the effect of orientation averaging on EFD for different orientations of the chiral molecule, the molecule is rotated by different angles. The absence of coherences implies an imperfect orientation in an ensemble of molecules, where each molecule

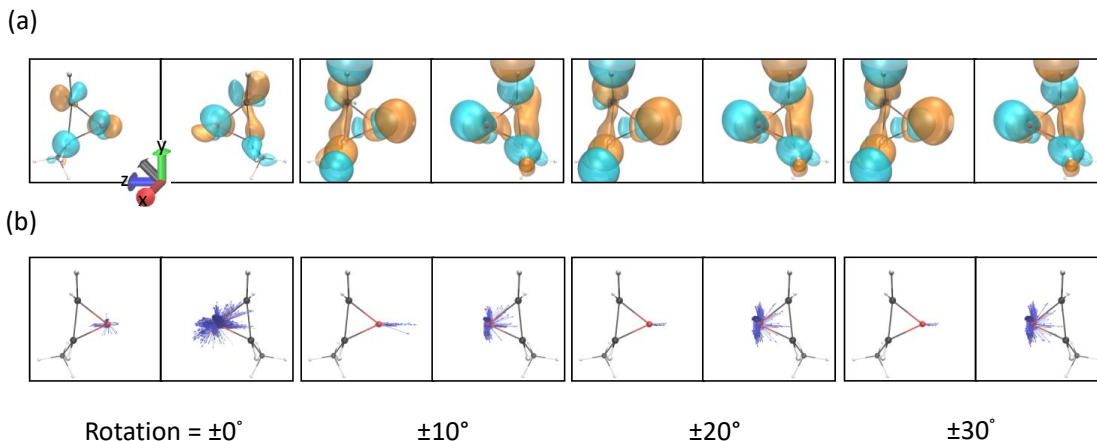


Figure 5.8: (a) Electronic charge distribution difference and (b) corresponding flux densities (blue arrows) for both R- and S-enantiomers at different rotation angles with respect to  $z$  axis, during field-free charge migration, at  $T = 6$  fs for linearly polarized laser pulse in  $yz$  plane. Isocontours at  $+0.0020$  (blue) and  $-0.0020$  (orange) for the enantiomers.

has a specific orientation which might be imperfectly aligned with the lab-frame axes. In contrast, coherent averaging over a specific rotational quantum number would imply a complete lack of orientation of each individual molecule.

To explore the impact of imperfect orientation on the EFDs, we calculate the flux densities at a particular time  $T = 6$  fs after the end of the pulse with parameters specified in Fig. 5.4. For this purpose, we investigate the charge migration driven by linearly polarized laser in the  $yz$  plane. In this scenario, we have flexibility to rotate the molecule in planes containing the normal axis, i.e.,  $yz$  and  $xz$  planes as  $z$  axis is our normal axis. The EFDs are calculated to interpret the effect of different molecular orientations. Fig. 5.8(a) presents the charge distributions for the molecule rotated by  $\pm 10^\circ$ ,  $\pm 20^\circ$  and  $\pm 30^\circ$  along  $z$  axis at  $T = 6$  fs during field-free charge migration. As reflected from the figure, the charge distributions are similar for the different values of rotational averaging. Note that the populations in the excited enantiomers changes as we rotate the chiral molecule in space.

The average flux densities for larger-angle rotations are obtained by taking the average over the flux densities at all smaller-angle rotations. For example, the average flux densities for  $\pm 30^\circ$  rotations are obtained from the flux densities averaged incoherently over  $0^\circ$ ,  $\pm 10^\circ$ ,  $\pm 20^\circ$  and  $\pm 30^\circ$  rotations. The average flux



densities for both the enantiomers are presented in Fig. 5.8(b). It is evident from the figure that the average flux densities for  $\pm 10^\circ$ ,  $\pm 20^\circ$  and  $\pm 30^\circ$  rotations are very similar, while they differ quantitatively from the flux densities for the space-fixed case, i.e.,  $0^\circ$  rotation. If we consider the flux densities around individual atoms separately, say around the oxygen atom, there is a marked changes in the magnitude of the flux densities. The presence of a noticeable amount of flux densities around chiral carbon and upper carbon atoms are significantly different from the flux densities associated with the space-fixed molecule. The physical origin of these changes in the flux densities is the variations in the phases due to the different orientations. Nonetheless, the main findings remain unchanged: linearly polarized pulse in the  $yz$  plane induces charge migration and the associated time-dependent EFDs are found to be different for enantiomer pairs, unrelated by mirror reflection.

### 5.1.2 Imaging charge migration by TRXD

As we have seen that the linearly polarized pulse in the  $yz$  plane induces charge migration, which is drastically different for the enantiomers (see Fig. 5.4). This makes them to study in further detail. We employ TRXD to image the induced charge migration in this particular case. Moreover, to make a connection between the EFD and TRXD signal, EFDs are projected in two different planes as shown in Fig. 5.9. Thus, let us discuss the projected flux densities in detail before we discuss the results of TRXD.

The EFDs accompanying the charge migration for both enantiomers are presented in Fig. 5.9. To avoid the fast oscillating contribution stemming from the coherent interaction with the ground state in the charge migration, only contributions from the excited states are considered in the reconstructed signal. Snapshots are presented for 2 fs, 6 fs, 10 fs, and 14 fs, and the 2D representation in the  $xz$  plane is obtained by integrating over the  $y$  coordinate. The arrows of the vector field are color-coded according to their magnitude. In both enantiomers, almost all the flux density is concentrated around the oxygen atom (in maroon). It is important to mention that, maybe surprisingly, the chiral carbon atom is not involved

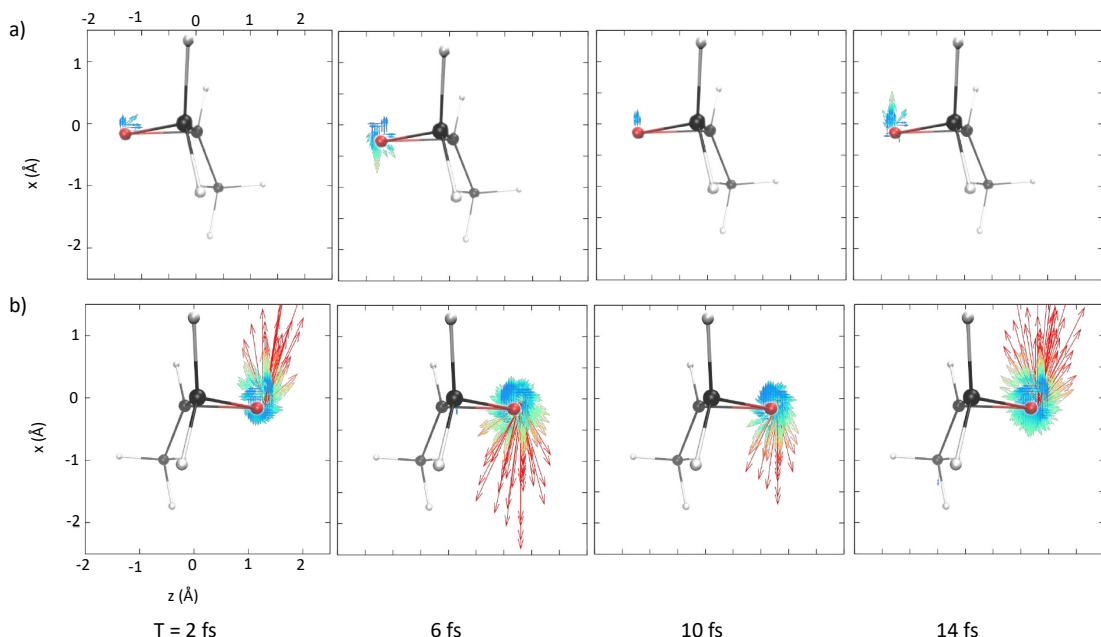


Figure 5.9: Time-dependent electronic flux densities for (a) R- and, (b) S-enantiomers of epoxyp propane in the  $xz$  plane at 2 fs, 6 fs, 10 fs, and 14 fs after the pump pulse. Violet, maroon and gray colors are representing carbon, oxygen and hydrogen atoms, respectively. Here,  $z$  axis is defined as the chiral axis in the molecular frame of reference.

in the dynamics, as revealed by the transient flux densities. The most striking difference lies in the magnitude of the fluxes. The strength of the flux densities for R-enantiomer is weak in comparison to S-enantiomer during the charge migration. At all times, they both exhibit a similar circular pattern around the oxygen atom. The direction of the circular charge migration changes as the dynamics progresses.

Since the direction of the electron flow is more prominent for the S-enantiomer, as reflected from Fig. 5.9(b), it can therefore be more readily described. Arrows corresponding to the flux densities are emerging from the oxygen atom along all directions, corresponding to an approximately circular flux density. Yet, the longest arrows in red represent the most probable direction for the flow of electrons, and these are changing with time. At 2 fs, arrows are mostly emerging along the positive  $x$ -direction and it is almost reversed in the next snapshot, i.e., at 6 fs. The flux densities for the S-enantiomer are along the same direction at 2 fs and 14 fs, which indicate the partial recurrence. Similar observations can be made for the circular component of the flux density in the R-enantiomer, where the direction

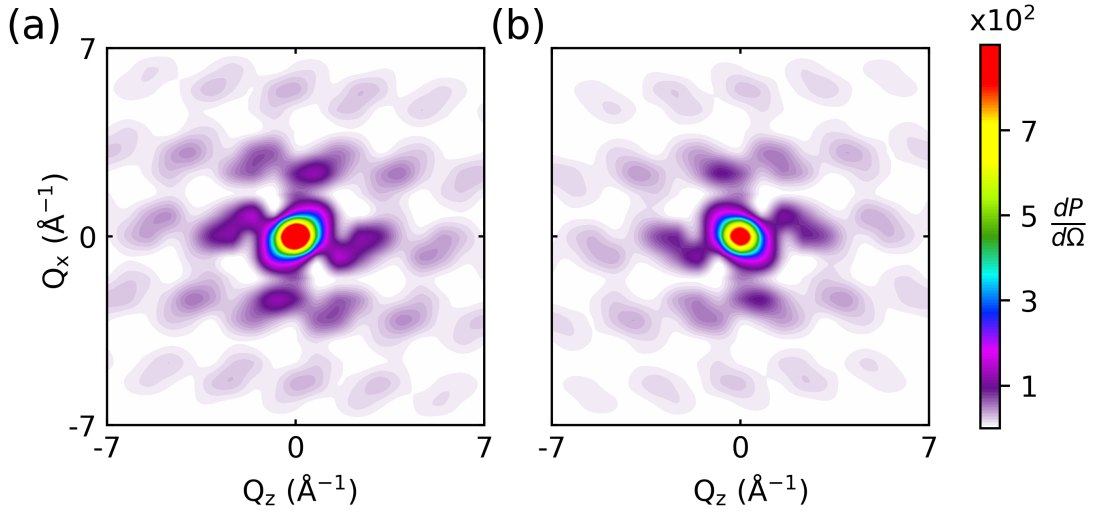


Figure 5.10: Time-independent diffraction patterns for (a) R- and (b) S- enantiomers of epoxypropane on left and right panels, respectively. The diffraction patterns are presented in  $Q_z - Q_x$  plane in units of  $dP_e/d\Omega$ . An ultrashort x-ray pulse of 8 keV mean energy is aimed to obtain 1.55  $\text{\AA}$  spatial resolution in these simulations. All diffracted photons up to  $60^\circ$  are collected in the detector.

of the circular flux is opposite to that of the S-enantiomer. On the contrary, the flux component with the largest magnitude points in the same direction for both enantiomers at all times. A tentative explanation could be that the circular component stems from the phase transferred to the molecule by the laser pulse. This leads to opposite relative phases among the three excited states. On the other hand, the dominant component of the flux density could be associated with the response of the electron cloud in the laser pulse during the preparation phase. This electronic response behaviour would then be inherited by the subsequent charge migration dynamics, explaining that both enantiomers react with the same phase.

The different timescale of the charge migration can be understood by analysing the characteristic timescales involved in the system, i.e.,  $\tau = h/\Delta E$  where  $\Delta E$  is the energy difference between two eigenstates. The characteristic timescales corresponding to  $E_3 = 7.56$  eV,  $E_4 = 7.73$  eV, and  $E_5 = 7.84$  eV are  $\tau_{43} = 24.32$  fs,  $\tau_{53} = 14.77$  fs and  $\tau_{54} = 37.59$  fs. Different contributions of the excited states and their respective interference including these timescales are the reason for non-identical charge migration in the two excited enantiomers.

After the pump pulse and in the absence of an external field, the time-dependent

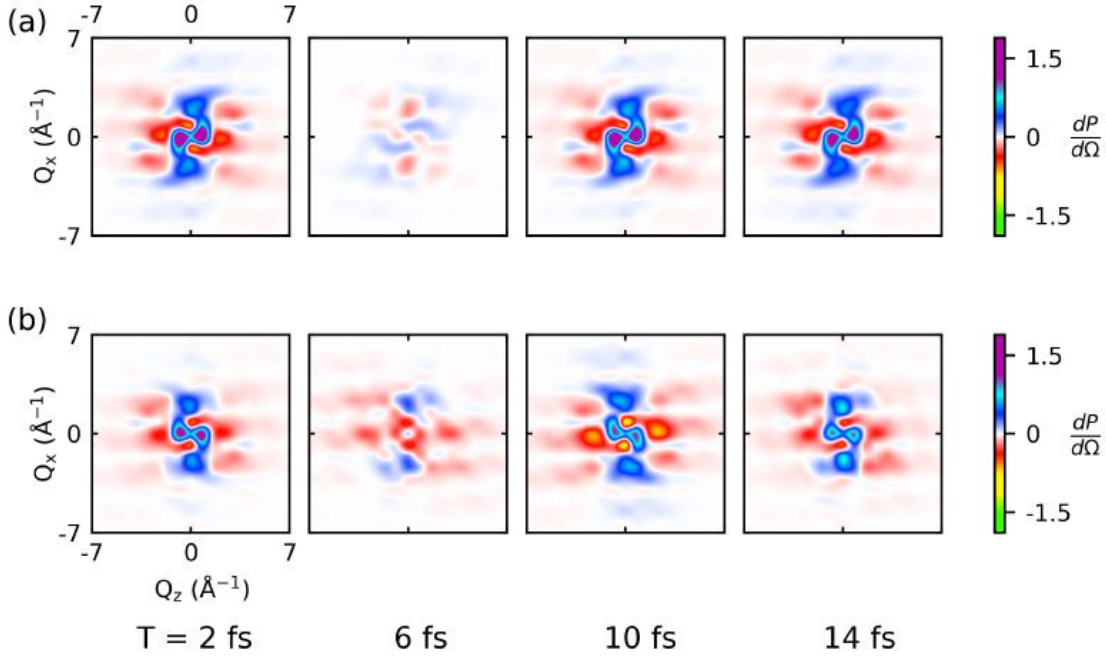


Figure 5.11: Time-resolved diffraction patterns for (a) R- and, (b) S-enantiomers of epoxypropane in  $Q_z - Q_x$  plane at 2 fs, 6 fs, 10 fs, and 14 fs. Intensity of the diffraction patterns is presented in units of  $dP_e/d\Omega$ . Here, time-dependent diffraction signal at  $T = 0$  fs is subtracted to the subsequent delay time. An ultrashort x-ray pulse of 8 keV mean energy is aimed to obtain 1.55 Å spatial resolution in these simulations. All diffracted photons up to  $60^\circ$  are collected in the detector.

coefficients in Eq. (2.0.5) simplify to the analytical form containing amplitude and energy-dependent phase. At  $T = 0$ , Eq. (2.3.8) reduces to time-independent diffraction signal as

$$\frac{dP}{d\Omega} = \frac{dP_e}{d\Omega} \sum_f \left| \sum_k C_k \int d\mathbf{r} \langle \Phi_f | \hat{\rho}(\mathbf{r}) | \Phi_k \rangle e^{-i\mathbf{Q} \cdot \mathbf{r}} \right|^2. \quad (5.1.1)$$

As evident from the above equation, the time-independent diffraction signal is emerging from the joint contribution of the elastic and time-independent inelastic parts of the total diffraction signal. This term serves as a constant background in TRXD.

The time-independent contributions to the total diffraction signal for both the enantiomers after the excitation are presented in Fig. 5.10. These signals are simulated using Eq. (5.1.1). From the figure, one can see that the time-independent

diffraction signals are different for both enantiomers. First, the intensity of the time-independent signal is stronger for the R-enantiomer in comparison to the S-enantiomer. This is especially true in the low-momentum region. Also, the signals are not mirror images of each other, which could allow to discriminate between the enantiomers by simple inspection of the two diffraction signals. Since these diffraction signals are static in nature, the dynamical information about the charge migration is lost.

To image the charge migration, we present time-dependent difference diffraction signals where the total diffraction signal at zero delay time is subtracted from the subsequent delay times. To simulate time-resolved diffraction signal, the DSP is computed according to Eq.(2.3.8). The six lowest-lying excited eigenstates (i.e.,  $f = [0, 6]$ ) were sufficient to obtain the converged diffraction signals within the assumption that the sum-over-states expression truncation due to the detector response.

Time-resolved diffraction signals at selected delay times for both the enantiomers are presented in Fig. 5.11. The total diffraction signal at  $T = 0$  fs is subtracted from the signal at subsequent delay times. It is observed that the time-independent signal is three orders of magnitude stronger than this time-dependent signal. Similar observations have been reported earlier in the case of TRXD for different systems (Carrascosa et al., 2021; Keefer et al., 2021). In spite of having low magnitude, the information about ultrafast dynamics of charge migration is imprinted in the difference diffraction signals as they are significantly different for both enantiomers at different delay times. The central parts as well as the higher momenta signals are changing in a very distinct way for both enantiomers. Note that  $\langle \Phi_i | \Phi_j \rangle$  is not exactly zero in our case due to numerical limitations, which impose a small but finite value with threshold value of  $10^{-5}$  on the LR-TDDFT coefficients. This, together with the numerical coefficient re-normalization, explain the small but non-zero value of the diffraction signal at the centre in Fig. 5.11.

By comparing the time-dependent diffraction pattern of the enantiomers at 2 fs, it can be seen that the overall signals are not very different for both enantiomers. There are two lobes of positive signal around the centre and they are of almost same

intensity with different orientations for the respective enantiomers. The negative part of the signal is scattered at higher momenta. There is a mismatch in the intensity at the central part of the lobes for two enantiomers.

At the next time step, i.e., at 6 fs, the diffraction signal reduces significantly for the R-enantiomer. In contrast, the signal is just reversed in the central part, dominated by negative extrema and spreading to higher momenta for S-enantiomer. The signal at 10 fs is comparable with the signal at 6 fs, but the orientation of the signal is different. On the contrary, for the R-enantiomer, the signal at 6 fs is similar to the one at 2 fs, and there is a slight decrease in diffraction intensity at 14 fs. The time-period of the time-dependent signal correlates well with the timescale of the charge migration found in the flux density for the enantiomers as shown in Fig. 5.9.

In order to understand how the time-dependent diffraction signals are related to the flux density, time-derivative of electron density in momentum space,  $|\partial_t \rho(\mathbf{Q})|$ , at selected delay times are presented in Fig. 5.12.  $|\partial_t \rho(\mathbf{Q})|$  is zero at  $T = 0$  fs [see Eq. (S7) in Ref. (Hermann et al., 2020)]. Therefore, subtracting  $|\partial_t \rho(\mathbf{Q})|$  at  $T = 0$  fs is not required.  $|\partial_t \rho(\mathbf{Q})|$  is related to the flux densities, and it can be obtained by Fourier transform of the electronic continuity equation [see Eq. (2.2.13)].

For both the enantiomers, the overall signal of  $|\partial_t \rho(\mathbf{Q})|$  decreases drastically from 2 fs to 6 fs. There is a partial revival of the signal at 10 fs for the R-enantiomer as observed in Figs. 5.9 and 5.11. The intensity of  $|\partial_t \rho(\mathbf{Q})|$  at 14 fs increases compared to that in 10 fs for R-enantiomer. In contrast,  $|\partial_t \rho(\mathbf{Q})|$  for S-enantiomer at 14 fs is approximately similar to the one at 2 fs.

As evident from Figs. 5.11 and 5.12, it is not straightforward to establish one-to-one visual correspondent between DSP and  $|\partial_t \rho(\mathbf{Q})|$ , which is in contrast to the earlier work discussed in Ref. (Hermann et al., 2020)). There are two simple reasons behind this: the first one is that more than two electronic states are contributing to the electronic wavepacket in epoxypropane. As a result, time-dependent terms yield more than one sine term in the expression of  $|\partial_t \rho(\mathbf{Q})|$  [see Eq. (S7) in Ref. (Hermann et al., 2020)]. The other reason can be attributed to significant contribution stemming from sine square term in comparison to the sine

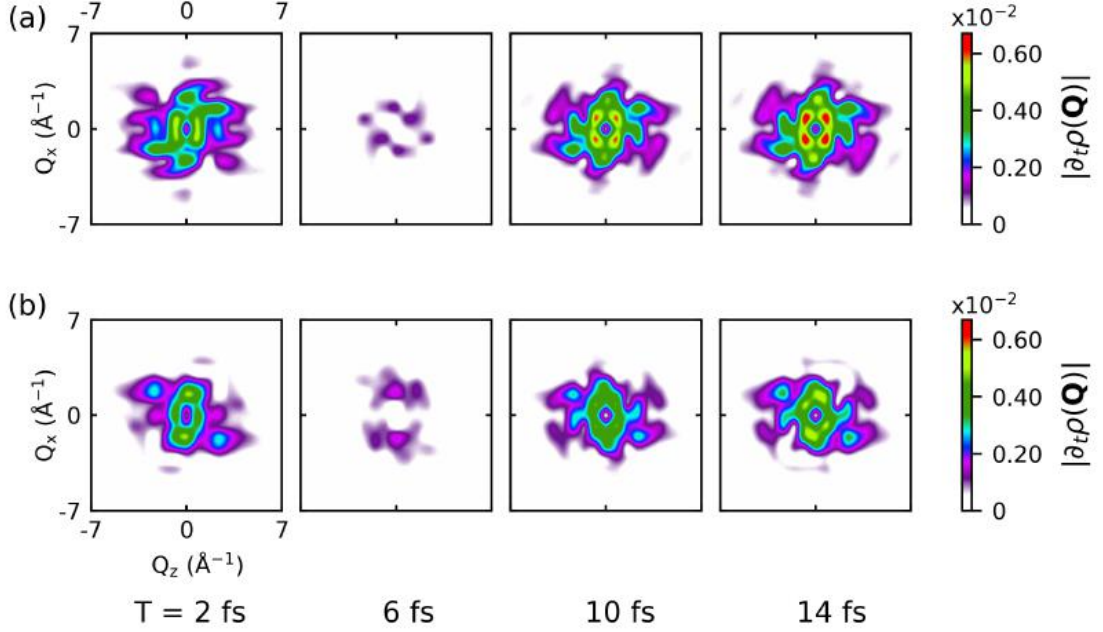


Figure 5.12: Time-derivative of electron density in momentum space,  $|\partial_t \rho(\mathbf{Q})|$ , for (a) R- and, b) S-enantiomers of epoxypropane in  $Q_z - Q_x$  plane at 2 fs, 6 fs, 10 fs, and 14 fs.

term in the expression of  $\Delta dP/d\Omega$  [see Eq. (S12) in Ref. (Hermann et al., 2020)]. These findings are in contrast to earlier case, where the wavepacket was composed of only two electronic states, and the sine square term was negligibly small in comparison to the sin term (Hermann et al., 2020). Therefore, the comparison between DSP and  $|\partial_t \rho(\mathbf{Q})|$  can only be qualitative.

As the time-resolved diffraction signals for two enantiomers are different, we can define the asymmetry parameter as

$$Y = \frac{\sigma_R - \sigma_S}{\sigma_R + \sigma_S}, \quad (5.1.2)$$

where  $\sigma_R$  and  $\sigma_S$  are the DSP of R- and S-enantiomers, respectively. Here, the DSP is represented by  $\sigma$  as a compact notation. Figures 5.13(a) and 5.13(b) present, respectively, the asymmetry parameter along  $Q_x$  and  $Q_z$  axes as a function of time. The domination of the red part over the blue is an indication that the signal for the S-enantiomer is stronger than the R-enantiomer along  $Q_x$  axis. If we look only around the  $Q_x = 0$  line, the signal for R-enantiomer is dominating over

S-enantiomer for all the time steps. The case is almost reversed for  $Q_x \neq 0$ .

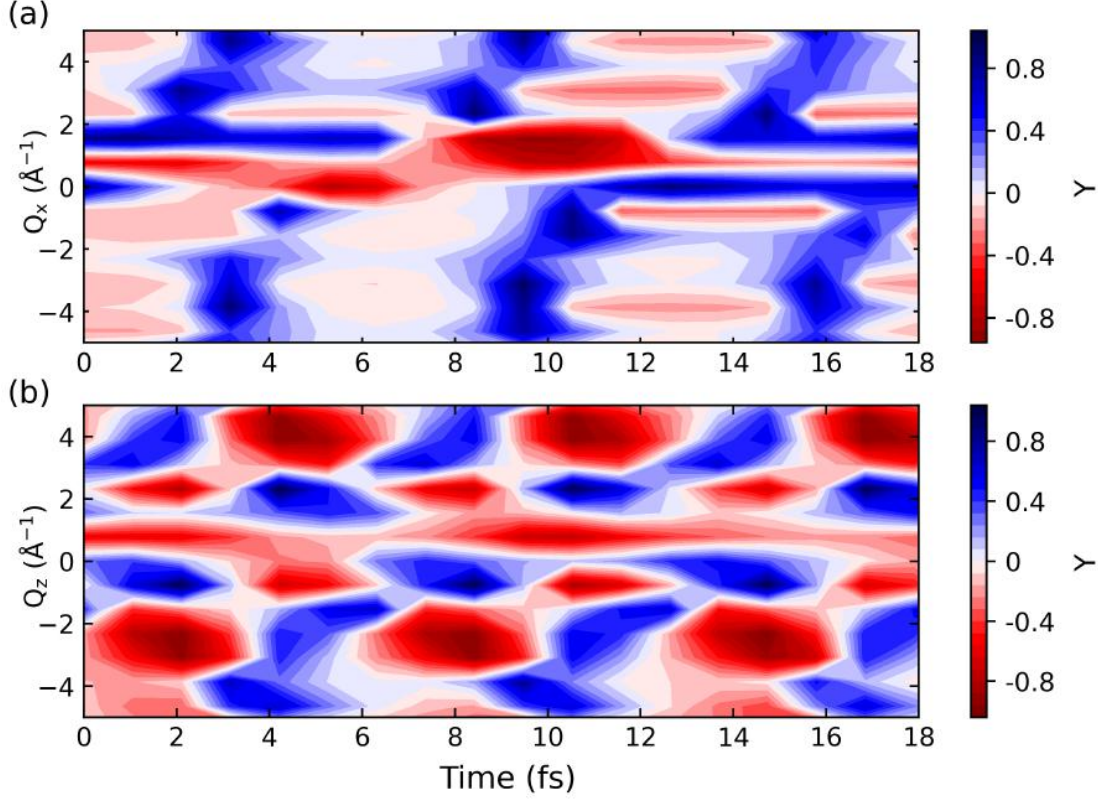


Figure 5.13: Asymmetry parameter  $Y$  along (a)  $Q_x$  and, (b)  $Q_z$  axes as a function of the delay time. The 1D TRXD signal is obtained from Eq. (2.3.8) and integrated along the other axes.

The signals are more interesting along the chiral axis, i.e., along  $Q_z$  axis. For a specific point in momentum space, the signal is changing in a periodic fashion. The same is true if we fix the time delay and walk along the  $Q_z$  axis. These signals encode important information about the dynamical evolution of the system, which is unique for a given choice of laser tagging parameters. The asymmetry parameter can be used to determine the enantiomeric ratio in a sample of unknown concentrations  $C_R$  and  $C_S$  in the R and S enantiomers, respectively. In this case, the measured signal of the unknown mixture is given as the weighted sum of the two signals,  $\sigma_{\text{sample}} = C_R\sigma_R + C_S\sigma_S$ . By subtracting from the TRXD signal of a pure enantiomer, say  $\sigma_R$ , this difference

$$\begin{aligned}\Delta\sigma &= \sigma_R - (C_R\sigma_R + C_S\sigma_S) \\ &= (1 - C_R)\sigma_R - C_S\sigma_S = C_S(\sigma_R - \sigma_S)\end{aligned}\tag{5.1.3}$$



can be simply normalized and related to the asymmetry parameter

$$\frac{\Delta\sigma}{\sigma_R + \sigma_S} = C_S \left( \frac{\sigma_R - \sigma_S}{\sigma_R + \sigma_S} \right) = C_S Y, \quad (5.1.4)$$

Hence, from the knowledge of the TRXD signals of both enantiomers, the concentration of an enantiomer can be directly obtained by comparing the intensity of the difference signal with that of the asymmetry parameter. As the dynamics becomes more intricate at longer times, the time-dependent monitoring of the difference signal would potentially lead to a more precise determination of the concentrations.

## 5.2 Summary

In summary, we have explored how time-resolved electron densities and associated EFDs behave when chiral molecules are driven by linearly polarized pulses. Moreover, it is shown by means of numerical simulations that the signature of chirality in molecules can be studied by the choice of orientation in linearly polarized laser excitation, which determines how enantiomers are driven out-of-equilibrium. Our findings are valid for molecules with fixed spatial orientation as well as for floppy molecules with imperfect degree of orientation. It has been shown that two linearly polarized pulses can orient the chiral molecules in a specific direction (Tutunnikov et al., 2018). Particularly, epoxyp propane and other chiral molecules can be oriented in space for sufficiently long times (of order of few picoseconds) using twisted polarization (Milner et al., 2019; Tutunnikov et al., 2020). The enantiomers are oriented in such a manner to retain the mirror symmetry at the end of the second pulse. Our work, discussed in this chapter, utilizes such oriented enantiomers while driving them out of equilibrium and opens new avenues for imaging time-dependent EFD and associated charge distributions in enantiomers. In recent years, methods based on electric field-dipole interaction have gained importance as they provide strong enantioselective signal (Ordonez and Smirnova, 2018). Our method for generating EFD belongs to this family of novel field-dipole based methods, and it is compatible with large, floppy chiral molecules. Our method is different from photoexcitation

circular dichroism where enantiospecific bound electronic wavepacket in a randomly oriented molecules is launched by broadband circularly polarized pulse and linearly polarized pulse is used to ionised the bound electronic wavepacket (Beaulieu et al., 2018). In contrast to that, in this chapter, linearly polarized pulse is used to prepare enantiospecific bound electronic wavepacket in an oriented chiral molecule. Moreover, we image the induced charge migration in epoxypropane using TRXD. The charge migration in an oriented epoxypropane is triggered by a linearly polarized pulse at  $45^\circ$  in the  $yz$  plane in the molecular frame of reference. For each enantiomer, the induced charge migration is different, and is imaged by TRXD. The dominating time-independent as well as difference TRXD signals are analysed separately. It is found that time-dependent difference signals are significantly different for both enantiomers. We believe that the present proof-of-principle results motivate to follow laser-induced charge migration in chiral molecules followed by TRXD. In particular, this could pave the way for a new, sensitive technique to determine the enantiomeric concentrations in unknown samples.

# Chapter 6

## Conclusions and Future Directions

### 6.1 Conclusions

Present thesis is aimed to understand the impact of various molecular symmetries in different molecules on attosecond charge migration. For this purpose, time-dependent electronic charge distributions and associated flux densities are used for spatiotemporal representation of the charge migration. Furthermore, TRXD is employed for four-dimensional imaging of the charge migration in selected cases.

Starting with preparatory works about previously studied charge migration in “highly symmetric” benzene with  $\mathcal{D}_{6h}$  symmetry, we have investigated how the charge migration will behave in different five-membered ring-shaped aromatic molecules. To this end, emphasis has been placed on those molecules that are neutral as opposed to ionic homocyclic and nonaromatic pentagon molecules. In **Chapter3**, we have examined how charge migration in five-membered ring-shaped neutral molecules, such as pyrrole, furan, and oxazole, is influenced by symmetry reduction and electronegativity of the foreign atom(s). To compare the charge migration in these three molecules on equal footing, similar laser parameters are chosen to get the population in the target excited states with nodal structure adjacent to the foreign atom(s). The direction of the charge migration and its spatial distribution are understood by means of the time-dependent difference electronic charge and flux densities. The presence of nitrogen and oxygen causes significantly different charge migration in pyrrole and furan, respectively; despite having

identical  $C_{2v}$  symmetry. The changes in the electron densities in pyrrole are primarily positioned at atoms, whereas the difference electron densities are delocalized around the bonds in furan. Analysis of the flux densities unravel atom-to-bond and bond-to-atom charge migration in pyrrole and furan, respectively.  $C_{2v}$  symmetry is imprinted at different instances during the attosecond charge migration in both molecules. As the symmetry is reduced from  $C_{2v}$  to  $C_s$  for oxazole, the time-dependent charge and flux densities display no reflection symmetry during charge migration. The difference electron densities are neither located at atoms nor at bonds in oxazole, which results a swirling motion originating from the lower left carbon to the lower right carbon through the space between the nitrogen and oxygen atom. Thus, it is concluded that the charge migration is sensitive to the point group symmetry via the presence of foreign atom(s), such as nitrogen in pyrrole, oxygen in furan; and nitrogen and oxygen in oxazole.

Following the charge migration in planar molecules, **Chapter 4** is dedicated to understand the role of the structural saddling on the charge migration in copper corrole in which two nitrogen atoms are out-of-plane and exhibits  $C_2$  symmetry. To explore how the out-of-plane nitrogen atoms affect the charge migration, a linearly polarized pump pulse is used to initiate coherent electronic motion. Time-dependent charge and flux densities are used to understand the simulated results. Analysis of the electronic flux density reveals that the diagonal nitrogen atoms mediate coherent charge migration between them via a central copper atom. In this chapter, TRXD is employed to image the charge migration. It is found that the signature of the saddling in copper corrole during charge migration is imprinted in time-resolved diffraction signals. To further assert the role of the saddling, a comparison of the static diffraction signals of nonsaddled planar copper porphyrin and saddled nonplanar copper corrole in their ground states is made.

After analyzing roles of different symmetries in molecules on the charge migration, **Chapter 5** is focused on the charge migration in molecules without any symmetry. For this purpose, epoxypropane – a chiral molecule with  $C_1$  symmetry, i.e., absence of molecular symmetry, is chosen. In general, circularly polarized light is used to probe the chirality in molecules. In this chapter, different orientations

of the linearly polarized pulses are used to induce charge migration in space-fixed R- and S-enantiomers of epoxypropane. It has been demonstrated that the selective orientation of R- and S-enantiomers of epoxypropane in lab frame is possible with the help of two linearly polarized pulses (Tutunnikov et al., 2018). After the orientation in lab frame, enantiomers exhibit mirror symmetry. However, it is not *a priori* obvious whether laser-induced charge migration in enantiomers will also display mirror symmetry or not. It has been found that the electronic population dynamics and the associated flux densities are identical when the enantiomers are driven by a linearly polarized pulse along  $x$  axis. These findings remain same for other linearly polarized pulses along  $y$  and  $z$  axes. On the other hand, if the enantiomers are driven by a linearly polarized pulse in the  $yz$  plane, the population dynamics and associated flux densities are drastically different for both enantiomers. Our observations remain valid for R- and S-enantiomers of epoxypropane with a fixed spatial orientation as well as for certain degree of imperfect orientation in lab frame.

Time-resolved x-ray diffraction is used for four-dimensional imaging of the charge migration in oriented epoxypropane, induced by a linearly polarized pulse at  $45^\circ$  in the  $yz$  plane. Detailed analysis of the x-ray diffraction signals reveals that the time-independent diffraction signal is two orders in magnitude higher than the time-dependent difference diffraction signals. Moreover, the time-independent diffraction signals for the two enantiomers differ remarkably from one another at higher momenta. Furthermore, a connection between TRXD and the electronic continuity equation is discussed by analysing the time-dependent diffraction signal and the time derivative of the total electron density in the momentum space. In this chapter, we have proposed a way to determine the concentration of an enantiomer in the racemic mixture by analyzing the asymmetry parameter stemming from the TRXD signal of a pure enantiomer. Our proposal could open an avenue to ascertain the enantiomeric contents in unidentified chiral molecules.

## 6.2 Future Directions

Attosecond charge migration is one of the important topics of attosecond physics in present days. We believe that our findings on imaging charge migration in different molecules will catalyze further theoretical and experimental works, particularly on laser-induced ultrafast processes in various metal corroles and other symmetry-reduced molecular systems.

Present thesis focused on inducing and probing charge migration in chiral molecule with one chiral (stereo) center. It is known that there exists  $2^n$  number of stereoisomers depending on the number of stereo centers,  $n$ , in a molecule. For example, there are two stereo centers in tartaric acid that generates four stereoisomers. The pairs of them which are connected by mirror reflection are called enantiomers and the pairs which are not connected by mirror reflection are known as diastereomers. There are not much research activities on light-induced charge migration in diastereomers till date. It will be very interesting to study the charge migration in the stereoisomers where they are connected with (enantiomers) or without (diastereomers) mirror reflection. Moreover, the spatiotemporal imaging of the charge migration to understand the role of the multiple stereo centers can also be investigated using EFDs and TRXD.

The origin of the homochirality is an open question as it is still unclear why asymmetry is naturally preferred, resulting in the survival of only one type of enantiomer in living objects in earth. Since light is the most frequent perturbation in nature, it might be conceivable to use either enantiomer transformation or enantiomer dissociation to understand why one enantiomer is preferred over another. The transformation could involve bond breaking and formation, which can be investigated using light-driven nuclear dynamics in enantiomer. This could potential contribute towards our understanding of homochirality.

Not only different molecules are interesting for various light-induced phenomena but also different properties of light can be harnessed to learn about various aspects of the charge migration in molecules. It is known that light carry an extra degree of freedom: orbital angular momentum (OAM) – associated with its spatial profile,

apart from known spin angular momentum associated with light's polarization. The OAM carrying beam is also known as helical or twisted beam. Investigating the interaction of twisted light with molecule is another topic for future study. The OAM of light has been extensively studied in the context of optical interferometry, quantum information processing, and nanoparticle manipulation, to name but a few. It would be interesting to explore how the helical laser pulse interacts with chiral molecules – leading to an emerging concept of time-resolved helical dichroism. Moreover, how helical ultrashort x-ray pulses could be useful for TRXD will be another open direction of research.

Attosecond charge migration is actively studied in various molecular systems and sheds light on various laser-driven processes in them. It would be interesting to extend such studies to solid-state systems, which is an unexplored territory. Additionally, there is a plenty of room for theory to motivate and support the design of upcoming state-of-the-art experiments with suitable pump-probe methods to probe charge migration. It would be interesting to apply attosecond transient-absorption spectroscopy, and time- and angle-resolved photoionization spectroscopy within pump-probe configuration to image the EFDs associated with the laser-induced charge migration in near future.





# Bibliography

ORBKIT download link. <https://github.com/orbkit/orbkit>. Accessed: 2020-10-05.

A. B. Alemayehu, E. Gonzalez, L. K. Hansen, and A. Ghosh. Copper corroles are inherently saddled. *Inorganic Chemistry*, 48(16):7794–7799, 2009.

J. L. Bada. Origins of homochirality. *Nature*, 374(6523):594–595, 1995.

M. Barbatti, M. Vazdar, A. J. Aquino, M. Eckert-Maksić, and H. Lischka. The nonadiabatic deactivation paths of pyrrole. *Journal of Chemical Physics*, 125(16):164323, 2006.

M. Barbatti, J. Pittner, M. Pederzoli, U. Werner, R. Mitrić, V. Bonačić-Koutecký, and H. Lischka. Non-adiabatic dynamics of pyrrole: Dependence of deactivation mechanisms on the excitation energy. *Chemical Physics*, 375(1):26–34, 2010.

L. Barron, M. Bogaard, and A. Buckingham. Raman scattering of circularly polarized light by optically active molecules. *Journal of the American Chemical Society*, 95(2):603–605, 1973.

L. D. Barron. *Molecular light scattering and optical activity*. Cambridge University Press, 2009.

I. Barth and J. Manz. Periodic electron circulation induced by circularly polarized laser pulses: Quantum model simulations for mg porphyrin. *Angewandte Chemie International Edition*, 45(18):2962–2965, 2006.

I. Barth, J. Manz, Y. Shigeta, and K. Yagi. Unidirectional electronic ring current driven by a few cycle circularly polarized laser pulse: quantum model simulations for mg- porphyrin. *Journal of the American Chemical Society*, 128(21):7043–7049, 2006.

- D. Baykusheva and H. J. Wörner. Chiral discrimination through bielliptical high-harmonic spectroscopy. *Physical Review X*, 8(3):031060, 2018.
- D. Baykusheva, D. Zindel, V. Svoboda, E. Bommeli, M. Ochsner, A. Tehlar, and H. J. Wörner. Real-time probing of chirality during a chemical reaction. *Proceedings of the National Academy of Sciences*, 116(48):23923–23929, 2019.
- S. Beaulieu, A. Comby, B. Fabre, D. Descamps, A. Ferré, G. Garcia, R. Gêneaux, F. Légaré, L. Nahon, S. Petit, et al. Probing ultrafast dynamics of chiral molecules using time-resolved photoelectron circular dichroism. *Faraday Discussions*, 194:325–348, 2016a.
- S. Beaulieu, A. Ferré, R. Gêneaux, R. Canonge, D. Descamps, B. Fabre, N. Fedorov, F. Légaré, S. Petit, T. Ruchon, et al. Universality of photoelectron circular dichroism in the photoionization of chiral molecules. *New Journal of Physics*, 18(10):102002, 2016b.
- S. Beaulieu, A. Comby, A. Clergerie, J. Caillat, D. Descamps, N. Dudovich, B. Fabre, R. Gêneaux, F. Légaré, S. Petit, et al. Attosecond-resolved photoionization of chiral molecules. *Science*, 358(6368):1288–1294, 2017.
- S. Beaulieu, A. Comby, D. Descamps, B. Fabre, G. Garcia, R. Gêneaux, A. Harvey, F. Légaré, Z. Mašín, L. Nahon, et al. Photoexcitation circular dichroism in chiral molecules. *Nature Physics*, 14(5):484–489, 2018.
- K. Bennett, M. Kowalewski, J. R. Rouxel, and S. Mukamel. Monitoring molecular nonadiabatic dynamics with femtosecond x-ray diffraction. *Proceedings of the National Academy of Sciences*, 115(26):6538–6547, 2018.
- A. Bergantini, M. J. Abplanalp, P. Pokhilko, A. I. Krylov, C. N. Shingledecker, E. Herbst, and R. I. Kaiser. A combined experimental and theoretical study on the formation of interstellar propylene oxide ( $\text{CH}_3\text{CHCH}_2\text{O}$ ) – a chiral molecule. *Astrophysical Journal*, 860(2):108, 2018.
- J. Bijvoet, A. Peerdeman, and A. Van Bommel. Determination of the absolute configuration of optically active compounds by means of x-rays. *Nature*, 168(4268):271–272, 1951.
- D. G. Blackmond. The origin of biological homochirality. *Cold Spring Harbor Perspectives in Biology*, 2(5):a002147, 2010.

- A. Bornschlegl, C. Logé, and U. Boesl. Investigation of cd effects in the multi photon ionisation of r-(+)-3-methylcyclopentanone. *Chemical Physics Letters*, 447(4-6):187–191, 2007.
- N. Böwering, T. Lischke, B. Schmidtke, N. Müller, T. Khalil, and U. Heinzmann. Asymmetry in photoelectron emission from chiral molecules induced by circularly polarized light. *Physical Review Letters*, 86(7):1187, 2001.
- T. Bredtmann, M. Ivanov, and G. Dixit. X-ray imaging of chemically active valence electrons during a pericyclic reaction. *Nature Communications*, 5(1):1–7, 2014.
- J. Breidbach and L. Cederbaum. Migration of holes: Formalism, mechanisms, and illustrative applications. *Journal of Chemical Physics*, 118(9):3983–3996, 2003.
- J. Breidbach and L. Cederbaum. Universal attosecond response to the removal of an electron. *Physical Review Letters*, 94(3):033901, 2005.
- M. Bröring, F. Brégier, E. Cónsul Tejero, C. Hell, and M. C. Holthausen. Revisiting the electronic ground state of copper corroles. *Angewandte Chemie International Edition*, 46(3):445–448, 2007.
- R. Burcl, R. D. Amos, and N. C. Handy. Study of excited states of furan and pyrrole by time-dependent density functional theory. *Chemical Physics Letters*, 355(1-2):8–18, 2002.
- F. Calegari, D. Ayuso, A. Trabattoni, L. Belshaw, S. De Camillis, S. Anumula, F. Frassetto, L. Poletto, A. Palacios, P. Decleva, et al. Ultrafast electron dynamics in phenylalanine initiated by attosecond pulses. *Science*, 346(6207):336–339, 2014.
- J. Cao, Z.-Z. Xie, and X. Yu. Excited-state dynamics of oxazole: A combined electronic structure calculations and dynamic simulations study. *Chemical Physics*, 474:25–35, 2016.
- A. M. Carrascosa, M. Yang, H. Yong, L. Ma, A. Kirrander, P. M. Weber, and K. Lopata. Mapping static core-holes and ring-currents with x-ray scattering. *Faraday Discussions*, 228:60–81, 2021.
- M. E. Casida. Time-dependent density-functional theory for molecules and molecular solids. *Journal of Molecular Structure: THEOCHEM*, 914(1-3):3–18, 2009.

- A. L. Cavalieri, N. Müller, T. Uphues, V. S. Yakovlev, A. Baltuška, B. Horvath, B. Schmidt, L. Blümel, R. Holzwarth, S. Hendel, et al. Attosecond spectroscopy in condensed matter. *Nature*, 449(7165):1029–1032, 2007.
- L. S. Cederbaum and J. Zobeley. Ultrafast charge migration by electron correlation. *Chemical Physics Letters*, 307(3-4):205–210, 1999.
- S. Chandra, I. N. Ansari, G. Dixit, F. Lepine, and A. Bhattacharya. Experimental evidence of sensitivity of the high harmonic generation to hydrogen bonding. *Journal of Physical Chemistry A*, 123(24):5144–5149, 2019.
- O. Christiansen and P. Jørgensen. The electronic spectrum of furan. *Journal of the American Chemical Society*, 120(14):3423–3430, 1998.
- O. Christiansen, J. Gauss, J. F. Stanton, and P. Jørgensen. The electronic spectrum of pyrrole. *Journal of Chemical Physics*, 111(2):525–537, 1999.
- R. Cireasa, A. Boguslavskiy, B. Pons, M. Wong, D. Descamps, S. Petit, H. Ruf, N. Thiré, A. Ferré, J. Suarez, et al. Probing molecular chirality on a sub-femtosecond timescale. *Nature Physics*, 11(8):654–658, 2015.
- A. Comby, S. Beaulieu, M. Boggio-Pasqua, D. Descamps, F. Légaré, L. Nahon, S. Petit, B. Pons, B. Fabre, Y. Mairesse, et al. Relaxation dynamics in photoexcited chiral molecules studied by time-resolved photoelectron circular dichroism: toward chiral femtochemistry. *Journal of Physical Chemistry Letters*, 7(22):4514–4519, 2016.
- D. P. Craig and T. Thirunamachandran. *Molecular quantum electrodynamics: an introduction to radiation-molecule interactions*. Courier Corporation, 1998.
- M. Defranceschi and G. Berthier. Symmetry properties in position and momentum space. *Journal de Physique*, 51(24):2791–2800, 1990.
- P. G. Demingos, N. M. Balzaretta, and A. R. Muniz. First-principles study of carbon nanothreads derived from five-membered heterocyclic rings: thiophene, furan and pyrrole. *Physical Chemistry Chemical Physics*, 23(3):2055–2062, 2021.
- D. J. Diestler. Coupled-channels quantum theory of electronic flux density in electronically adiabatic processes: fundamentals. *Journal of Physical Chemistry A*, 116(11):2728–2735, 2012.

- D. J. Diestler, A. Kenfack, J. Manz, B. Paulus, J. F. Pérez-Torres, and V. Pohl. Computation of the electronic flux density in the born–oppenheimer approximation. *Journal of Physical Chemistry A*, 117(36):8519–8527, 2013.
- G. Dixit and R. Santra. Role of electron-electron interference in ultrafast time-resolved imaging of electronic wavepackets. *Journal of Chemical Physics*, 138(13):134311, 2013.
- G. Dixit and R. Santra. Time-resolved ultrafast x-ray scattering from an incoherent electronic mixture. *Physical Review A*, 96(5):053413, 2017.
- G. Dixit, O. Vendrell, and R. Santra. Imaging electronic quantum motion with light. *Proceedings of the National Academy of Sciences*, 109(29):11636–11640, 2012.
- G. Dixit, J. M. Slowik, and R. Santra. Proposed imaging of the ultrafast electronic motion in samples using x-ray phase contrast. *Physical Review Letters*, 110(13):137403, 2013.
- G. Dixit, J. M. Slowik, and R. Santra. Theory of time-resolved nonresonant x-ray scattering for imaging ultrafast coherent electron motion. *Physical Review A*, 89(4):043409, 2014.
- G. Dixit, Á. Jiménez-Galán, L. Medišauskas, and M. Ivanov. Control of the helicity of high-order harmonic radiation using bichromatic circularly polarized laser fields. *Physical Review A*, 98(5):053402, 2018.
- D. K. Dogutan, R. McGuire Jr, and D. G. Nocera. Electrocatalytic water oxidation by cobalt (iii) hangman  $\beta$ -octafluoro corroles. *Journal of the American Chemical Society*, 133(24):9178–9180, 2011.
- I. Dreissigacker and M. Lein. Photoelectron circular dichroism of chiral molecules studied with a continuum-state-corrected strong-field approximation. *Physical Review A*, 89(5):053406, 2014.
- M. Drescher, M. Hentschel, R. Kienberger, M. Uiberacker, V. Yakovlev, A. Scrinzi, T. Westerwalbesloh, U. Kleineberg, U. Heinzmann, and F. Krausz. Time-resolved atomic inner-shell spectroscopy. *Nature*, 419(6909):803–807, 2002.

- T. H. Dunning Jr. Gaussian basis sets for use in correlated molecular calculations. i. the atoms boron through neon and hydrogen. *Journal of Chemical Physics*, 90(2):1007–1023, 1989.
- J. Duris, S. Li, T. Driver, E. G. Champenois, J. P. MacArthur, A. A. Lutman, Z. Zhang, P. Rosenberger, J. W. Aldrich, R. Coffee, et al. Tunable isolated attosecond x-ray pulses with gigawatt peak power from a free-electron laser. *Nature Photonics*, 14(1):30–36, 2020.
- S. Eibenberger, J. Doyle, and D. Patterson. Enantiomer-specific state transfer of chiral molecules. *Physical Review Letters*, 118(12):123002, 2017.
- P. Emma, R. Akre, J. Arthur, R. Bionta, C. Bostedt, J. Bozek, A. Brachmann, P. Bucksbaum, R. Coffee, F.-J. Decker, et al. First lasing and operation of an angstrom-wavelength free-electron laser. *Nature Photonics*, 4(9):641–647, 2010.
- M. Ernzerhof. Taylor-series expansion of density functionals. *Physical Review A*, 50(6):4593, 1994.
- P. Fischer and F. Hache. Nonlinear optical spectroscopy of chiral molecules. *Chirality: the Pharmacological, Biological, and Chemical Consequences of Molecular Asymmetry*, 17(8):421–437, 2005.
- H. Flack and G. Bernardinelli. Absolute structure and absolute configuration. *Acta Crystallographica Section A: Foundations of Crystallography*, 55(5):908–915, 1999.
- A. S. Folorunso, A. Bruner, F. Mauger, K. A. Hamer, S. Hernandez, R. R. Jones, L. F. DiMauro, M. B. Gaarde, K. J. Schafer, and K. Lopata. Molecular modes of attosecond charge migration. *Physical Review Letters*, 126(13):133002, 2021.
- M. J. Frisch, G. W. Trucks, H. B. Schlegel, G. E. Scuseria, M. A. Robb, J. R. Cheeseman, G. Scalmani, V. Barone, G. A. Petersson, H. Nakatsuji, et al. Gaussian 16, revision a. 03, gaussian. *Inc., Wallingford CT*, 2016.
- T. Geng, J. Ehrmaier, O. Schalk, G. W. Richings, T. Hansson, G. Worth, and R. D. Thomas. Time-resolved photoelectron spectroscopy studies of isoxazole and oxazole. *Journal of Physical Chemistry A*, 124(20):3984–3992, 2020.
- A. Ghosh, T. Wondimagegn, and A. B. Parusel. Electronic structure of gallium, copper, and nickel complexes of corrole. high-valent transition metal centers

- versus noninnocent ligands. *Journal of the American Chemical Society*, 122(21): 5100–5104, 2000.
- S. Giri, A. M. Dudzinski, J. C. Tremblay, and G. Dixit. Time-dependent electronic current densities in chiral molecules. *Physical Review A*, 102(6):063103, 2020.
- S. Giri, J. C. Tremblay, and G. Dixit. Imaging charge migration in chiral molecules using time-resolved x-ray diffraction. *Physical Review A*, 104(5):053115, 2021.
- S. Giri, J. C. Tremblay, and G. Dixit. Probing the effect of molecular structure saddling on ultrafast charge migration via time-resolved x-ray diffraction. *Physical Review A*, 106:033120, 2022.
- J. Glowia, A. Natan, J. Cryan, R. Hartsock, M. Kozina, M. Minitti, S. Nelson, J. Robinson, T. Sato, T. Van Driel, et al. Self-referenced coherent diffraction x-ray movie of angstrom-and femtosecond-scale atomic motion. *Physical Review Letters*, 117(15):153003, 2016.
- E. Goulielmakis, Z.-H. Loh, A. Wirth, R. Santra, N. Rohringer, V. S. Yakovlev, S. Zherebtsov, T. Pfeifer, A. M. Azzeer, M. F. Kling, et al. Real-time observation of valence electron motion. *Nature*, 466(7307):739–743, 2010.
- E. K. U. Gross, J. Dobson, and M. Petersilka. Density functional theory of time-dependent phenomena. *Density Functional Theory II*, pages 81–172, 1996.
- Z. Gross, G. Golubkov, and L. Simkhovich. Epoxidation catalysis by a manganese corrole and isolation of an oxomanganese (v) corrole. *Angewandte Chemie International Edition*, 39(22):4045–4047, 2000.
- V. Gruson, L. Barreau, Á. Jiménez-Galan, F. Risoud, J. Caillat, A. Maquet, B. Carré, F. Lepetit, J.-F. Hergott, T. Ruchon, et al. Attosecond dynamics through a fano resonance: Monitoring the birth of a photoelectron. *Science*, 354(6313):734–738, 2016.
- Y. Harada, E. Haraguchi, K. Kaneshima, and T. Sekikawa. Circular dichroism in high-order harmonic generation from chiral molecules. *Physical Review A*, 98(2):021401, 2018.
- C. J. Harding. *Photoelectron circular dichroism in gas phase chiral molecules*. PhD thesis, University of Nottingham, 2005.

- N. Hartmann, G. Hartmann, R. Heider, M. Wagner, M. Ilchen, J. Buck, A. Lindahl, C. Benko, J. Grünert, J. Krzywinski, et al. Attosecond time–energy structure of x-ray free-electron laser pulses. *Nature Photonics*, 12(4):215–220, 2018.
- A. G. Harvey, Z. Mašín, and O. Smirnova. General theory of photoexcitation induced photoelectron circular dichroism. *Journal of Chemical Physics*, 149(6):064104, 2018.
- L. He, S. Sun, P. Lan, Y. He, B. Wang, P. Wang, X. Zhu, L. Li, W. Cao, P. Lu, et al. Filming movies of attosecond charge migration in single molecules with high harmonic spectroscopy. *Nature Communications*, 13(1):1–9, 2022.
- T. Helgaker, P. Jorgensen, and J. Olsen. *Molecular electronic-structure theory*. John Wiley & Sons, 2014.
- H. Hennig, J. Breidbach, and L. S. Cederbaum. Electron correlation as the driving force for charge transfer: charge migration following ionization in n-methyl acetamide. *Journal of Physical Chemistry A*, 109(3):409–414, 2005.
- N. E. Henriksen and K. B. Møller. On the theory of time-resolved x-ray diffraction. *Journal of Physical Chemistry B*, 112(2):558–567, 2008.
- M. Hentschel, R. Kienberger, C. Spielmann, G. A. Reider, N. Milosevic, T. Brabec, P. Corkum, U. Heinzmann, M. Drescher, and F. Krausz. Attosecond metrology. *Nature*, 414(6863):509–513, 2001.
- G. Hermann and J. Tremblay. Ultrafast photoelectron migration in dye-sensitized solar cells: Influence of the binding mode and many-body interactions. *Journal of Chemical Physics*, 145(17):174704, 2016.
- G. Hermann, B. Paulus, J. Pérez-Torres, and V. Pohl. Electronic and nuclear flux densities in the  $\text{h}_2$  molecule. *Physical Review A*, 89(5):052504, 2014.
- G. Hermann, C. Liu, J. Manz, B. Paulus, J. F. Perez-Torres, V. Pohl, and J. C. Tremblay. Multidirectional angular electronic flux during adiabatic attosecond charge migration in excited benzene. *Journal of Physical Chemistry A*, 120(27):5360–5369, 2016a.
- G. Hermann, V. Pohl, J. C. Tremblay, B. Paulus, H.-C. Hege, and A. Schild. Orbkit: A modular python toolbox for cross-platform postprocessing of quantum chemical wavefunction data, 2016b.



- G. Hermann, C. Liu, J. Manz, B. Paulus, V. Pohl, and J. C. Tremblay. Attosecond angular flux of partial charges on the carbon atoms of benzene in non-aromatic excited state. *Chemical Physics Letters*, 683:553–558, 2017a.
- G. Hermann, V. Pohl, and J. C. Tremblay. An open-source framework for analyzing n-electron dynamics. ii. hybrid density functional theory/configuration interaction methodology. *Journal of Computational Chemistry*, 38(28):2378–2387, 2017b.
- G. Hermann, V. Pohl, G. Dixit, and J. C. Tremblay. Probing electronic fluxes via time-resolved x-ray scattering. *Physical Review Letters*, 124(1):013002, 2020.
- P. Herwig, K. Zawatzky, M. Grieser, O. Heber, B. Jordon-Thaden, C. Krantz, O. Novotný, R. Repnow, V. Schurig, D. Schwalm, et al. Imaging the absolute configuration of a chiral epoxide in the gas phase. *Science*, 342(6162):1084–1086, 2013.
- S. Hirata and M. Head-Gordon. Time-dependent density functional theory within the tamm–dancoff approximation. *Chemical Physics Letters*, 314(3-4):291–299, 1999.
- P. Hohenberg and W. Kohn. Inhomogeneous electron gas. *Physical Review*, 136(3B):B864, 1964.
- J. D. Hunter. Matplotlib: A 2d graphics environment. *Computing in Science & Engineering*, 9(03):90–95, 2007.
- Y. Inoue and V. Ramamurthy. *Chiral photochemistry*. CRC Press, 2004.
- T. Ishikawa, H. Aoyagi, T. Asaka, Y. Asano, N. Azumi, T. Bizen, H. Ego, K. Fukami, T. Fukui, Y. Furukawa, et al. A compact x-ray free-electron laser emitting in the sub-angstrom region. *Nature Photonics*, 6(8):540–544, 2012.
- M. H. Janssen and I. Powis. Detecting chirality in molecules by imaging photoelectron circular dichroism. *Physical Chemistry Chemical Physics*, 16(3):856–871, 2014.
- K. L. Jensen. *Introduction to the physics of electron emission*. John Wiley & Sons, 2017.

- D. Jia, J. Manz, B. Paulus, V. Pohl, J. C. Tremblay, and Y. Yang. Quantum control of electronic fluxes during adiabatic attosecond charge migration in degenerate superposition states of benzene. *Chemical Physics*, 482:146–159, 2017.
- X. Jiang, R.-X. Liu, H.-Y. Liu, and C. K. Chang. Corrole-based photodynamic antitumor therapy. *Journal of the Chinese Chemical Society*, 66(9):1090–1099, 2019.
- A. Johnson and I. Kay. 306. corroles. part i. synthesis. *Journal of the Chemical Society (Resumed)*, pages 1620–1629, 1965.
- D. Keefer, F. Aleotti, J. R. Rouxel, F. Segatta, B. Gu, A. Nenov, M. Garavelli, and S. Mukamel. Imaging conical intersection dynamics during azobenzene photoisomerization by ultrafast x-ray diffraction. *Proceedings of the National Academy of Sciences*, 118(3):e2022037118, 2021.
- F. Kelkensberg, W. Siu, J. F. Pérez-Torres, F. Morales, G. Gademann, A. Rouzée, P. Johnsson, M. Lucchini, F. Calegari, J. L. Sanz-Vicario, et al. Attosecond control in photoionization of hydrogen molecules. *Physical Review Letters*, 107(4):043002, 2011.
- S. Klinkusch and J. C. Tremblay. Resolution-of-identity stochastic time-dependent configuration interaction for dissipative electron dynamics in strong fields. *Journal of Chemical Physics*, 144(18):184108, 2016.
- W. Kohn and L. J. Sham. Self-consistent equations including exchange and correlation effects. *Physical Review*, 140(4A):A1133, 1965.
- K. Köksal and F. Koç. The effect of twisted light on the ring-shaped molecules: the manipulation of the photoinduced current and the magnetic moment by transferring spin and orbital angular momentum of high frequency light. *Computational and Theoretical Chemistry*, 1099:203–208, 2017.
- M. Kowalewski, K. Bennett, and S. Mukamel. Monitoring nonadiabatic avoided crossing dynamics in molecules by ultrafast x-ray diffraction. *Structural Dynamics*, 4(5):054101, 2017.
- P. M. Kraus, B. Mignolet, D. Baykusheva, A. Rupenyan, L. Horný, E. F. Penka, G. Grassi, O. I. Tolstikhin, J. Schneider, F. Jensen, et al. Measurement and laser control of attosecond charge migration in ionized iodoacetylene. *Science*, 350(6262):790–795, 2015.

- F. Krausz and M. Ivanov. Attosecond physics. *Reviews of Modern Physics*, 81(1):163, 2009.
- A. I. Kuleff and L. S. Cederbaum. Ultrafast correlation-driven electron dynamics. *Journal of Physics B*, 47(12):124002, 2014.
- A. I. Kuleff, J. Breidbach, and L. S. Cederbaum. Multielectron wave-packet propagation: General theory and application. *Journal of Chemical Physics*, 123(4):044111, 2005.
- J. Küpper, S. Stern, L. Holmegaard, F. Filsinger, A. Rouzée, A. Rudenko, P. Johnsson, A. V. Martin, M. Adolph, A. Aquila, et al. X-ray diffraction from isolated and strongly aligned gas-phase molecules with a free-electron laser. *Physical Review Letters*, 112(8):083002, 2014.
- M. Lara-Astiaso, M. Galli, A. Trabattoni, A. Palacios, D. Ayuso, F. Frassetto, L. Poletto, S. De Camillis, J. Greenwood, P. Decleva, et al. Attosecond pump-probe spectroscopy of charge dynamics in tryptophan. *Journal of Physical Chemistry Letters*, 9(16):4570–4577, 2018.
- S. Y. Lee and B. H. Boo. Molecular structures and vibrational spectra of pyrrole and carbazole by density functional theory and conventional ab initio calculations. *Journal of Physical Chemistry*, 100(37):15073–15078, 1996.
- C. S. Lehmann, N. B. Ram, I. Powis, and M. H. Janssen. Imaging photoelectron circular dichroism of chiral molecules by femtosecond multiphoton coincidence detection. *Journal of Chemical Physics*, 139(23):234307, 2013.
- M. Leibscher, T. F. Giesen, and C. P. Koch. Principles of enantio-selective excitation in three-wave mixing spectroscopy of chiral molecules. *Journal of Chemical Physics*, 151(1):014302, 2019.
- C. M. Lemon. Corrole photochemistry. *Pure and Applied Chemistry*, 92(12):1901–1919, 2020.
- F. Lépine, M. Y. Ivanov, and M. J. Vrakking. Attosecond molecular dynamics: fact or fiction? *Nature Photonics*, 8(3):195–204, 2014.
- R. Li, R. Sullivan, W. Al-Basheer, R. Pagni, and R. Compton. Linear and non-linear circular dichroism of r-(+)-3-methylcyclopentanone. *Journal of Chemical Physics*, 125(14):144304, 2006.

- H. Lim, K. E. Thomas, B. Hedman, K. O. Hodgson, A. Ghosh, and E. I. Solomon. X-ray absorption spectroscopy as a probe of ligand noninnocence in metallo-corroles: the case of copper corroles. *Inorganic Chemistry*, 58(10):6722–6730, 2019.
- E. Lindroth, F. Calegari, L. Young, M. Harmand, N. Dudovich, N. Berrah, and O. Smirnova. Challenges and opportunities in attosecond and xfel science. *Nature Reviews Physics*, 1(2):107–111, 2019.
- C. Liu, J. Manz, K. Ohmori, C. Sommer, N. Takei, J. C. Tremblay, and Y. Zhang. Attosecond control of restoration of electronic structure symmetry. *Physical Review Letters*, 121(17):173201, 2018.
- I. Luobeznova, L. Simkhovich, I. Goldberg, and Z. Gross. Electronic structures and reactivities of corrole- copper complexes. *European Journal of Inorganic Chemistry*, 2004(8):1724–1732, 2004.
- C. Lux, M. Wollenhaupt, T. Bolze, Q. Liang, J. Köhler, C. Sarpe, and T. Baumert. Circular dichroism in the photoelectron angular distributions of camphor and fenchone from multiphoton ionization with femtosecond laser pulses. *Angewandte Chemie International Edition*, 51(20):5001–5005, 2012.
- C. Lux, M. Wollenhaupt, C. Sarpe, and T. Baumert. Photoelectron circular dichroism of bicyclic ketones from multiphoton ionization with femtosecond laser pulses. *ChemPhysChem*, 16(1):115–137, 2015.
- A. Mahammed and Z. Gross. Corroles as triplet photosensitizers. *Coordination Chemistry Reviews*, 379:121–132, 2019.
- A. Mahammed, H. B. Gray, A. E. Meier-Callahan, and Z. Gross. Aerobic oxidations catalyzed by chromium corroles. *Journal of the American Chemical Society*, 125(5):1162–1163, 2003.
- E. P. Mansson, S. Latini, F. Covito, V. Wanie, M. Galli, E. Perfetto, G. Stefanucci, H. Hübener, U. De Giovannini, M. C. Castrovilli, et al. Real-time observation of a correlation-driven sub 3 fs charge migration in ionised adenine. *Communications Chemistry*, 4(1):1–7, 2021.
- M. A. Marques and E. K. U. Gross. Time-dependent density functional theory. *Annual Review of Physical Chemistry*, 55(1):427–455, 2004.

- M. A. Marques, N. T. Maitra, F. M. Nogueira, E. K. U. Gross, and A. Rubio. *Fundamentals of time-dependent density functional theory*, volume 837. Springer, 2012.
- R. L. Martin. Natural transition orbitals. *Journal of Chemical Physics*, 118(11): 4775–4777, 2003.
- J. Mauritsson, T. Remetter, M. Swoboda, K. Klünder, A. L’Huillier, K. Schafer, O. Ghafur, F. Kelkensberg, W. Siu, P. Johnsson, et al. Attosecond electron spectroscopy using a novel interferometric pump-probe technique. *Physical Review Letters*, 105(5):053001, 2010.
- V. May and O. Kühn. *Charge and energy transfer dynamics in molecular systems*. John Wiley & Sons, 2008.
- B. A. McGuire, P. B. Carroll, R. A. Loomis, I. A. Finneran, P. R. Jewell, A. J. Remijan, and G. A. Blake. Discovery of the interstellar chiral molecule propylene oxide (ch3chch2o). *Science*, 352(6292):1449–1452, 2016.
- D. McMorrow and J. Als-Nielsen. *Elements of modern X-ray physics*. John Wiley & Sons, 2011.
- U. J. Meierhenrich. Amino acids and the asymmetry of life. *European Review*, 21(2):190–199, 2013.
- I. C. Merritt, D. Jacquemin, and M. Vacher. Attochemistry: Is controlling electrons the future of photochemistry? *Journal of Physical Chemistry Letters*, 12(34): 8404–8415, 2021.
- A. A. Milner, J. A. Fordyce, I. MacPhail-Bartley, W. Wasserman, V. Milner, I. Tutunnikov, and I. S. Averbukh. Controlled enantioselective orientation of chiral molecules with an optical centrifuge. *Physical Review Letters*, 122(22):223201, 2019.
- D. M. P. Mingos and J. P. Dahl. *Molecular electronic structures of transition metal complexes II*, volume 2. Springer Science & Business Media, 2012.
- M. Minitti, J. Budarz, A. Kirrander, J. Robinson, D. Ratner, T. Lane, D. Zhu, J. Glowacki, M. Kozina, H. Lemke, et al. Imaging molecular motion: Femtosecond x-ray scattering of an electrocyclic chemical reaction. *Physical Review Letters*, 114(25):255501, 2015.

- M. P. Minitti, J. M. Budarz, A. Kirrander, J. Robinson, T. J. Lane, D. Ratner, K. Saita, T. Northey, B. Stankus, V. Cofer-Shabica, et al. Toward structural femtosecond chemical dynamics: imaging chemistry in space and time. *Faraday Discussions*, 171:81–91, 2014.
- K. Mori. Bioactive natural products and chirality. *Chirality*, 23(6):449–462, 2011.
- K. Nagashima and K. Takatsuka. Electron-wavepacket reaction dynamics in proton transfer of formamide. *Journal of Physical Chemistry A*, 113(52):15240–15249, 2009.
- L. Nahon, G. A. Garcia, C. J. Harding, E. Mikajlo, and I. Powis. Determination of chiral asymmetries in the valence photoionization of camphor enantiomers by photoelectron imaging using tunable circularly polarized light. *Journal of Chemical Physics*, 125(11):114309, 2006.
- Y. Nam, J. R. Rouxel, J. Y. Lee, and S. Mukamel. Monitoring aromatic ring-currents in mg-porphyrin by time-resolved circular dichroism. *Physical Chemistry Chemical Physics*, 22(45):26605–26613, 2020.
- S. Nardis, F. Mandoj, M. Stefanelli, and R. Paolesse. Metal complexes of corrole. *Coordination Chemistry Reviews*, 388:360–405, 2019.
- O. Neufeld, D. Ayuso, P. Decleva, M. Y. Ivanov, O. Smirnova, and O. Cohen. Ultra-sensitive chiral spectroscopy by dynamical symmetry breaking in high harmonic generation. *Physical Review X*, 9(3):031002, 2019.
- M. Nisoli, P. Decleva, F. Calegari, A. Palacios, and F. Martín. Attosecond electron dynamics in molecules. *Chemical Reviews*, 117(16):10760–10825, 2017.
- M. Okuyama and K. Takatsuka. Electron flux in molecules induced by nuclear motion. *Chemical Physics Letters*, 476(1-3):109–115, 2009.
- M. Okuyama and K. Takatsuka. Dynamical electron mechanism of double proton transfer in formic acid dimer. *Bulletin of the Chemical Society of Japan*, 85(2):217–227, 2012.
- A. F. Ordonez and O. Smirnova. Generalized perspective on chiral measurements without magnetic interactions. *Physical Review A*, 98(6):063428, 2018.

- M. H. Palmer, I. C. Walker, C. C. Ballard, and M. F. Guest. The electronic states of furan studied by vuv absorption, near-threshold electron energy-loss spectroscopy and ab initio multi-reference configuration interaction calculations. *Chemical Physics*, 192(2):111–125, 1995.
- K. Pande, C. D. Hutchison, G. Groenhof, A. Aquila, J. S. Robinson, J. Tenboer, S. Basu, S. Boutet, D. P. DePonte, M. Liang, et al. Femtosecond structural dynamics drives the trans/cis isomerization in photoactive yellow protein. *Science*, 352(6286):725–729, 2016.
- S. Patchkovskii. Electronic currents and born-oppenheimer molecular dynamics. *Journal of Chemical Physics*, 137(8):084109, 2012.
- D. Patterson, M. Schnell, and J. M. Doyle. Enantiomer-specific detection of chiral molecules via microwave spectroscopy. *Nature*, 497(7450):475–477, 2013.
- P.-M. Paul, E. S. Toma, P. Breger, G. Mullot, F. Augé, P. Balcou, H. G. Muller, and P. Agostini. Observation of a train of attosecond pulses from high harmonic generation. *Science*, 292(5522):1689–1692, 2001.
- C. Pellegrini, A. Marinelli, and S. Reiche. The physics of x-ray free-electron lasers. *Reviews of Modern Physics*, 88(1):015006, 2016.
- M. Peplow. The next big hit in molecule hollywood. *Nature*, 544(7651):408, 2017.
- K. Pierloot, H. Zhao, and S. Vancoillie. Copper corroles: the question of noninnocence. *Inorganic Chemistry*, 49(22):10316–10329, 2010.
- M. Pitzer, M. Kunitski, A. S. Johnson, T. Jahnke, H. Sann, F. Sturm, L. P. H. Schmidt, H. Schmidt-Böcking, R. Dörner, J. Stohner, et al. Direct determination of absolute molecular stereochemistry in gas phase by coulomb explosion imaging. *Science*, 341(6150):1096–1100, 2013.
- M. Pitzer, G. Kastirke, M. Kunitski, T. Jahnke, T. Bauer, C. Goihl, F. Trinter, C. Schober, K. Henrichs, J. Becht, et al. Absolute configuration from different multifragmentation pathways in light-induced coulomb explosion imaging. *ChemPhysChem*, 17(16):2465–2472, 2016.
- V. Pohl, G. Hermann, and J. C. Tremblay. An open-source framework for analyzing n-electron dynamics. i. multideterminantal wave functions. *Journal of Computational Chemistry*, 38(17):1515–1527, 2017.

- V. Pohl, L. E. Marsoner Steinkasserer, and J. C. Tremblay. Imaging time-dependent electronic currents through a graphene-based nanojunction. *Journal of Physical Chemistry Letters*, 10(18):5387–5394, 2019.
- I. Powis. Photoelectron circular dichroism of the randomly oriented chiral molecules glyceraldehyde and lactic acid. *Journal of Chemical Physics*, 112(1):301–310, 2000.
- V. I. Prokhorenko, A. M. Nagy, and R. D. Miller. Coherent control of the population transfer in complex solvated molecules at weak excitation. an experimental study. *Journal of Chemical Physics*, 122(18):184502, 2005.
- P. Ramachandran and G. Varoquaux. Mayavi: 3d visualization of scientific data. *Computing in Science & Engineering*, 13(2):40–51, 2011.
- F. Remaille and R. D. Levine. An electronic time scale in chemistry. *Proceedings of the National Academy of Sciences*, 103(18):6793–6798, 2006.
- B. Ritchie. Theory of the angular distribution of photoelectrons ejected from optically active molecules and molecular negative ions. *Physical Review A*, 13(4):1411, 1976.
- B. O. Roos, P.-A. Malmqvist, V. Molina, L. Serrano-Andrés, and M. Merchán. Theoretical characterization of the lowest-energy absorption band of pyrrole. *Journal of Chemical Physics*, 116(17):7526–7536, 2002.
- S. Rozen, A. Comby, E. Bloch, S. Beauvarlet, D. Descamps, B. Fabre, S. Petit, V. Blanchet, B. Pons, N. Dudovich, et al. Controlling subcycle optical chirality in the photoionization of chiral molecules. *Physical Review X*, 9(3):031004, 2019.
- E. Runge and E. K. U. Gross. Density-functional theory for time-dependent systems. *Physical Review Letters*, 52(12):997, 1984.
- J. J. Sakurai. *Advanced quantum mechanics*. Pearson Education India, 2006.
- G. Sansone, F. Kelkensberg, J. Pérez-Torres, F. Morales, M. F. Kling, W. Siu, O. Ghafur, P. Johnsson, M. Swoboda, E. Benedetti, et al. Electron localization following attosecond molecular photoionization. *Nature*, 465(7299):763–766, 2010.



- E. Santoro, S. Vergura, P. Scafato, S. Belviso, M. Masi, A. Evidente, and S. Supercchi. Absolute configuration assignment to chiral natural products by biphenyl chiroptical probes: The case of the phytotoxins colletochlorin a and agropyrenol. *Journal of Natural Products*, 83(4):1061–1068, 2020.
- R. Santra, G. Dixit, and J. M. Slowik. Comment on “how to observe coherent electron dynamics directly”. *Physical Review Letters*, 113(18):189301, 2014.
- A. Schiffrin, T. Paasch-Colberg, N. Karpowicz, V. Apalkov, D. Gerster, S. Mühlbrandt, M. Korbman, J. Reichert, M. Schultze, S. Holzner, et al. Optical-field-induced current in dielectrics. *Nature*, 493(7430):70–74, 2013.
- M. Schultze, M. Fieß, N. Karpowicz, J. Gagnon, M. Korbman, M. Hofstetter, S. Neppl, A. L. Cavalieri, Y. Komninos, T. Mercouris, et al. Delay in photoemission. *Science*, 328(5986):1658–1662, 2010.
- M. Schultze, K. Ramasesha, C. Pemmaraju, S. Sato, D. Whitmore, A. Gandman, J. S. Prell, L. Borja, D. Prendergast, K. Yabana, et al. Attosecond band-gap dynamics in silicon. *Science*, 346(6215):1348–1352, 2014.
- L. Serrano-Andres, M. Merchán, I. Nebot-Gil, B. O. Roos, and M. Fulscher. Theoretical study of the electronic spectra of cyclopentadiene, pyrrole, and furan. *Journal of the American Chemical Society*, 115(14):6184–6197, 1993.
- J. Shao, V. Pohl, L. E. Marsoner Steinkasserer, B. Paulus, and J. C. Tremblay. Electronic current mapping of transport through defective zigzag graphene nanoribbons. *Journal of Physical Chemistry C*, 124(43):23479–23489, 2020.
- J. Shao, B. Paulus, and J. C. Tremblay. Local current analysis on defective zigzag graphene nanoribbons devices for biosensor material applications. *Journal of Computational Chemistry*, 42(21):1475–1485, 2021.
- M. Simmermacher, N. E. Henriksen, K. B. Møller, A. M. Carrascosa, and A. Kirrander. Electronic coherence in ultrafast x-ray scattering from molecular wave packets. *Physical Review Letters*, 122(7):073003, 2019a.
- M. Simmermacher, A. Moreno Carrascosa, N. E. Henriksen, K. B. Møller, and A. Kirrander. Theory of ultrafast x-ray scattering by molecules in the gas phase. *Journal of Chemical Physics*, 151(17):174302, 2019b.

- W. Siu, F. Kelkensberg, G. Gademann, A. Rouzée, P. Johnsson, D. Döwck, M. Lucchini, F. Calegari, U. De Giovannini, A. Rubio, et al. Attosecond control of dissociative ionization of  $\text{O}_2$  molecules. *Physical Review A*, 84(6):063412, 2011.
- O. Smirnova, Y. Mairesse, and S. Patchkovskii. Opportunities for chiral discrimination using high harmonic generation in tailored laser fields. *Journal of Physics B*, 48(23):234005, 2015.
- S. Sobottka, M. Nöckler, A. L. Ostericher, G. Hermann, N. Z. Subat, J. Beerhues, M. Behr-van Der Meer, L. Suntrup, U. Albold, S. Hohloch, et al. Tuning pti-based donor–acceptor systems through ligand design: effects on frontier orbitals, redox potentials, uv/vis/nir absorptions, electrochromism, and photocatalysis. *Chemistry–A European Journal*, 26(6):1314–1327, 2020.
- A. Sommer, E. Bothschafter, S. Sato, C. Jakubeit, T. Latka, O. Razskazovskaya, H. Fattahi, M. Jobst, W. Schweinberger, V. Shirvanyan, et al. Attosecond nonlinear polarization and light–matter energy transfer in solids. *Nature*, 534(7605):86–90, 2016.
- A. Szabo and N. S. Ostlund. *Modern quantum chemistry: introduction to advanced electronic structure theory*. Courier Corporation, 2012.
- K. Takatsuka and T. Yonehara. Exploring dynamical electron theory beyond the born–oppenheimer framework: from chemical reactivity to non-adiabatically coupled electronic and nuclear wavepackets on-the-fly under laser field. *Physical Chemistry Chemical Physics*, 13(11):4987–5016, 2011.
- K. Takatsuka, Y. Arasaki, T. Yonehara, and K. Hanasaki. *Chemical theory beyond the Born-Oppenheimer paradigm: nonadiabatic electronic and nuclear dynamics in chemical reactions*. World Scientific, 2014.
- D. J. Tannor. *Introduction to quantum mechanics: a time-dependent perspective*. 2007.
- J. C. Tremblay and T. Carrington Jr. Using preconditioned adaptive step size runge-kutta methods for solving the time-dependent schrödinger equation. *Journal of Chemical Physics*, 121(23):11535–11541, 2004.
- J. C. Tremblay and P. Saalfrank. Guided locally optimal control of quantum dynamics in dissipative environments. *Physical Review A*, 78(6):063408, 2008.

- J. C. Tremblay, T. Klamroth, and P. Saalfrank. Time-dependent configuration-interaction calculations of laser-driven dynamics in presence of dissipation. *Journal of Chemical Physics*, 129(8):084302, 2008.
- J. C. Tremblay, S. Klinkusch, T. Klamroth, and P. Saalfrank. Dissipative many-electron dynamics of ionizing systems. *Journal of Chemical Physics*, 134(4):044311, 2011.
- J. C. Tremblay, V. Pohl, G. Hermann, and G. Dixit. Time-resolved imaging of correlation-driven charge migration in light-induced molecular magnets by x-ray scattering. *Faraday Discussions*, 228:82–103, 2021.
- I. Tutunnikov, E. Gershnel, S. Gold, and I. S. Averbukh. Selective orientation of chiral molecules by laser fields with twisted polarization. *The Journal of Physical Chemistry Letters*, 9(5):1105–1111, 2018.
- I. Tutunnikov, J. Floß, E. Gershnel, P. Brumer, I. S. Averbukh, A. A. Milner, and V. Milner. Observation of persistent orientation of chiral molecules by a laser field with twisted polarization. *Physical Review A*, 101(2):021403, 2020.
- M. Uiberacker, T. Uphues, M. Schultze, A. J. Verhoef, V. Yakovlev, M. F. Kling, J. Rauschenberger, N. M. Kabachnik, H. Schröder, M. Lezius, et al. Attosecond real-time observation of electron tunnelling in atoms. *Nature*, 446(7136):627–632, 2007.
- I. S. Ulusoy and M. Nest. Correlated electron dynamics: How aromaticity can be controlled. *Journal of the American Chemical Society*, 133(50):20230–20236, 2011.
- R. Van Leeuwen. Mapping from densities to potentials in time-dependent density-functional theory. *Physical Review Letters*, 82(19):3863, 1999.
- M. J. Vrakking and T. Elsaesser. X-rays inspire electron movies. *Nature Photonics*, 6(10):645–647, 2012.
- J. Wan, J. Meller, M. Hada, M. Ehara, and H. Nakatsuji. Electronic excitation spectra of furan and pyrrole: Revisited by the symmetry adapted cluster–configuration interaction method. *Journal of Chemical Physics*, 113(18):7853–7866, 2000.

- D. Wang, X. Zhu, X. Liu, L. Li, X. Zhang, P. Lan, and P. Lu. High-harmonic generation from axial chiral molecules. *Optics Express*, 25(19):23502–23516, 2017.
- M. R. Ware, J. M. Glowacki, N. Al-Sayyad, J. T. O’Neal, and P. H. Bucksbaum. Characterizing dissociative motion in time-resolved x-ray scattering from gas-phase diatomic molecules. *Physical Review A*, 100(3):033413, 2019.
- H. J. Wörner, C. A. Arrell, N. Banerji, A. Cannizzo, M. Chergui, A. K. Das, P. Hamm, U. Keller, P. M. Kraus, E. Liberatore, et al. Charge migration and charge transfer in molecular systems. *Structural Dynamics*, 4(6):061508, 2017.
- A. Yachmenev and S. N. Yurchenko. Detecting chirality in molecules by linearly polarized laser fields. *Physical Review Letters*, 117(3):033001, 2016.
- K. Yamamoto and K. Takatsuka. An electron dynamics mechanism of charge separation in the initial-stage dynamics of photoinduced water splitting in x–mn–water (x = oh, ocah) and electron–proton acceptors. *ChemPhysChem*, 16(12):2534–2537, 2015.
- T. Yanai, D. P. Tew, and N. C. Handy. A new hybrid exchange–correlation functional using the coulomb-attenuating method (cam-b3lyp). *Chemical Physics Letters*, 393(1-3):51–57, 2004.
- H. Yong, N. Zotev, B. Stankus, J. M. Ruddock, D. Bellshaw, S. Boutet, T. J. Lane, M. Liang, S. Carbajo, J. S. Robinson, et al. Determining orientations of optical transition dipole moments using ultrafast x-ray scattering. *Journal of Physical Chemistry Letters*, 9(22):6556–6562, 2018.
- H. Yong, N. Zotev, J. M. Ruddock, B. Stankus, M. Simmermacher, A. M. Carascosa, W. Du, N. Goff, Y. Chang, D. Bellshaw, et al. Observation of the molecular response to light upon photoexcitation. *Nature Communications*, 11(1):1–6, 2020.
- H. Yong, S. M. Cavaletto, and S. Mukamel. Ultrafast valence-electron dynamics in oxazole monitored by x-ray diffraction following a stimulated x-ray raman excitation. *Journal of Physical Chemistry Letters*, 12(40):9800–9806, 2021.
- H. Yong, S. Sun, B. Gu, and S. Mukamel. Attosecond charge migration in molecules imaged by combined x-ray and electron diffraction. *Journal of the American Chemical Society*, 2022.

## BIBLIOGRAPHY

---

A. H. Zewail. Femtochemistry: Atomic-scale dynamics of the chemical bond. *Journal of Physical Chemistry A*, 104(24):5660–5694, 2000.



# List of Publications

## A. Part of this thesis

1. **Sucharita Giri**, Alexandra Maxi Dudzinski, Jean Christophe Tremblay, and Gopal Dixit: “Time-dependent electronic current densities in chiral molecules” **Physical Review A** **102**, 063103 (2020).
2. **Sucharita Giri**, Jean Christophe Tremblay, and Gopal Dixit: “Imaging charge migration in chiral molecules using time-resolved x-ray diffraction” **Physical Review A** **104**, 053115 (2021).
3. **Sucharita Giri**, Jean Christophe Tremblay, and Gopal Dixit: “Probing the effect of molecular structure saddling on ultrafast charge migration via time-resolved x-ray diffraction” **Physical Review A** **106**, 033120 (2022).
4. **Sucharita Giri**, Gopal Dixit, and Jean Christophe Tremblay: “Charge migration in heterocyclic five-membered rings” (accepted in The European Physical Journal Special Topics).

## B. Not part of this thesis

1. **Sucharita Giri**, Misha Ivanov, and Gopal Dixit: “Signatures of the orbital angular momentum of an infrared light beam in the two-photon transition matrix element: A step toward attosecond chronoscopy of photoionization” **Physical Review A** **101**, 033412 (2020).
2. Nilanjan Roy, **Sucharita Giri**, and Partha Pratim Jana: “Site preference and atomic ordering in the ternary Rh<sub>5</sub>Ga<sub>2</sub>As: first-principles calculations” **Zeitschrift fuer Kristallographie-Crystalline Materials** **236**, 147-54 (2021).

3. Jean Christophe Tremblay, Ambre Blanc, Pascal Krause, **Sucharita Giri**, and Gopal Dixit: “Probing electronic symmetry reduction during charge migration via time-resolved x-ray diffraction” **Chem. Phys. Chem.** **e202200463** (2022).



# Conferences Attended

## A. International

1. **ATTOCHEM2020**, Online (9 - 11 September 2020).
2. **UXSS2021**, Online (14 - 18 June 2021).
3. **UXSS2022**, Paris, France (10 - 14 October 2022).
4. **Theory Meets XFELs Workshop**, Hamburg, Germany (2 - 4 November 2022).

## B. National

1. **UFS 2017**, University of Hyderabad (02 - 04 November, 2017).
2. **UFS 2019**, IIT Bombay (07 - 09 November, 2019).
3. **8<sup>th</sup> TC2020**, IIT Roorkee (03 - 05 March, 2020).

